TOWARDS A PRECISION MEASUREMENT OF THE HALF LIFE OF NEUTRINOLESS DOUBLE BETA DECAY OF ^{136}XE

A DISSERTATION
SUBMITTED TO THE DEPARTMENT OF PHYSICS
AND THE COMMITTEE ON GRADUATE STUDIES
OF STANFORD UNIVERSITY
IN PARTIAL FULFILLMENT OF THE REQUIREMENTS
FOR THE DEGREE OF
DOCTOR OF PHILOSOPHY

Francisco LePort
September 2010

This dissertation is online at: http://purl.stanford.edu/gq005wr3931

I certify that I have read this dissertation and that, in my opinion, it is fully adequate in scope and quality as a dissertation for the degree of Doctor of Philosophy.

Giorgio Gratta, Primary Adviser

I certify that I have read this dissertation and that, in my opinion, it is fully adequate in scope and quality as a dissertation for the degree of Doctor of Philosophy.

Peter Michelson

I certify that I have read this dissertation and that, in my opinion, it is fully adequate in scope and quality as a dissertation for the degree of Doctor of Philosophy.

Stephen Shenker

Approved for the Stanford University Committee on Graduate Studies.

Patricia J. Gumport, Vice Provost Graduate Education

This signature page was generated electronically upon submission of this dissertation in electronic format. An original signed hard copy of the signature page is on file in University Archives.

Abstract

Recent neutrino oscillation experiments provide proof that neutrinos are massive particles, but the absolute neutrino mass scale remains unknown. Observation of neutrinoless double beta-decay ($0\nu\beta\beta$), a hypothetical nuclear transition, would provide information on the absolute neutrino mass scale. This decay violates lepton number conservation and requires that neutrinos are massive Majorana particles.

Current limits on the half-life of $0\nu\beta\beta$ are in excess of $\sim 10^{25}$ yr. The 200 kg Enriched Xenon Observatory experiment (EXO-200) is a double beta-decay experiment designed to improve upon this limit. It is currently in the early stages of commissioning at the Waste Isolation Pilot Plant near Carlsbad, New Mexico. This work discusses first the use of liquid xenon as source and detector medium for double beta decay. The design and construction of EXO-200 is then presented, including a detailed prediction of detector backgrounds and sensitivity.

Acknowledgements

Thank you to everyone who has helped me get this far. To my advisor Giorgio Gratta, who has taught me that you can get (almost) anything done if you're clever enough. To Andrea Pocar, for making my experience as a junior grad student particularly fun. To Henry Sobel and Shunichi Mine, for providing an incredible introduction to experimental particle physics. To the teachers I've had since pre-school who have always encouraged me to go as far as I could. To all of my friends who were there for me no matter what. To my family which I could always count on. And most importantly to my parents, who have guided and supported me and made it all possible.

Contents

List of Tables

List of Figures

Chapter 1

Introduction

Recent pioneering neutrino oscillation experiments such as Super-Kamiokande[26], KamLAND[27], SNO[28], and others have provided evidence that neutrinos are massive particles. Prior to these experiments, the Standard Model (SM) of particle physics assumed that neutrinos were massless. The evidence of neutrino mass has therefore opened new avenues of research. Yet neutrino oscillation experiments are sensitive only to differences in the neutrino masses. A measurement of the absolute neutrino mass scale would have a profound impact on our understanding of the physics of fundamental particles and interactions.

Measurement of the half-life of a yet unobserved second order process, neutrinoless double beta-decay[29] ($0\nu\beta\beta$), is a promising method of measuring the neutrino mass scale. $0\nu\beta\beta$ decay violates lepton number conservation [30], and is forbidden under standard electroweak theory. In addition, observation of this decay would imply that the neutrino is a Majorana particle (that there is no distinction between a neutrino and an anti-neutrino), rather than a Dirac particle as are all other known fermions.

This thesis will discuss and motivate the design of the 200kg Enriched Xenon Observatory (EXO-200) experiment, which aims primarily to measure the half life of $0\nu\beta\beta$ of ^{136}Xe. EXO-200 will also measure the half life of as yet unobserved two neutrino double beta-decay ($2\nu\beta\beta$) of ^{136}Xe and serve as a stepping stone in the larger EXO project, a ton scale experiment designed for background-free measurement of $0\nu\beta\beta$ of ^{136}Xe.

The remainder of this chapter briefly discusses the current status of neutrino mass scale measurements and the relationship between neutrino mass and $0\nu\beta\beta$. In chapter 2, the use of ^{136}Xe as source and medium for detection of double beta-decay is discussed. Chapter 3 presents a brief overview of the detector. General background requirements are described and methods used to reduce the background are outlined. A material qualification campaign is outlined, and the simulation tools used to inform design choices are described. Chapters 4 and 5 detail the design and fabrication of all major components of the experiment, including the impact of each component on the background to the measurement. In chapter 6 electronics and calibration requirements for the detector are discussed. Chapter 7 summarizes the total background contribution and details the expected sensitivity of the EXO-200 experiment as constructed. Finally, Appendix A discusses Teflon as an alternative material for an ultra low-background liquid xenon (LXe) chamber, and presents results from the operation of a prototype all-Teflon LXe cell.

1.1 Absolute Neutrino Mass and $0\nu\beta\beta$

$2\nu\beta\beta$ is a standard model process in which a nucleus with charge Z and mass A decays to two electrons, two anti-neutrinos, and a mass A nucleus with charge Z+2:

$$(Z, A) \rightarrow (Z + 2, A) + e^- + e^- + \bar{\nu}_e + \bar{\nu}_e \tag{1.1}$$

The Feynman diagram for $2\nu\beta\beta$ is shown in fig. 1.1a. Half-lives for this decay have been observed for several nuclei, the most significant of which are listed in table 1.1. $2\nu\beta\beta$ of ^{136}Xe has not yet been observed. To date the best upper limit is $T_{1/2}^{2\nu\beta\beta} > 1.0 \times 10^{22}$ [31].

$0\nu\beta\beta$ is a hypothetical process with similar phenomenology but very different origin in which a nucleus with charge Z and mass A decays to two electrons and a nucleus with charge Z+2 and mass A. No anti-neutrinos are emitted:

$$(Z, A) \rightarrow (Z + 2, A) + e^- + e^- \tag{1.2}$$

Isotope	Experiment	$T_{1/2}^{2\nu\beta\beta}$ [$\times 10^{21}$ yr]	$T_{1/2}^{0\nu\beta\beta}$ [$\times 10^{25}$ yr]
^{76}Ge	Heidelberg-Moscow[32]	$1.55 \pm 0.001^{+0.19}_{-0.15}$	>1.9*
^{82}Se	NEMO-3[33]	$(9.6 \pm 0.3 \pm 0.1) \times 10^{-2}$	>0.014
^{96}Zr	NEMO-2[34]	$(2.1^{+0.8}_{-0.4} \pm 0.2) \times 10^{-2}$	>0.0001
^{100}Mo	NEMO-3[33]	$(7.68 \pm 0.02 \pm 0.54) \times 10^{-3}$	>0.046
^{116}Cd	CAMEO[35]	$(2.9^{+0.4}_{-0.3}) \times 10^{-2}$	>0.017
^{130}Te	Cuoricino[36]	$0.61 \pm 0.14^{+0.29}_{-0.35}$	>0.3
^{136}Xe	Bernabei[31]	> 10	>0.12

Table 1.1: 90% CL measurements of $T_{1/2}^{2\nu\beta\beta}$ and limits for $T_{1/2}^{0\nu\beta\beta}$ for various isotopes. Table adapted from [1]. *Part of the Heidelberg-Moscow colaboration claims a positive signal with $T_{1/2}^{2\nu\beta\beta\_Ge} = 2.23^{+0.44}_{-0.31} \times 10^{25}$ yr[2], though this claim is highly controversial[3]

The detection of such a reaction necessarily implies a left-handed Majorana neutrino mass term and violation of lepton number conservation, as shown by the Feynman diagram in figure 1.2. A minimally modified standard model interaction, shown in figure 1.1b, as well as more exotic interactions from a wide variety of models, including supersymmetric[37], scalar bilinear[38], and bileptonic[39], can contribute to this decay. Other less exotic interactions, including right-handed weak current coupling, can also contribute. This work assumes that the contribution of any interaction other than that shown in figure 1.1b is negligible.

If SM interactions at both vertices are assumed, the right-handed antineutrino emitted at vertex A is absorbed as a left-handed neutrino at vertex B. The effective Majorana neutrino mass $\langle m_{\beta\beta} \rangle$, a superposition of all three neutrino mass eigenstates, participates in this reaction

$$\langle m_{\beta\beta} \rangle = \sum_j \left| U_{ej}^2 \right| e^{i\alpha_j} m_j \tag{1.3}$$

where U_{ej} are the elements of the MNS Lepton Mixing Matrix[40] and α_j are the Majorana phases of U shown explicitly. $\langle m_{\beta\beta} \rangle$ is related to the half-life of $0\nu\beta\beta$, $T_{1/2}^{0\nu\beta\beta}$, via[5]

$$T_{1/2}^{0\nu\beta\beta} = 1/(G^{0\nu\beta\beta}(Q,Z) \left| M^{0\nu} \right|^2 \langle m_{\beta\beta} \rangle^2) \tag{1.4}$$

Isotope	Method	$\langle m_{\beta\beta} \rangle$ [eV]
^{76}Ge	Heidelberg-Moscow[32]	<0.35-0.50*
^{82}Se	NEMO-3[33]	<1.7-4.9
^{96}Zr	NEMO-2[34]	<23
^{100}Mo	NEMO-3[33]	<0.7-2.8
^{116}Cd	CAMEO[35]	<1.5-1.7
^{130}Te	Cuoricino[36]	<0.19-0.68
^{136}Xe	LXe scint.[31]	<2.9

Table 1.2: Best limits on $\langle m_{\beta\beta} \rangle$ for various experimental methods. Table adapted from [1]. *Part of the Heidelberg-Moscow colaboration claims a positive signal with $\langle m_{\beta\beta} \rangle = 0.32 \pm 0.03$ eV[2] ($\langle m_{\beta\beta} \rangle = 0.25 \pm 0.02$ eV using the NME listed in table 1.3), though this claim is highly controversial[3]

where $G^{0\nu\beta\beta}(Q, Z)$ is a well-understood phase-space factor depending on the endpoint energy Q and nuclear charge Z and $|M^{0\nu}|$ is the calculated nuclear matrix element (NME). Upper limits for $T^{0\nu\beta\beta}_{1/2}$ for several nuclei are listed in table 1.1.

Calculations of $\langle m_{\beta\beta} \rangle$ are shown in table 1.2. The uncertainties shown include both theoretical and experimental components. The majority of the theoretical uncertainty in calculating $\langle m_{\beta\beta} \rangle$ comes from the variety of methods of calculating the nuclear matrix element term $\left|M'^{0\nu}\right|$. Different models predict different values of $\left|M'^{0\nu}\right|$, and even within a specific model many assumptions contribute to uncertainty. Table 1.3 lists phase space factors for several candidate $0\nu\beta\beta$ isotopes[4], as well as a calculation of NMEs obtained using the Renormalized Quasiparticle Random Phase Approximation (RQRPA)[5] and Interacting Shell Model[6]. Calculations of the nuclear matrix elements using other methods and assumptions can be found in [7, 8, 9, 10, 11, 12].

1.2 Measuring Absolute Neutrino Mass via Detection of $0\nu\beta\beta$

The sum energy spectrum of the electrons emitted in $0\nu\beta\beta$ is a delta-function centered about the total energy of the decay (Q). Assuming only contributions from the

Isotope	$G^{0\nu\beta\beta}(Q,Z) \times 10^{26}$ [yr^{-1}]	$\lvert M'^{0\nu}_{RQRPA}\rvert$	$\lvert M'^{0\nu}_{ISM}\rvert$ [eV]
^{76}Ge	2.44	4.07 - 6.64	2.96
^{82}Se	10.79	3.53 - 5.92	2.79
^{96}Zr	22.42	1.43 - 2.12	*
^{100}Mo	17.54	2.91 - 5.56	*
^{116}Cd	18.94	2.30 - 4.14	*
^{130}Te	16.98	2.92 - 5.04	2.81
^{136}Xe	18.12	1.57 - 3.24	2.32

Table 1.3: Theoretical phase space factors[4] and nuclear matrix elements calculated using RQRPA[5] and ISM[6] for several enrichable candidate $0\nu\beta\beta$ isotopes. Other nuclear matrix element calculations can be found in [7, 8, 9, 10, 11, 12]. *NMEs for these isotopes in the ISM model have not yet been published.

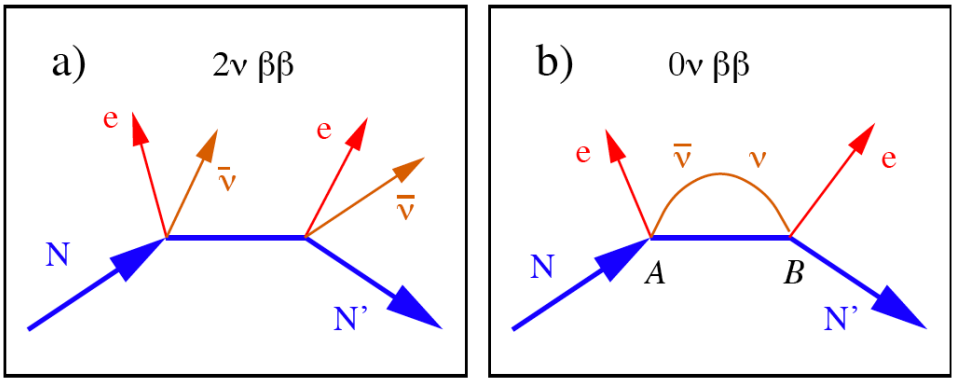

Figure 1.1: Feynman diagrams for (a) (standard) two-neutrino double beta-decay ($2\nu\beta\beta$) and (b) neutrinoless double beta-decay ($0\nu\beta\beta$). N and N' are the initial and final nuclei.

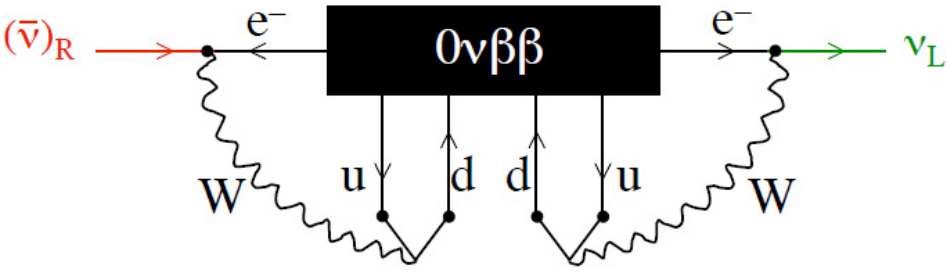

Figure 1.2: Neutrinoless double beta-decay necessarily implies a left-handed majorana neutrino mass and violation of lepton number conservation.

Feynmann Diagram shown in figure 1.1b and a background-free measurement, a simple count of events occurring within an energy window centered around Q provides a measure of $T_{1/2}^{0\nu\beta\beta}$, from which the effective Majorana neutrino mass via eqn. 1.4 can be obtained.

Based on the very high limits set thus far for $T_{1/2}^{0\nu\beta\beta}$ (listed in table 1.1), it is clear that a central driving force for all $0\nu\beta\beta$ experiments is background minimization. Two sources of such background exist for $0\nu\beta\beta$ experiments. The first is $2\nu\beta\beta$ itself. The sum electron energy spectrum for $2\nu\beta\beta$ is continuous, since the total energy of the decay is shared between the emitted electrons and neutrinos. Fig 1.3 shows the combined sum electron energy spectra of $0\nu\beta\beta$ and $2\nu\beta\beta$ convolved with a 1.5% (σ) detector energy resolution, for $0\nu\beta\beta/2\nu\beta\beta$ rate ratios of 10^{-2} and 10^{-5}. The portion of the $2\nu\beta\beta$ spectrum lying within the $0\nu\beta\beta$ energy window is a background to the $0\nu\beta\beta$ signal. Improvement of energy resolution is essentially the sole means of mitigating this background, as it is indistinguishable from the $0\nu\beta\beta$ signal without detection of the emitted anti-neutrinos or the individual momenta of each emitted electron.

The second source of background for $0\nu\beta\beta$ experiments is any spurious ionizing radiation depositing an energy into the detector which lies within the $0\nu\beta\beta$ window. The "full EXO" experiment is currently the only proposed experiment which would completely eliminate this source of background by positively identifying the Ba daughter of each candidate $0\nu\beta\beta$. EXO-200 will not employ this technique, but employs several other means of mitigating background events. (1) Improvements in energy resolution (see chapter 2) narrow the $0\nu\beta\beta$ window, thus narrowing the probability that the spurious energy deposition will be mistaken for signal. (2) Much of this background is caused by spurious gammas which Compton scatter, depositing energy in several locations as they travel many centimeters through the detector. A homogeneous, fully sensitive detector can be used to reject such "multi-site" events. (3) The use of radio-pure materials in constructing the detector and shielding reduces the source of external ionizing radiation. (4) Placing the detector deep underground and using an active veto system mitigates the effects of Cosmic Rays. Details on these and other backgrounds and mitigation techniques can be found in chapter 3.

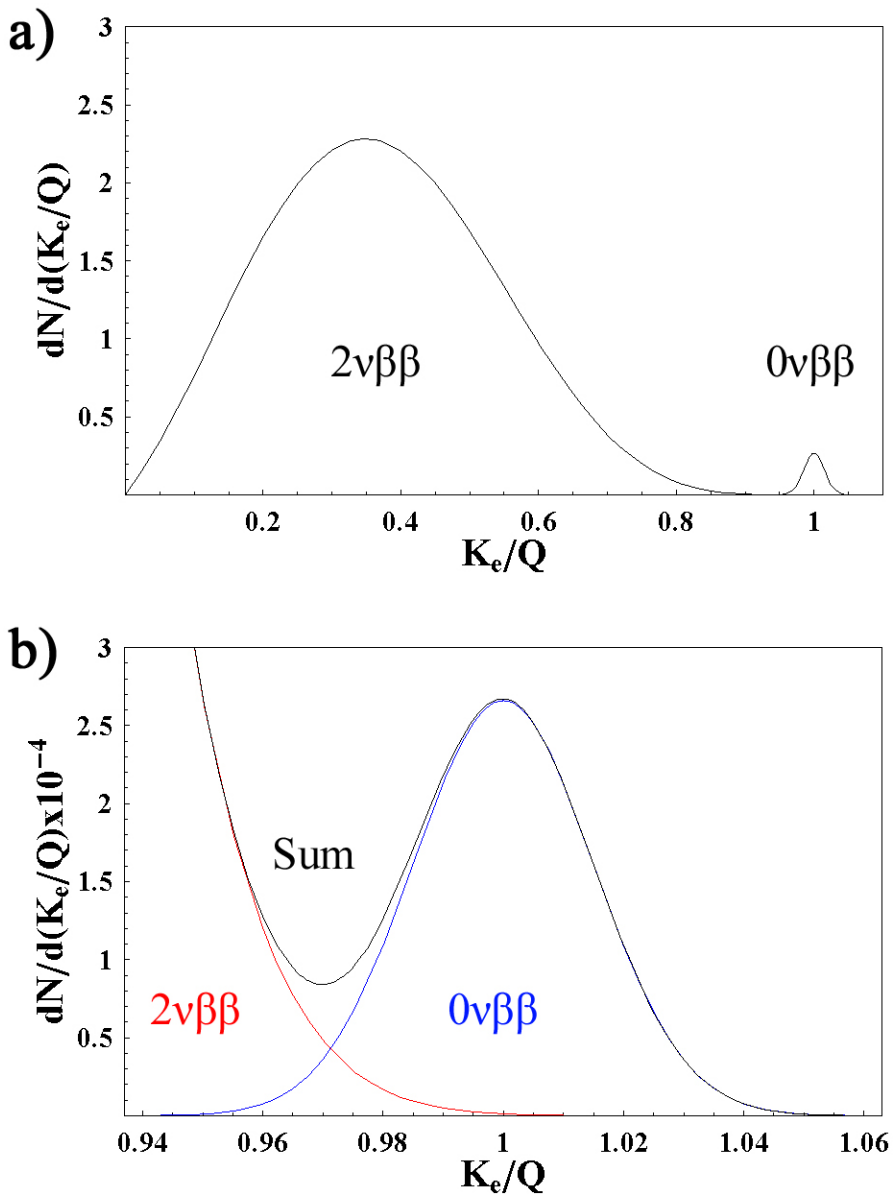

Figure 1.3: a) Spectra of the sum of electron energies, K_e, from $2\nu\beta\beta$ and $0\nu\beta\beta$ decay, normalized by the decay endpoint Q. In this figure the ratio of $0\nu\beta\beta$ to $2\nu\beta\beta$ counts $= 10^{-2}$. b) Magnification of endpoint with ratio of $0\nu\beta\beta$ to $2\nu\beta\beta$ counts $= 10^{-5}$. All spectra are convolved with an energy resolution of 1.5% σ.

Spurious ionizing radiation is a background for measurement of $T_{1/2}^{2\nu\beta\beta}$ as well, if the deposited energy lies within the $2\nu\beta\beta$ window. Techniques 2-4 mentioned in the previous paragraph also reduce this background.

1.3 Status of Neutrino Mass Scale Measurements

Data from solar, atmospheric, and reactor neutrino oscillation experiments provide strong evidence for the existence of three massive neutrinos, labeled m_1, m_2, m_3. These mass eigenstates are related to the eigenstates of the weak force, ν_e, ν_μ, ν_τ, via U_{ij},

$$\nu_i = \sum_j^3 U_{ij} m_j \qquad i = (e, \mu, \tau) \tag{1.5}$$

Measurements of neutrino oscillations in many experiments of varying baseline imply non-zero off-diagonal terms in the MNS mixing matrix, and non-zero neutrino mass differences. Unfortunately neutrino oscillation measurements reveal little about absolute neutrino masses. The strongest constraint is imposed by ν_μ disappearance measurements, which reveal a mass splitting $|\Delta m^2_{32}| = (2.35^{+0.11}_{-0.08}) \times 10^{-3}$ eV^2 and impose a lower limit on the heaviest neutrino mass of 0.048 eV[41].

A variety of non-oscillation experiments, such as β-decay endpoint measurements, cosmological observations, and $0\nu\beta\beta$ measurements shed more light on the absolute neutrino masses. The Mainz[42] and Troitsk[43] experiments measured the tritium β-decay energy spectrum at the endpoint and set upper limits for the mass of the electron neutrino of 2.2-2.5 eV. KATRIN is designed to improve on this limit, with a sensitivity of 0.2 eV[44]. Results from cosmology experiments such as WMAP and Sloan Digital Sky Survey, and supernovae and galaxy clustering constraints point toward an upper limit on the sum of neutrino masses $\sum_{i=1}^3 m_i$ ranging from 0.17 - 0.75 eV (95% C.L.) [45, 46, 47], though as made clear by the references, these estimates are highly model dependent.

Ton scale $0\nu\beta\beta$ experiments have the potential to reach sensitivities to neutrino mass of several meV, provided that neutrinos are Majorana particles. Though ton scale has not yet been achieved, it being aggressively pursued through a variety of

techniques including

- Cryogenic bolometers (CUORE)
- Ionization detectors (COBRA, Majorana, Gerda)
- Scintillation detectors (CAMEO, CANDLES, SNO+, KAMLAND-ZEN)
- Time projection and tracking chambers (EXO-200, MOON, NEMO, NeXT)

A thorough discussion of experimental techniques for detection of $0\nu\beta\beta$ is beyond the scope of this work. A list of limits on $\langle m_{\beta\beta}\rangle$ for various isotopes was shown earlier in table 1.2. The best limit on the effective Majorana neutrino mass due to $0\nu\beta\beta$ was set by the Heidelberg-Moscow experiment as $\langle m_{\beta\beta}\rangle <$ (0.35 - 0.50) eV [32]. A portion of the Heidelberg-Moscow collaboration claims a positive signal at $\langle m_{\beta\beta}\rangle = 0.32 \pm 0.03$ eV [48, 49, 2], though this claim is highly controversial [3].

^{136}Xe offers many unique advantages in the search for the absolute neutrino mass scale and pursuit of a very low background ton scale $0\nu\beta\beta$ experiment. These advantages will be discussed in the following chapter.

Chapter 2

Liquid Xe as Detection Source and Medium

The use of LXe for radiation detection was first investigated by Alvarez in 1968[50]. The advantages LXe offers in this application include an inert chemistry, high ionization and scintillation yields relative to other noble liquids, and good electron mobility. In addition, high density and atomic number provide the highest stopping power for ionizing radiation among the noble liquids.

LXe offers many advantages specific to the search for $0\nu\beta\beta$:

- Experiments using other elements (e.g. ^{76}Ge in Heidelberg-Moscow and Majorana, or ^{130}Te in CUORE) require a complex process of ultra high purity crystallization. This process is not necessary when using LXe.

- Arbitrarily large homogeneous volumes of LXe are possible, allowing LXe experiments to take full advantage of self-shielding. Other elements require the use of foils (e.g. ^{100}Mo in MOON or NEMO3) or arrays of smaller detectors, introducing impurities within the double beta-decay medium and making it hard to scale.

- Given its liquid form, continuous purification is possible. Because xenon is a noble element, purification is relatively simple, and can be performed using commercial products. Solid elements used in other $0\nu\beta\beta$ experiments require

high initial purity, since further purification is not possible. Verifying the purity of this initial production is made difficult due to the extreme sensitivity required (typically one part in 10^{14}).

- Xe has no long lived isotopes activated by cosmogenics. Byproducts of an interaction of ^{76}Ge, for example, can result in ^{60}Co ($T_{1/2}$ = 5.27 yr, Q = 2.823 MeV).

- Due to small natural isotopic abundances, enrichment is necessary for large $0\nu\beta\beta$ detectors (except possibly in the case of ^{130}Te, which has a natural abundance of 34%). Enrichment of ^{136}Xe is possible by centrifuge, and is made relatively easy because chemistry is not required to put it in gaseous form.

- LXe detectors operate at a relatively high temperature (∼170K). Other experiments (e.g. CUORE) must operate at far lower temperatures.

- Finally, Xe can be transferred easily from one detector to another, reducing the cost of upgrading and integrating new technologies.

The energy resolution thus far achieved in LXe is worse than that achieved using other techniques, but this disadvantage can be mitigated. Other double beta decay experiments have proven energy resolutions of ∼0.1-0.2% (σ/E) at the end point energy[51, 48]. Work by our group[20] has shown that an energy resolution of 3% (σ/E) can be achieved at 570 keV by a combined analysis of scintillation and ionization signals in LXe. More recent work by Aprile et al. [52] has shown that improved light collection efficiency allows an energy resolution of 1.7% (σ) at 662 keV. Given a Q-value of 2.458 MeV for ^{136}Xe[53], and assuming that energy resolution scales as the square root of energy, theory predicts an energy resolution of 0.9% (σ) in EXO-200 at the $0\nu\beta\beta$ endpoint energy.

The EXO-200 detector is constructed assuming an energy resolution of no worse than 1.5% (σ) will be achieved at the Q-value. As described in chapters 3 - 5, detailed Monte Carlo predicts that such resolution is sufficient for meaningful $0\nu\beta\beta$ measurements once the background has been minimized by stringent material purity standards, design parameters, and construction practices.

Isotope	Mass [amu]	Content fraction [%]
136	135.907	8.9
134	133.905	10.4
132	131.904	26.9
131	103.905	21.2
130	129.904	4.1
129	128.905	26.4
128	127.904	1.9
126	125.904	0.09
124	123.906	0.10

Table 2.1: Isotopic composition of natural xenon[13].

Isotope	Content fraction [%]
136	80.6
134	19.1
132	0.2
124-131	<0.1

Table 2.2: Isotopic composition of EXO-200 enriched xenon. Error is 0.1%.

The rest of this chapter will discuss the basic properties of LXe as related to EXO-200 and the detection of $0\nu\beta\beta$ as well as an overview of the physical processes that lead to the production of ionization electrons and scintillation photons. A very thorough theoretical and experimental treatment of this topic can be found in [54].

2.1 Physical Properties of EXO-200 Enriched Xe

Xenon has a standard atomic mass of 131.3 amu. Its isotopic composition in the Earth's atmosphere (natural xenon) is shown in table 2.1. The xenon used in EXO-200 was obtained and enriched by the Ministry of Atomic Energy in Russia. A total of 199.419 kg of enriched xenon was delivered in 10 gas bottles. Each gas bottle was sampled and isotopic composition was measured using a residual gas analyzer. The average composition of the enriched xenon across all bottles is shown in table 2.2. The average atomic mass of EXO-200 enriched xenon is 135.5 amu. This value is

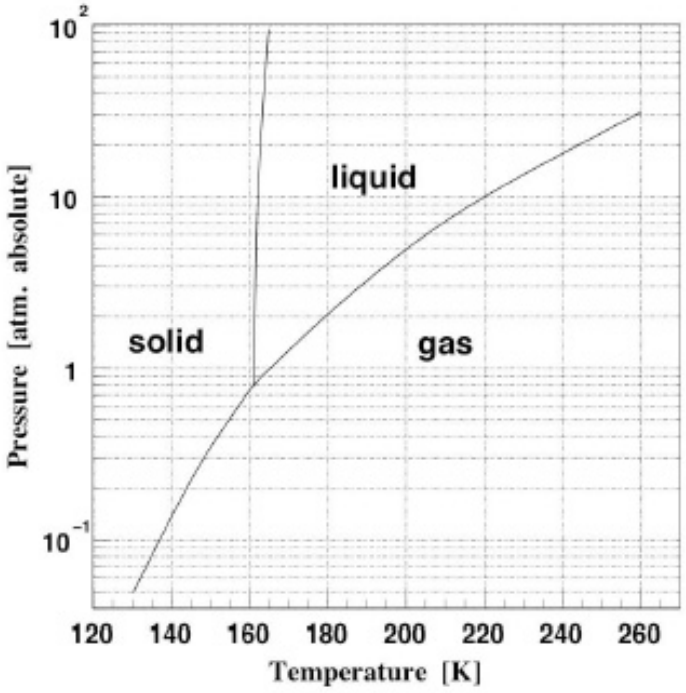

Figure 2.1: Phase diagram for Xenon. Image adapted from [18].

assumed for all physical properties listed in this work unless otherwise noted. After sampling, 198.487 kg are available for use in the experiment.

The relevant thermodynamic properties of xenon are listed in table 2.3. The phase diagram for xenon is shown in figure 2.1. EXO-200 operates at a temperature of 168K and pressure of 131.7 kPa (1000 torr). This temperature and pressure is assumed for all physical properties listed in this work unless otherwise noted.

A detailed review of scintillation calorimetry and optical properties of LXe can be found in [55].

2.2 Ionization in Liquid Xenon

Upon entering LXe, ionizing radiation scatters off of Xe atoms, creating δ-electrons, ions (Xe^+), and excited states, or excitons (Xe^*). δ-electrons further excite and ionize, creating additional δ-electrons until the energy of all δ-electrons drops below

Property	Value
Melting point	161.36 K
Boiling point	169.75 K
Triple point	161.41 @ 80.5 kPa
Critical point	289.8 K @ 5.84 MPa
Liquid Density	22.23 mol/liter
Gas Density @ boiling	0.097 mol/liter
L-G density ratio @ boiling	228.4
Density @ STP	0.044 mol/liter
Heat capacity	44.65 J/K-mol
G Heat capacity @ boiling	23.37 J/K-mol
Heat of vaporization	12.40 kJ/mol

Table 2.3: Thermodynamic properties of xenon at 168 K and 131.7 kPa (1000 torr), unless otherwise noted.

the excitation energy of Xe, at which point they are referred to as sub-excitation electrons. These sub-excitation electrons exist in the conduction band of LXe, which is separated from the ground state by a gap of energy E_g. The energy of the incoming radiation, E_0, is split among these channels according to

$$E_0 = N_i E_i + N_{ex} E_{ex} + N_i E_e \tag{2.1}$$

where N_i is the number of Xe^+ created, each with average energy cost E_i, N_{ex} is the number of Xe^* created, each with average energy cost E_{ex}, and E_e is the average kinetic energy of sub-excitation electrons. The W-value is a constant defined as the average energy required to produce one electron-ion pair, and is given by

$$W = E_0/N_i = E_i + E_e + (N_{ex}/N_i)E_{ex} \tag{2.2}$$

Theoretical and experimental values for the various parameters appearing in these equations are listed in table 2.4[14].

In order to correctly measure the number of electron-ion pairs produced, one must prevent recombination of electron-ion pairs by applying an external electric field. Experimentally, if an ionizing event occurs within an electric field $\mathcal{E}$ setup between

Property	Value
W	15.6±0.3 eV
W/E_g	1.68±0.3
E_g	9.32±0.07 eV
E_i/E_g	1.13
E_e/E_g	0.48
$(E_{ex}/E_g)(N_{ex}/N_i)$	0.05

Table 2.4: Quantities pertaining to ionization of LXe by penetrating radiation. Experimental and theoretical discussion of these values can be found in [14] and references therein.

two parallel plates,

$$W = \lim_{\mathcal{E}\to\infty} \frac{E_0}{Q(\mathcal{E})/e} \tag{2.3}$$

where $Q(\mathcal{E})$ is the charge collected at the anode, and e is the electron charge. $Q(\mathcal{E})$ varies not only with electric field, but with the type of radiation. Heavily ionizing particles, such as alphas, which penetrate LXe produce a cylindrical track with a dense core of electron-ion pairs which typically dominate the local electric field. Even at $\mathcal{E}$ = 20 kV/cm less than 10% of charge is collected[56], with the rest being lost to recombination. Conversely, minimum ionizing particles produce tracks with much lower ionization densities, allowing almost complete charge collection at $\mathcal{E} \sim$ 10 kV/cm[57]. This topic will be discussed in more detail in section 2.5.

The motion of sub-excitation electrons excited to the conduction band and corresponding ions left at the top of the valence band in LXe has been studied in [58, 59]. At very low fields ($\sim$100 V/cm) the electron drift velocity v_d varies almost linearly with field strength as

$$v_d \propto \mu_e \mathcal{E} \tag{2.4}$$

where μ_e is the electron mobility. For LXe μ_e was measured by Miller to be 2200 cm^2/s·V. For $\mathcal{E} > 10$ kV/cm the drift velocity saturates at 2.86×10^5 cm/s.

The ion drift velocity behaves linearly at all field strengths used in EXO-200. μ_{ion} was measured by Hilt to be 3.7×10^{-3} cm^2/s·V at 170 K, varying linearly with temperature by 0.02×10^{-3} cm^2/s·V·K.

The transverse diffusion of a cloud of electrons drifting over a distance d is given by

$$\delta = \sqrt{D_T d / v_d} \tag{2.5}$$

The transverse electron diffusion constant, D_T, has been measured in [60] to be 80 cm^2/s at 1 kV/cm, dropping to 50 cm^2/s at 10 kV/cm. The same work shows that the longitudinal diffusion coefficient is roughly 0.1 D_T.

2.3 Purity Effects on Electron Lifetime

Electrons excited to the conduction band can be captured by electronegative impurities in the LXe such as SF_6, N_2O, O_2, N_2, CO_2, and H_2O. This can affect the number of electron-ion pairs measured in an ionizing event by the reaction

$$e^- + S \rightarrow S^- \tag{2.6}$$

where S is the electronegative impurity. Ignoring any recombination, the rate of change of concentration of electrons drifting through contaminated LXe can be described by[61]

$$dN_e/dt = -k_s(\mathcal{E}) \cdot N_S \cdot N_e \tag{2.7}$$

Where $k_s(\mathcal{E})$ is the drift field dependent electron capture rate for S given in $M^{-1} \cdot s^{-1}$, and N_S and N_e are the molar concentrations of molecule S and electrons. The electron lifetime, τ_e, can then be defined as

$$\tau_e = -\left(k_s(\mathcal{E}) \cdot N_S\right)^{-1} \tag{2.8}$$

Values of $k_s(\mathcal{E})$ for SF_6, N_2O, and O_2 can be found in [61]. The value for O_2 (the most relevant contaminant for EXO-200 because of its presence in air) varies from 7×10^{10} at 1 kV/cm to 2×10^{10} at 4 kV/cm. Values of the capture rate for N_2, CO_2, and H_2O in LXe could not be found in the literature. Based on the ratio of the capture rates of N_2 and O_2 in LAr[62], and the similarity between LXe and LAr of capture rates of the contaminants SF_6, N_2O, and O_2[61], it is suspected that the

electron capture rate for N_2 in LXe is 1×10^{-2} - 1×10^{-4} that of O_2.

2.4 Luminescence in Liquid Xenon

The decay of excited dimers, Xe_2^*, to the ground state is responsible for luminescence, or scintillation, in LXe. Both Xe^* and Xe^+ can lead to excited dimers[60]. The first process (exciton de-excitation) involving Xe^* is

$$\begin{aligned} Xe^* + Xe &\rightarrow Xe_2^* \\ Xe_2^* &\rightarrow 2Xe + h\nu \end{aligned} \tag{2.9}$$

The second process (recombination), involving Xe^+ and sub-excitation electrons is

$$\begin{aligned} Xe^+ + Xe &\rightarrow Xe_2^+ \\ Xe_2^+ + e^- &\rightarrow Xe^{**} + Xe \\ Xe^{**} &\rightarrow Xe^* + heat \\ Xe^* + Xe &\rightarrow Xe_2^* \\ Xe_2^* &\rightarrow 2Xe + h\nu \end{aligned} \tag{2.10}$$

where *heat* is an infrared photon[63, 64], and $h\nu$ is a scintillation photon. At 160 K, the scintillation spectrum was found by Jortner[65] to have a peak value at 56180 cm^{-1} (178.0 nm), with FWHM = 4500 cm^{-1} (14.3 nm).

The de-excitation process described by equation 2.9 has two components with two different time scales[66]. De-excitation of singlet states produce a short decay time constant of 4.3 ns. De-excitation of triplet states produce a longer decay time constant of 22 ns. These time constants have been found to be independent of electron-ion density, though the ratio of singlet to triplet excited states is positively correlated with the latter. The recombination process (equation 2.10) has a non-exponential decay structure[67], initially following a time constant of 45 ns with a long tail extending $>\sim1\mu$s. As described in section 6.1, EXO-200 electronics have a 1 μs time resolution, so all components of the scintillation signal are effectively immediate.

Property	Value
N_{ex}/N_i	0.13±0.07
W_{ph}(max)	13.8±0.9 eV
$W_{ph}(\beta)$	17.9 eV
$W_{ph}(\alpha)$	21.6 eV

Table 2.5: Parameters describing scintillation yield in LXe[15]

Based on eqns 2.9 and 2.10, $N_i + N_{ex}$ scintillation photons are expected for each ionizing event. The W_{ph}-value is a constant defined as the average energy required for production of a scintillation photon assuming 100% recombination and no photon quenching. It is given by

$$W_{ph} = E_0/(N_i + N_{ex}) = W/(1 + N_{ex}/N_i) \tag{2.11}$$

In practice, a lower scintillation yield can be caused by the escape of sub-excitation electrons from recombination. According to the Onsager theory[68] electrons must thermalize within a distance from a Xe^+ less than the Onsager radius (49 nm for LXe) in order to recombine. The electron thermalization range in LXe is estimated to be 4000-5000 nm[69]. Thus in the absence of electric field, many electrons can escape the dense ionization region, recombining with ions up to ms later. These electrons are referred to as escape electrons.

Quenching can also suppress scintillation yield in regions of high exciton density. Hitachi et al.[70] devised a model in which free excitons undergo biexcitonic quenching

$$Xe^* + Xe^* = Xe + Xe^+ + e^- \tag{2.12}$$

The emitted electron carries away kinetic energy close to $h\nu$, which is then lost through thermalization prior to recombination.

Experimentally, it is found that escape electrons and quenching produce different values of W_{ph} for different species of incoming radiation. W_{ph} as given in eqn 2.11 is generally referred to as W_{ph}(max). The effective W_{ph} for betas and alphas ($W_{ph}(\beta)$, $W_{ph}(\alpha)$) are significantly higher. Table 2.5 lists empirically determined[15] values of

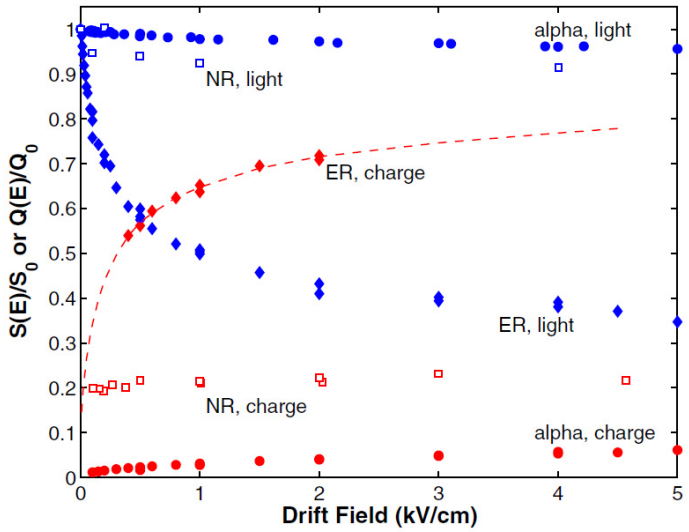

Figure 2.2: Macroscopic ionization-scintillation anti-correlation in LXe for 122 keV electron recoils (ER), 56.5 keVr nuclear recoils (NR) and 5.5 MeV alphas. S_0 is defined as the scintillation signal collected at no electric field. Q_0 is defined as the theoretical ionization signal collected at infinite electric field. Image reproduced from [19].

the various parameters relating to luminescence in LXe discussed here.

2.5 Drift Field Effects

The process described in eqn 2.9 has been shown to be independent of external electric field $\mathcal{E}$[66]. On the other hand participation of both positively charged Xe^+ ions and negatively charged sub-excitation electrons is required in the recombination process (eqn 2.10). Thus the recombination rate is strongly dependent on $\mathcal{E}$.

Based on these equations, in the absence of an electric field 100% of electron-ion pairs eventually recombine, and no charge is collected. As $\mathcal{E}$ increases, the likelihood of process 2.10 decreases, tending toward zero as the external field becomes infinite. Note that even in the limit as $\mathcal{E}\rightarrow\infty$, the scintillation signal does not go to zero due to field independent contributions from process 2.9. Thus, ionization signal increases and scintillation signal decreases with increasing external electric field, a property

referred to as macroscopic ionization-scintillation anti-correlation[20]. Figure 2.2[19] illustrates this property in LXe for various ionizing particles. Note in the figure the dramatically different scintillation and ionization signal ratios at low $\mathcal{E}$ for alphas and electrons, as described in section 2.2.

2.6 Energy Linearity

Eqns 2.2 and 2.11 imply that N_i and N_{ex} are directly proportional to the energy of the incoming radiation E_0:

$$\begin{aligned} N_i &= E_0/W \\ N_{ex} &= E_0(1/W_{ph} - 1/W) \end{aligned} \tag{2.13}$$

Thus, under the assumption that variations in ionization density, quenching, and electron escape effects are small, (true for minimum ionizing particles) ionization and scintillation yields are positively and linearly correlated with the energy of incoming radiation. These effects become significant for heavily ionizing particles, and their significance increases as the energy of these particles becomes small due to the Bragg peak.

2.7 Correlated Fluctuations Between Ionization and Scintillation

Statistical fluctuations in the production of ionization electrons due to an incident particle with energy E_0 can be modeled by a modified Poisson process first described by U. Fano[71]. Although equation 2.2 gives

$$N_i - E_0/W = 0 \tag{2.14}$$

this is a statistical statement, as W is defined as the average energy required to produce one electron-ion pair. A closer examination of the processes described in

section 2.2 reveals more about the statistics of energy deposition in LXe.

Equation 2.14 has thus far been applied for the full energy deposition of an incident particle, and it can be applied to each inelastic impact occuring during the energy deposition under the following assumptions:

1. The ionization and excitation processes are independent of the energy of the incident particle.

2. The ionization and excitation processes of the δ-electrons are not different from those of the incident particle.

With these assumptions, and making explicit the statistical nature of the processes, equation 2.14 can be re-written as

$$\langle n_p - \epsilon_p/W \rangle = 0 \tag{2.15}$$

where n_p is the number of electrons liberated in impact p, ϵ_p is the energy lost by the incident particle in the impact, and the average is taken over the large number of inelastic impacts of both the incident particle and δ-electrons.

The assumptions stated above imply that successive impacts are independent of each other. Thus, the mean statistical fluctuation in the production of ionization electrons by the incident particle can now be expressed as

$$N \left\langle (n_p - \epsilon_p/W)^2 \right\rangle = F N_i \tag{2.16}$$

where N is the total number of impacts in the ionizing event, given by $N_i/\langle n_p \rangle$, and F is the 'Fano factor', defined by:

$$F \equiv \left\langle (n_p - \epsilon_p/W)^2 \right\rangle / \langle n_p \rangle \tag{2.17}$$

Thus, assuming a perfect detector (all deposited energy is collected, electronic noise is negligible, there is no position dependence of detector response, etc), the

peak in the ionization spectrum can be described by a Gaussian distribution,

$$G(E) = \frac{A}{\sqrt{2\pi\sigma^2}} e^{-\frac{(E-E_0)^2}{2\sigma^2 W^2}} \tag{2.18}$$

where

$$\sigma = \sqrt{\frac{FE_0}{W}} \tag{2.19}$$

is the energy distribution width. F = 1 corresponds to a purely uncorrelated Poisson process. As described above, the Fano factor arises due to correlations caused by energy conservation (equation 2.14). That the Fano factor is different from zero indicates that energy is lost to modes other than the production of electron-ion pairs. In the treatment above, two such modes exist, namely the production of excitons and the kinetic energy of sub-excitation electrons. The Fano factor for LXe has been calculated to be 0.04 (0.06)[72], based on equation 2.17 and the Shockley[73] (Alkhazov[74]) model of ionization and excitation in noble liquids.

Energy resolution is a dimensionless measure of the accuracy of energy deposition measurements in a detector. It is defined as

$$R(E_0) = \sigma\frac{W}{E_0} = \sqrt{\frac{F_{eff}W}{E_0}} \tag{2.20}$$

where F_{eff} is an effective Fano factor. Since any real detector contains some amount of uncorrelated gausian noise (e.g. electronic noise from a charge amplifier), the noise subtracted energy resolution

$$R_{NS}(E_0) = \sqrt{\sigma^2 - \sigma^2_{Noise}}\frac{W}{E_0} \tag{2.21}$$

is more commonly used in referring to the intrinsic energy resolution of a detector medium. Any reference to energy resolution in this thesis assumes the noise subtracted value.

Experiment has repeatedly found effective Fano factors far larger than predicted ($\sim$50 vs. 0.04 as mentioned above). The reproducibility of the energy resolution measurements in a wide variety of experimental setup point toward an incomplete

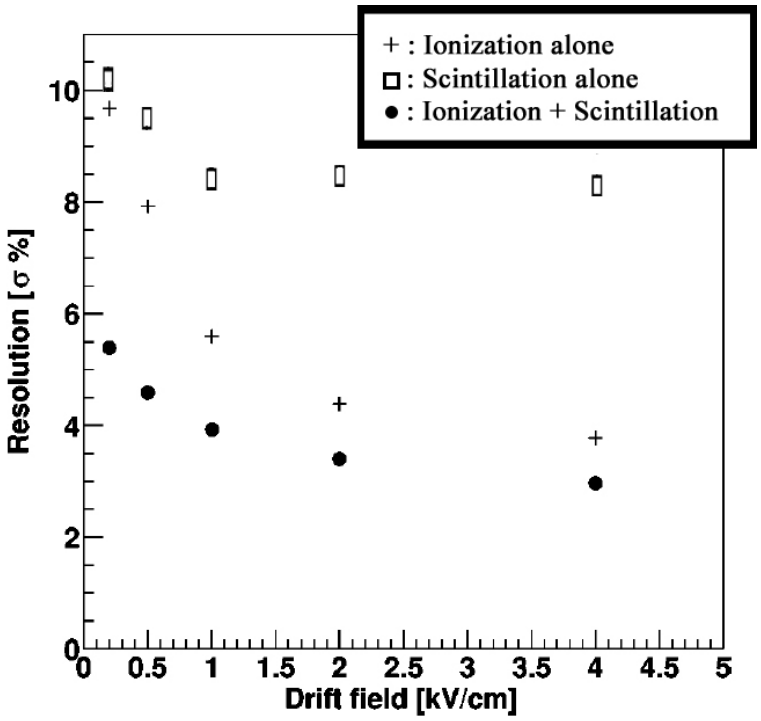

Figure 2.3: Energy resolution vs drift field strength for 570 keV gammas in LXe. Image adapted from[20].

understanding of correlations and energy loss in LXe.

A deeper look into the recombination process given by equation 2.10 reveals an explanation for some of this discrepancy and a method for improvement of energy resolution. As discussed in sections 2.2 and 2.5, the rate of recombination varies with incident particle type, energy, and external electric field. However, even for any given set of conditions, statistical event-by-event fluctuations in the rate occur about this average. If the recombination rate fluctuates slightly higher for a given event, more Xe^+ ions will recombine producing scintillation light, thus decreasing collected ionization charge and increasing collected scintillation light. In this way, statistical fluctuations in the recombination rate produce anti-correlated fluctuations in collected ionization charge and scintillation light event by event, refered to as microscopic ionization-scintillation anti-correlation. This anti-correlation can explain some of the discrepancies between theory and experiment described previously.

Ionization-scintillation anti-correlation was first shown to substantially improve LXe energy resolution in work by the EXO collaboration[20]. In this work, an effective Fano factor of 33 was measured using a combined analysis of scintillation and ionization signals. More recent work by Aprile[52] has shown that improved light collection further reduces the effective Fano factor to 12. Figure 2.3[20] shows energy resolution as a function of drift field strength for ionization and scintillation alone, and a combined measurement of ionization and scintillation.

The improvement in energy resolution made possible by this technique is taken advantage of in EXO-200. Using equation 2.19, the W-value listed in table 2.4 and a Fano factor of 12, one would expect an energy resolution of 0.87% at the ^{136}Xe $0\nu\beta\beta$ Q-value of 2.458 MeV. EXO-200 was conservatively designed assuming an energy resolution no worse than 1.5% will be achieved at 4 keV/cm, corresponding to an effective Fano factor of 35.

Despite these improvements, the experimentally measured energy resolutions in LXe are still inconsistent with prediction by a factor of 10 or more. It is possible that there exist further mechanisms for energy loss in LXe. Another possibility is that the assumptions given at the beginning of this section are inexact. As mentioned briefly in section 2.6, the Bragg curve of ionizing particles will result in higher and higher ionization densities as the particles come to rest. The heavier density results in a stronger local electric field, which can affect the ratio of scintillation and ionization as shown in section 2.5. Moreover, the total ionization density will depend on the number of impacts N, since the average δ-electron energy will decrease with increasing N. Modes such as these can potentially explain the discrepancy between theory and experiment.

2.8 Scattering Properties

Radionuclides decay primarily via gamma, beta, or alpha emission. Due to the very short interaction length of charged particles in matter (typically $\sim$1 mm), betas and alphas produced outside the LXe rarely enter the active volume of the detector. Thus the majority of EXO-200 backgrounds are gamma interactions. The topology

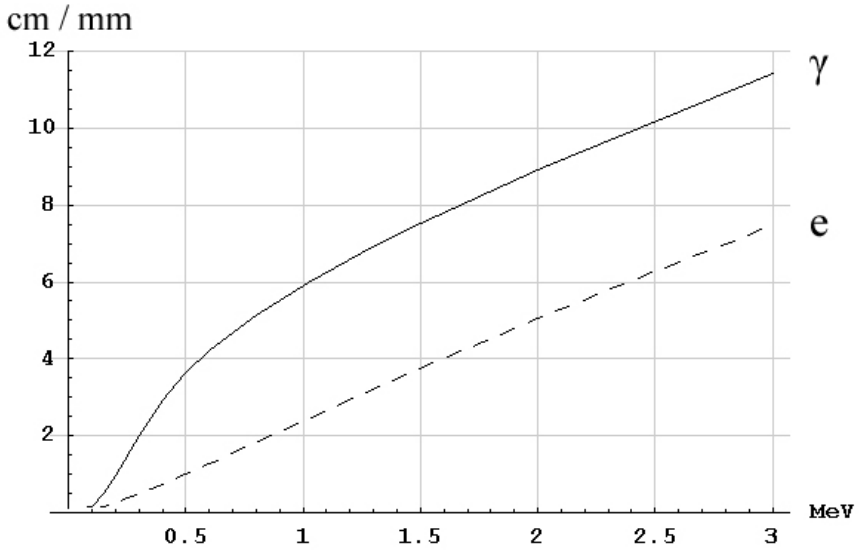

Figure 2.4: Mean free path of gammas, and the stopping distance of electrons, in LXe[21]. The vertical axis is in cm for gammas, and mm for electrons.

of gamma interactions in LXe can be used to distinguish them from the electrons emitted in $2\nu\beta\beta$ and $0\nu\beta\beta$ events, which can provide a powerful means of background rejection.

The mean free path of gammas in LXe is shown in figure 2.4. Also shown is the stopping distance (along the path) of electrons, which due to their charge effectively interact continuously in LXe. Electrons up to 3 MeV have a path length of up to 8 mm. Multiple scattering results in a total range of $\sim$2 mm. Gammas of similar energy have a mean free path of up to 12 cm. Thus in most cases, the interaction sites produced by gammas will be separated by many cm, whereas electrons produced by $\nu\beta\beta$ will deposit all energy within 1 cm of their production site. For this reason, EXO-200 was designed to measure the three-dimensional location of ionization sites with better than 1 cm position resolution. Rejection of all tracks longer than 2 cm has been proposed as a means of discriminating between $\nu\beta\beta$ and gamma backgrounds, though the exact implementation of such a cut will depend on as yet unknown experimental conditions such as signal to noise ratio.

Bremsstrahlung of betas in LXe creates inefficiency for such a background rejection technique. This process can produce gammas which travel many cm (or even leave the

active volume) before interacting. Thus, a small but significant number of $0\nu\beta\beta$ and $2\nu\beta\beta$ events can be rejected as background based on a strict track length criterion. The background rejection efficiency of this technique as implemented in the EXO-200 detector is discussed in section 4.6.

Chapter 3

Detector Design

Background minimization was the driving force behind every aspect of the design of EXO-200. This chapter will present an overview of the EXO-200 detector, and discuss the background considerations relevant to its overall design.

3.1 Design overview

EXO-200 employs a time projection chamber (TPC) in order to perform calorimetric and topologic measurements of energy depositions caused by radiation originating within and penetrating a LXe volume. A schematic of the EXO-200 detector is shown in fig. 3.1. Electrons and photons liberated by ionizing radiation passing through the LXe volume are collected by detector planes on either end of a cylindrical TPC, providing information on the location and magnitude of energy depositions in the LXe. The detector planes are each comprised of two elements. The elements closest to the center of the detector are optically transparent induction and electron collection grids. Behind these grids lies an array of Large Area Avalanche Photo Diodes (APDs). A high-voltage cathode grid at the center of the detector divides the TPC into two nearly symmetric halves, and establishes an electric field of up to 4 kV/cm within the active volume, allowing for collection of the liberated electrons. A series of field shaping rings maintain electric field uniformity between the cathode and detector planes. The potentials of the field shaping rings are graded by a chain

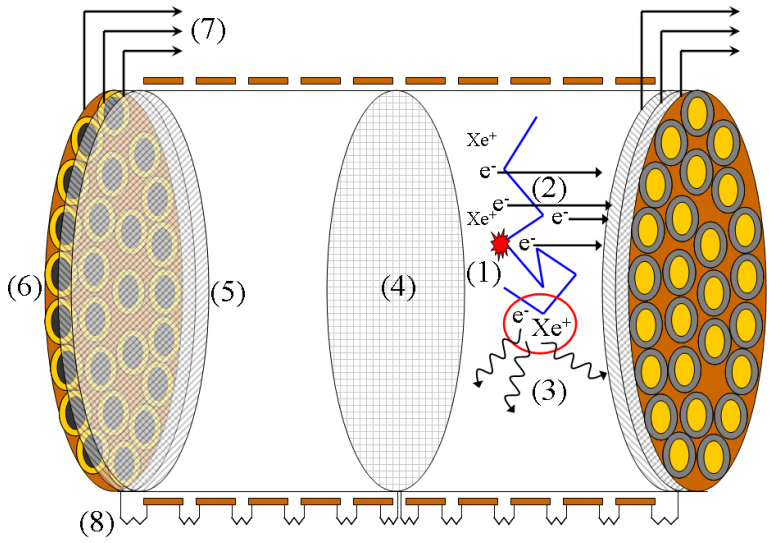

Figure 3.1: Schematic of the EXO-200 TPC. Electrons from a $0\nu\beta\beta$ energy deposition (1) produce electron-ion pairs (2), some of which recombine and release scintillation photons (3). A high-voltage cathode grid (4) creates an electric field, pulling liberated electrons toward a collection anode (5). Two arrays of APDs (6) collect scintillation photons. Flex cables carry signals to ionization and scintillation (7) readout electronics. A chain of field shaping rings and resistors (8) maintain electric field uniformity.

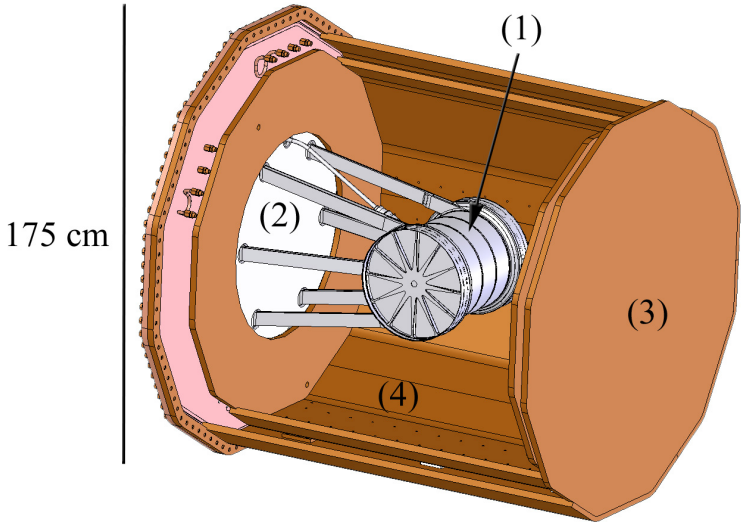

Figure 3.2: The LXe vessel (1) housing the TPC, welded to the inner hatch (2) of the double walled copper cryostat (3). HFE fills the inner volume of the inner cryostat (4).

of resistors which electrically link the cathode and anode. Ionization signals collected by the grids and scintillation signals collected by the APDs are carried out of the TPC to readout electronics by custom flexible cables.

The halves of the detector are inserted into opposite ends of a thin-walled copper vessel, which is cantilevered off the inner hatch of a double walled, vacuum insulated copper cryostat (see fig. 3.2). The volume of the inner cryostat is filled with 3M Novec Engineered Fluid HFE-7000[75] (here referred to as HFE). This fluid is extremely low in radioactive contaminants, liquid at both room temperature and LXe temperature, and serves as both heat transfer fluid and radioactive shielding. Three commercial refrigerators remove heat from the inner cryostat via three heat exchangers welded along the top of it. Feedthroughs on the hatches of the inner and outer cryostats allow the passage of xenon, HFE, and refrigerant into and out of the cryostat.

The inner vessel of the cryostat is surrounded by super-insulation (aluminized mylar). The volume between the inner and outer vessels of the cryostat, referred to the as the Vacuum Space, is maintained at less than 1×10^{-4} torr by a redundant system of dry scroll and turbo molecular pumps.

The cryostat is surrounded by 25 cm of lead (see fig 3.3). An aluminum and painted steel structure supports the lead shielding. Small lead bricks in the front wall allow the various feedthroughs on the outer cryostat hatch to penetrate the shield. Two electronics chassis receive cables from the two halves of the detector, and are located just outside the front wall. A second lead wall, located just beyond the electronics chassis, blocks radiation that would otherwise travel through the penetrations in the first wall.

Detector shielding prevents trace radioactive contamination in external objects (mostly the surrounding rock, but also the cleanroom, plumbing systems, people, etc) from contributing to background. The lead shielding is the primary shield, designed to allow no more than one $0\nu\beta\beta$ background event/year from external objects in conjunction with other shielding. The HFE also serves as a very significant shield, providing roughly a factor of 1000 suppression in background impact of any component external to it. It is much more radio-pure than the lead shielding, and provides shielding from the trace contamination present in the lead. See sections 5.1 and 5.6

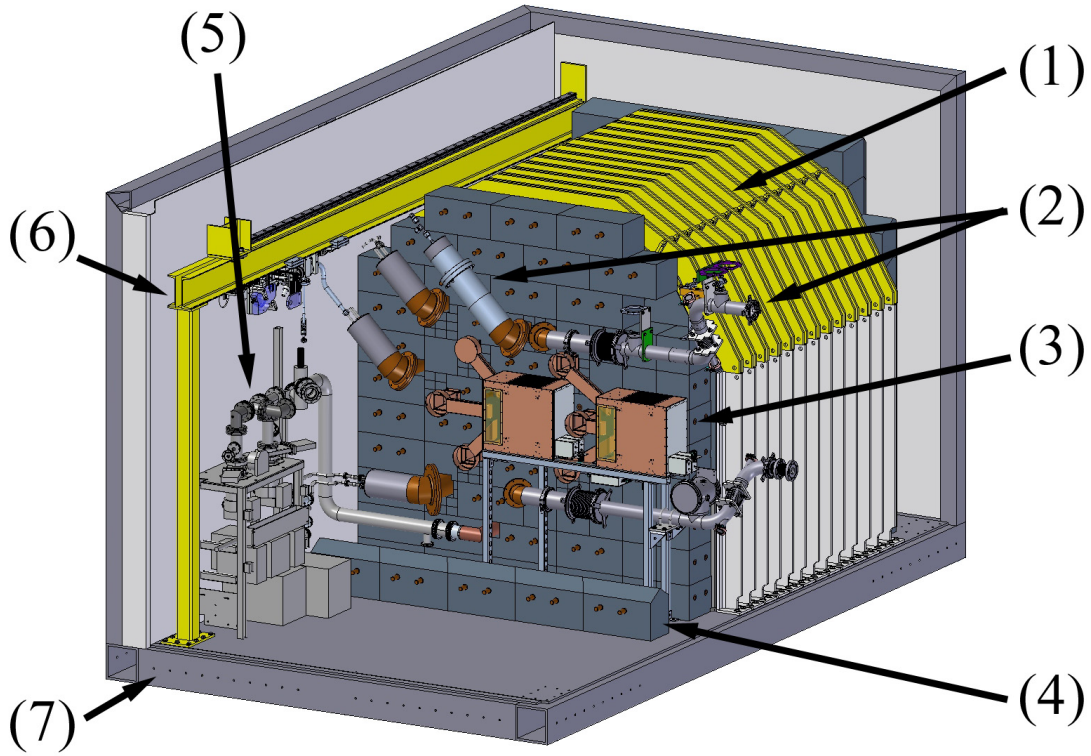

Figure 3.3: The outside of the EXO-200 detector. A lead shield supported by an aluminum and painted steel structure surrounds the cryostat (1). Smaller lead bricks allow cryostat feed throuhgs (2) to penetrate the front lead wall. The two electronics chassis (3) are located between the front wall and the second lead wall, only partially shown (4). A vacuum system (5) maintains vacuum in the Vacuum Space between the inner and outer cryostat. A crane (6) built into the class-100 cleanroom (7) allows construction of the detector.

for details on these components.

The HFE is delivered to and from the cryostat via a liquid handling system, referred to as the HFE System. Prior to filling the cryostat the HFE is stored in a dewar, referred to here as the HFE dewar. Nitrogen gas pushes the HFE through a 0.1 micron filter and into either the inner cryostat or an actively heated and cooled ballast bottle, exterior to the cryostat. The ballast bottle is used to control the pressure in the inner cryostat once the cryostat is full (see section 5.4).

Xenon is delivered to and from the LXe vessel via a liquid and gas handling and purification system, referred to as the Xenon System. The system includes a circulation loop, which is used to boil LXe from one side of the LXe vessel, purify it using commercial purifiers, then re-condense it into the other side of the vessel. The system is also constructed to regulate the pressure in the LXe vessel on a timescale of 1 sec, ensuring that the differential pressure across the LXe vessel is always less than 250 torr (in most cases it is kept less than 15 torr). Commercial compressors are used to transfer the Xe back into standard gas bottles.

The entire experiment is located in a class-100 clean room, 2150 ft (1700 m.w.e) underground at the Waste Isolation Pilot Plant (WIPP) near Carlsbad, New Mexico.

3.2 Backgrounds

Figure 3.4 illustrates the many sources of background for the EXO-200 experiment. These backgrounds fall into one of two categories, each of which will be described in detail in this section:

1. Primordial radioactive isotopes and their daughters.

2. Cosmic ray muon induced.

3. Man made isotopes (e.g. ^{85}Kr, ^{137}Cs).

Decay of primordial radioactive isotopes and their daughters is the largest contributor to the EXO-200 background. These radioactive isotopes are present throughout the Earth's crust, oceans, and atmosphere, and can thus be found in some quantity

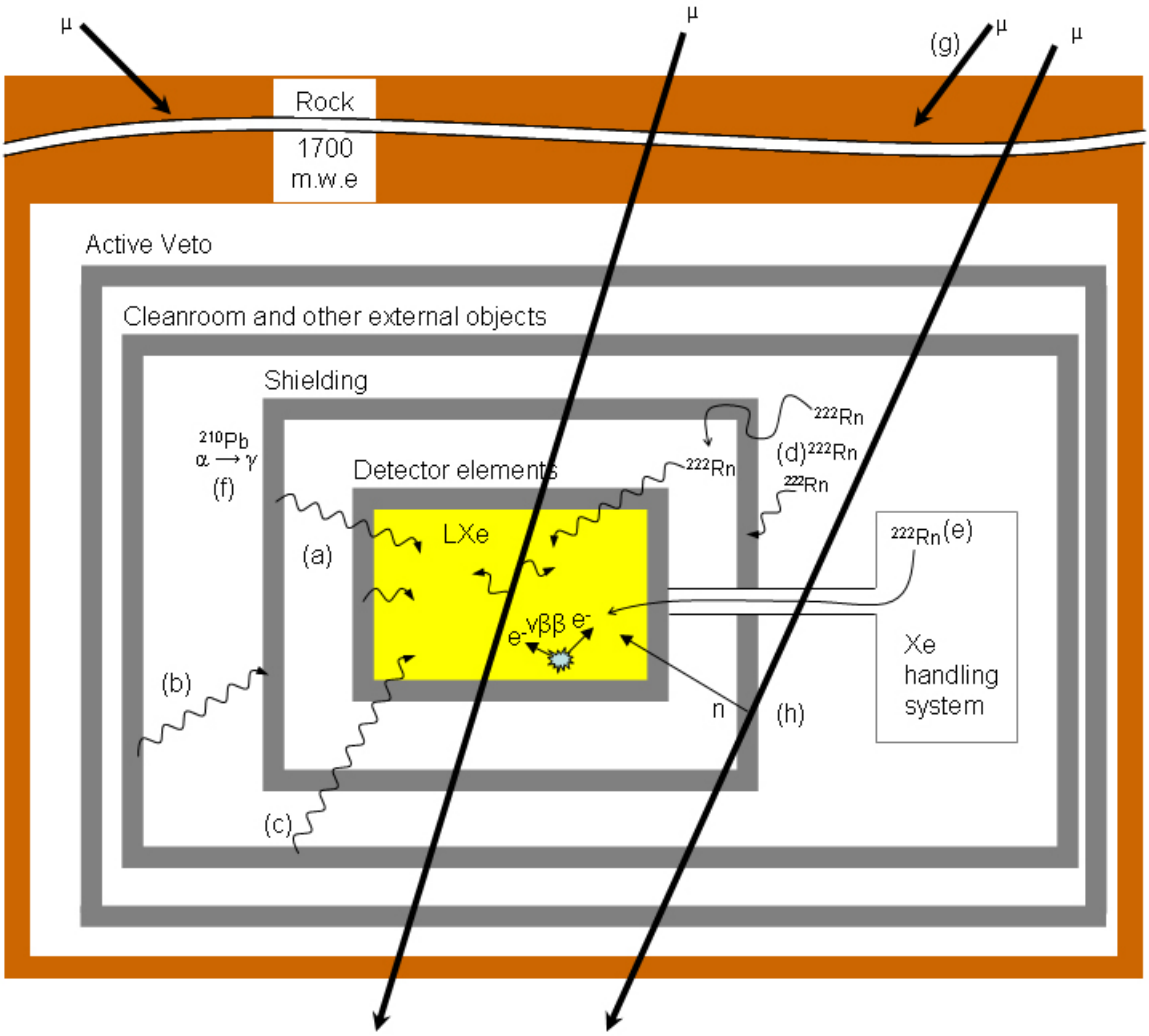

Figure 3.4: The various sources of background for EXO-200. (a) The largest source of background is from contamination of internal detector elements, including shielding. Contamination can be intrinsic, can adhere to surfaces, or can be cosmogenically activated. (b) Shielding stops essentially all external radiation from entering the detector. (c) Shielding thickness was chosen such that $<$ one external $0\nu\beta\beta$ background event/year would be recorded. (d) Gaseous ^{222}Rn poses a unique background, particularly if it seeps through cracks in the lead shielding. (e) ^{222}Rn emanated from Xe System plumbing can enter the detector and contribute to background. (f) ^{210}Pb is a significant contaminant in the lead shielding. (g) The effects of cosmic ray muons are mitigated by 1700 m.w.e. overburden and an active veto system. (h) Cosmic ray muons can produce spallation products which can enter the LXe.

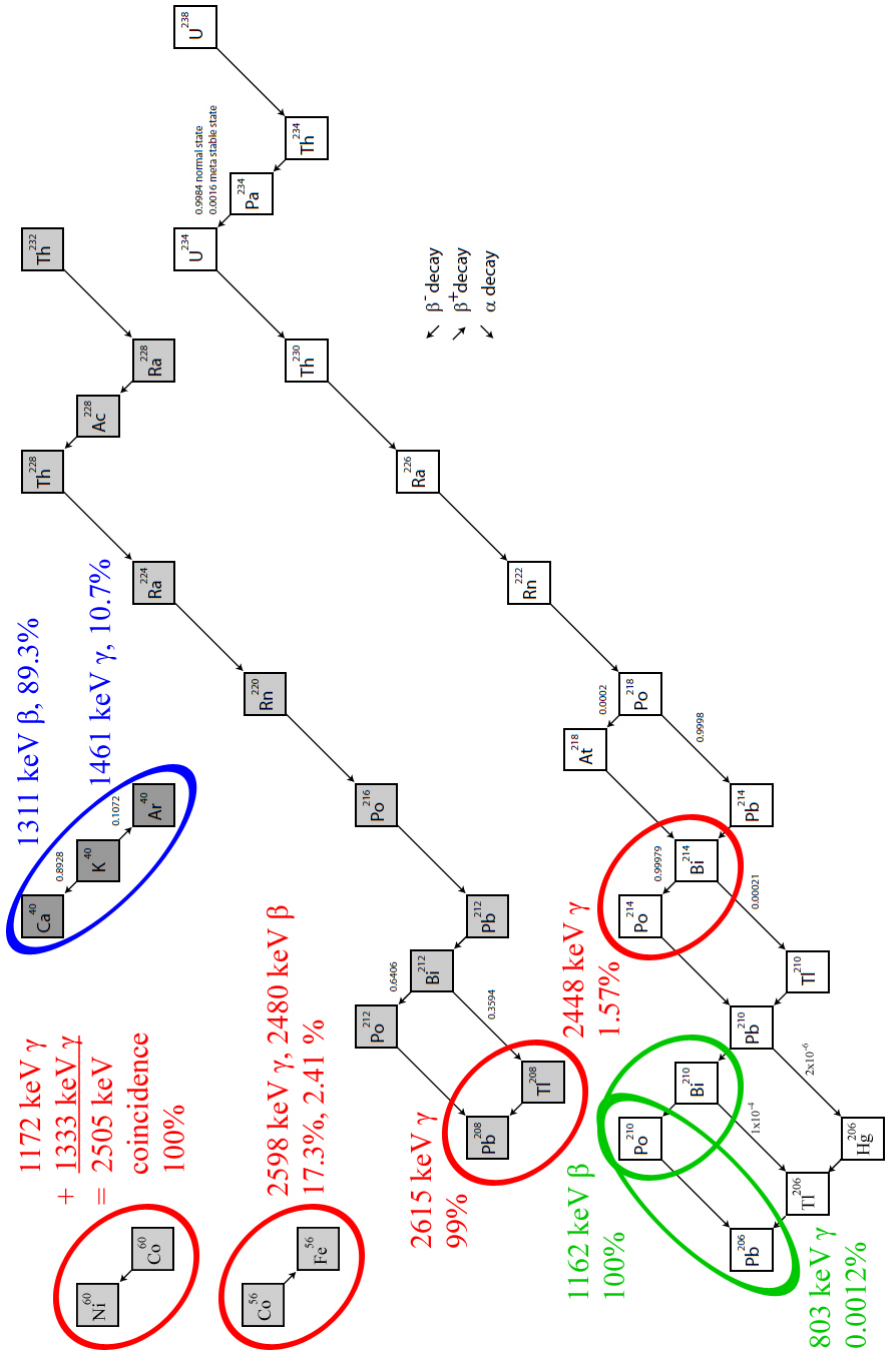

Figure 3.5: Decay chains of primordial radioactive contaminants, and the cosmogenically activated contaminants relevant to the $0\nu\beta\beta$ background. Lines of particular concern for the $0\nu\beta\beta$ signal are highlighted in red. The ^{40}K chain is high lighted in blue. Significant lines in the ^{210}Pb chain are highlighted in green.

Isotope	Half-life [yr]	Average crustal concentration [ppm]
^{40}K	1.28×10^{9}	2.0
^{232}Th	1.41×10^{10}	10.7
^{238}U	4.47×10^{9}	1.5

Table 3.1: Half-lives and concentration of the three most common primordial radioactive isotopes[16].

in the bulk and on the surface of all materials. Most of the primordial radioactive isotopes found in the Earth's crust today are one of three isotopes listed in table 3.1[16]. The decay chains of these isotopes are shown in figure 3.5.

^{40}K will undergo beta or inverse beta decay. The Q-value of these reactions is 1311 keV (89.3% branching ratio) and 1505 keV (10.7% branching ratio) respectively, and both decays result in stable daughter nuclei. There is no contribution to the $0\nu\beta\beta$ background from ^{40}K since the Q-values of its decays are less than the $0\nu\beta\beta$ Q-value.

^{232}Th and ^{238}U have much more complex decay chains. Gammas, betas, and alphas produced throughout each decay chain can contribute to the $2\nu\beta\beta$ and $0\nu\beta\beta$ backgrounds. The decays which contribute most heavily to $0\nu\beta\beta$ background are those which emit gammas that lie within the $0\nu\beta\beta$ energy window. These gammas, highlighted in red in figure 3.5, can penetrate into the LXe before scattering and produce a sharp line at or near the $0\nu\beta\beta$ Q-value rather than the relatively flat spectrum produced from Compton scattering and Bremsstrahlung, making them much harder to distinguish from the sharp line one expects from $0\nu\beta\beta$.

Details of the primordial contamination and predicted background contribution of every major component of the detector are presented throughout chapters 4 and 5.

^{222}Rn and ^{210}Pb are two isotopes of the ^{238}U decay chain which pose unique problems. ^{222}Rn has a half-life of 3.8 days, and is a gas at STP. Some of the ^{222}Rn that is continuously produced in the Earth's crust via ^{238}U decay diffuses into the atmosphere. This atmospheric ^{222}Rn can then seep through cracks in the lead shielding of EXO-200, and decay in the small gap that exists between the cryostat and lead. The location of ^{222}Rn in the decay chain is upstream of ^{214}Bi, an isotope with a Q-value for

decay that is within 10 keV of the $0\nu\beta\beta$ Q-value. Thus, significant $0\nu\beta\beta$ background can result from these decays. Results from simulation of this background source, and a proposed method of eliminating the source, are presented in section 5.6.

In addition to the above problem, decays of ^{238}U occurring inside the xenon system can cause ^{222}Rn to slowly seep into the Xe, a process known as radon emanation. The ^{222}Rn can originate from components of the TPC itself (details in section 4.6), or be carried into the active volume of the TPC by circulating Xe if generated in the xenon system plumbing (details in section 5.5).

^{210}Pb poses a different challenge. It is located lower in the ^{238}U decay chain than ^{222}Rn (indicated in green in figure 3.5), and has a half-life of 22.3 years. As a solid metal, ^{210}Pb created by atmospheric ^{222}Rn decay tends to plate on solid surfaces. Its half-life is long enough that significant build up is possible during handling of detector components, and short enough that even small build-up has sizeable specific activities, and can significantly impact background. For this reason, the TPC components and interior of the LXe vessel were stored in an atmosphere of boil-off nitrogen during fabrication, limiting their exposure to fresh ^{222}Rn contaminated air. Details of this source of background are presented in section 4.6. The decay of ^{210}Pb is not energetic enough to contribute to the $0\nu\beta\beta$ background, but can affect the $2\nu\beta\beta$ measurement.

Finally, there exists a significant concentration of ^{210}Pb in the Earth's crust due to the decay of ^{238}U. When elemental Pb is extracted from Pb ores, this natural abundance of ^{210}Pb is extracted along with the stable Pb isotopes. Thus, the bulk concentration of ^{210}Pb in the lead shielding can be significant. Details of this source of background can be found in section 5.6.

Cosmic ray muons can also contribute significantly to the EXO-200 backgrounds. At sea level the cosmic ray muon flux varies depending many factors such as latitude, and is roughly 1×10^{-2} s$^{-1}\cdot$cm$^{-2}\cdot$sr^{-1}. There are three modes by which cosmic ray muons contribute to the background. The first is direct interaction with the LXe volume. The total flux of cosmic ray muons at the underground site was measured to be 3.1×10^{-7} s$^{-1}\cdot$cm$^{-2}\cdot$sr^{-1}[76]. As charged particles, muons effectively ionize continuously while passing through LXe (as opposed to gammas, which can travel many cm before interacting). They deposit at least 2 MeV/g$\cdot$cm^2 as they travel. In addition,

due to their mass, their momentum changes relatively little with each ionizing interaction. Thus muons passing through the detector produce very energetic straight tracks originating from the outside of the detector, and are very easily distinguished from $0\nu\beta\beta$ based on the event topology and quantity of energy deposited.

The second mode is via spallation neutrons generated by muons passing near the detector. As a muon travels through matter, it scatters off nuclei and can release neutrons with energies varying from sub-eV to many GeV[77]. Neutrons with $\sim$MeV of energy can penetrate into the LXe and contribute to the $2\nu\beta\beta$ or $0\nu\beta\beta$ backgrounds. This background mode, and the active veto system designed to suppress it, are discussed in section 5.6.

The third mode is via short lived ($T_{1/2} \sim 1$ yr) isotopes generated by the interaction of cosmic ray muon spallation with bulk detector materials. Once produced, these isotopes can decay during the life-time of the experiment. The majority of these isotopes are generated during fabrication and handling of materials on the surface of the Earth, where the cosmic ray muon flux is much higher than it is underground. Copper, comprised of ^{63}Cu (69% abundance) and ^{65}Cu (31% abundance), is the only material used in EXO-200 with activation produced at a high enough rate, and that decay with high enough energy, to contribute to the EXO-200 backgrounds. Decays of the isotopes ^{54}Mn, ^{56}Co, ^{58}Co, ^{59}Fe, ^{60}Co, and ^{65}Zn, generated by (n,α) and (p,n) reactions on Cu, contribute to $2\nu\beta\beta$ decay. Only decays from ^{56}Co and ^{60}Co are energetic enough to contribute to the $0\nu\beta\beta$ background. Relevant gamma lines from these two isotopes are indicated in figure 3.5. Details on the production rates, half-lives, and background impact of all of the isotopes can be found in section 3.7. Reducing the cosmic ray muon flux (and hence nucleon spallation flux) by fabricating, handling, and storing copper components under an overburden is the only means of suppressing the accumulation of these isotopes. The impact of the activation of major copper components to EXO-200 backgrounds can be found in sections 4.5 and 5.2.

^{85}Kr is a radioactive gaseous fission product released into the atmosphere in significant quantities during nuclear testing in the late 1900's. Its presence is significant only in that it can dissolve in the HFE when the HFE is manufactured, and hence can get very close to the TPC. ^{137}Cs is another fission product now found in significant

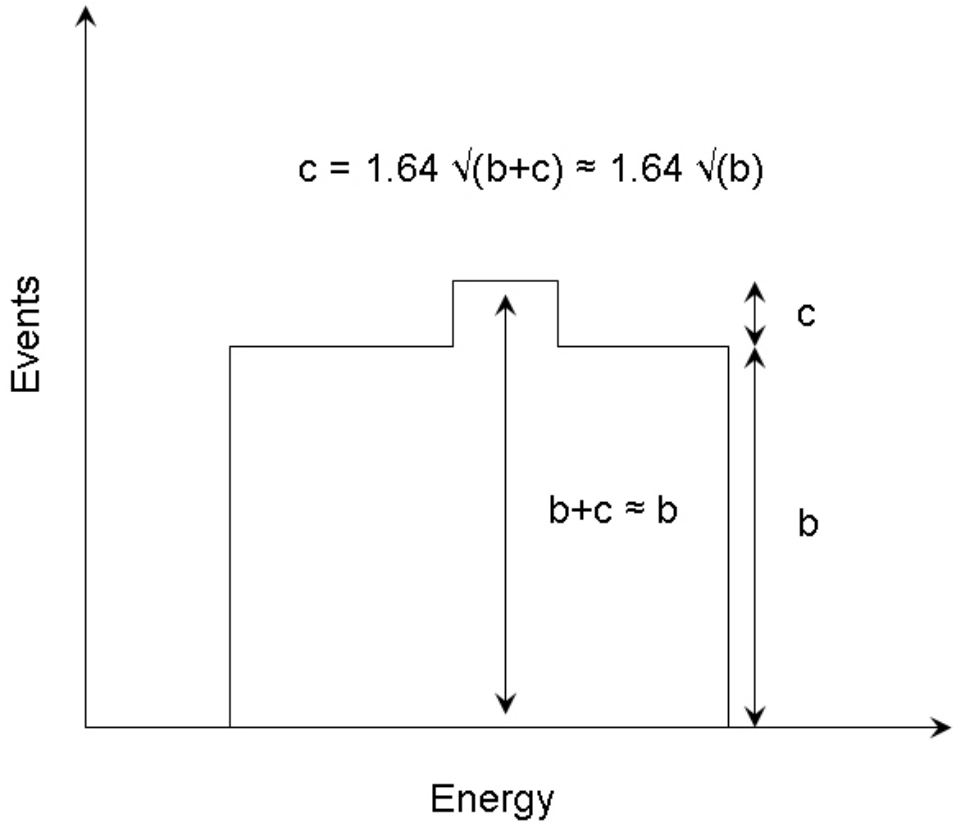

Figure 3.6: The derivation of equation 3.1. b refers to the predicted background, c to the predicted $0\nu\beta\beta$ signal.

quantities on the surface of the Earth due to nuclear testing, though its presence negligibly affects EXO-200 backgrounds.

3.3 Experimental Sensitivity

In a background dominated $0\nu\beta\beta$ experiment, and assuming gaussian statistics, the 90% CL sensitivity to $T_{1/2}^{0\nu\beta\beta}$ in the absence of signal can be expressed in terms of experimental parameters as

$$T_{1/2}^{0\nu\beta\beta} = (2.5 \times 10^{26}/mol) \left[\frac{a\epsilon}{A}\right] \left[\frac{MT}{b\Delta E}\right]^{1/2} \tag{3.1}$$

where A is the molecular weight of the source material in g/mol, a is the isotopic abundance, ϵ is the detector efficiency for $0\nu\beta\beta$, b is the number of background events per (kg·yr·keV), ΔE is the energy window for $0\nu\beta\beta$ decay in keV, M is the mass of isotope in kg, and T is the live time of the experiment in yr. This can be derived easily by taking the ratio of the $0\nu\beta\beta$ signal and the statistical error in background (approximately the square root of the background in a background dominated experiment) and setting it equal to 1.64 (90% CL) (refer to figure 3.6. In the calculations below, ϵ is assumed to be 1.

The total background tolerance used in designing and constructing the experiment was set based on a back-of-the-envelope estimation. Other low background experiments (for example SNO, Gotthard, Borexino) have obtained detector materials with ^{232}Th and ^{238}U contamination levels of order 1 ppt. If one assumes this contamination level, the ^{214}Bi decays in a 10 kg LXe vessel would produce roughly 30 $0\nu\beta\beta$ background evt/yr. This is the quantity used as the total background tolerance allowed within the $0\nu\beta\beta$ window, defined as 2384 keV - 2532 keV (Q $\pm$ 2σ).

The best lower limit on the half-life of $0\nu\beta\beta$ is roughly 1500 times higher than limit for the half-life of $2\nu\beta\beta$ of ^{136}Xe. Thus the background tolerance allowed within the $2\nu\beta\beta$ window, defined as 400-2000 keV, was set to 40k evt/yr.

As built, the active xenon mass of EXO-200 is 114.7 kg. Based on 30 background evt/yr, eqn 3.1 predicts a sensitivity to $T_{1/2}^{0\nu\beta\beta}$ of 4.4×10^{25} yr (90% CL) within two years, corresponding to a Majorana neutrino mass of $0.148^{+0.079}_{-0.038}$ eV using RQRPA NMEs. With these assumptions, two years of data will be sufficient to verify or reject the claim of observation by the Heidelberg-Moscow experiment at 1.1σ - 10.4σ confidence level (8.8 - 141 events on top of 60 background).

Given a background of 60 events over two years, an analysis using gaussian statistics is relatively precise. A more exact analysis using Poisson statistics reveals a 90% CL sensitivity to $T_{1/2}^{0\nu\beta\beta\_Xe}$ of 4.3×10^{25} yr, a 2.8% decrease when compared to gaussian statistics. A refined sensitivity analysis, based on detailed detector geometry and both measured and simulated detector characteristics, is presented in chapter 7.

3.4 Material Qualification

Achieving tolerable background rates within the $0\nu\beta\beta$ and $2\nu\beta\beta$ energy windows requires, among other things, that the lead shielding and all materials located within it be selected for very low intrinsic concentrations of the primordial radioactive impurities. Generally acceptable impurity levels in detector materials are of order pg/g for ^{238}U and ^{232}Th and ^{40}K, though specific tolerable impurity levels vary greatly with material quantity and location. As previously mentioned, in the case of the lead shielding bulk contamination of ^{210}Pb is also a concern.

Six techniques were used for measuring intrinsic radioactive contamination of detector materials and components: Neutron Activation Analysis (NAA), Gas Discharge Mass Spectrometry (GD-MS), Inductively Coupled Plasma Mass Spectrometry (ICP-MS), low background gamma spectrometry (also referred to as direct counting), alpha counting, and ^{222}Rn counting. The applicability and sensitivity of each technique is briefly described here. A more detailed discussion can be found in reference [78].

NAA is a method of bombarding a sample with thermal neutrons, then observing gamma emissions from resulting conversion of stable or very long-lived nuclei to relatively short-lived ($T_{1/2}\sim$days), activated isotopes. The method can achieve sensitivities as low as 0.1 pg/g, depending on the neutron cross section of the contaminant in question. Even better sensitivities are possible if pre-concentration techniques are used. Detection of ^{40}K, ^{232}Th, and ^{238}U contamination take advantage of the following reactions:

$$\begin{aligned} n + {}^{41}\mathrm{K} \rightarrow {}^{42}\mathrm{K} &\rightarrow {}^{42}\mathrm{Ca} \qquad T_{1/2} = 12.36h, \sigma = 1.2b \\ n + {}^{232}\mathrm{Th} \rightarrow {}^{233}\mathrm{Th} \rightarrow {}^{233}\mathrm{Pa} &\rightarrow {}^{233}\mathrm{U} \qquad T_{1/2} = 27.0d, \sigma = 6.1b \\ n + {}^{238}\mathrm{U} \rightarrow {}^{239}\mathrm{U} \rightarrow {}^{239}\mathrm{Np} &\rightarrow {}^{239}\mathrm{Pu} \qquad T_{1/2} = 2.36d, \sigma = 2.3b \end{aligned} \tag{3.2}$$

The half-lives shown apply to the final steps in each chain, which is the process observed via gamma ray spectroscopy after neutron activation. The cross-sections shown are for the initial reaction. Note that in the case of ^{40}K, NAA actually detects the presence of ^{41}K, which is a stable isotope of K with a factor 575 larger abundance

than ^{40}K.

Typically NAA is done using the very high neutron fluence in the core of a research reactor. EXO-200 used neutrons produced at the MIT Reactor Lab[79]. The neutron flux was measured using samples spiked with a known concentration of ^{40}K, ^{232}Th, or ^{238}U and irradiated together with the unknown samples. At a reactor power of 4.8 MW, a thermal neutron fluence of $(3.832\pm0.233)\times10^{13}$ cm^{-2}·s^{-1} was measured. Given this reactor power, the activity amplification factors achieved are (843, 1.6, and 2.3)$\times10^5$/hr of irradiation for the cases mentioned above, though these amplification factors drop exponentially with any delay between irradiation and measurement. NAA is generally suitable for plastics and other low-Z materials. It is inapplicable when the primary constituent of the material activates, as is notably the case for Cu, Pb, Au, Pt, and Al. Finally, NAA is destructive, making analysis of the specific parts used in the detector impossible.

Mass spectrometry is generally faster and less expensive than NAA. In Glow-Discharge Mass Spectrometry, the sample forms the cathode in a low pressure plasma. An ionized discharge gas (typically Ar) is accelerated towards the sample with energies of 0.1 - 1.0 keV. Resulting sputtered neutral species escaping the cathode surface and diffusing into the plasma are ionized and mass spectrometry is performed. GD-MS requires that the sample be a conductive or semi-conductive solid, and can achieve sensitivity to 1 pg/g. Thus it can analyze many of the metals that NAA cannot.

In Inductively Coupled Plasma Mass Spectrometry, Ar is loaded into an induction coil supplied with RF current, producing a plasma. The plasma surrounds tube in which a second flow of cooler Ar passes. Samples are dissolved into liquid form, usually using HNO_3, nebulized, and introduced to the cooler tube. At the prevailing temperatures, the sample ionizes and mass spectrometry is performed. ICPMS can achieve sensitivities of $\sim$1 pg/g. This sensitivity can be pushed up to 0.001 pg/g, but only if pre-concentration procedures are used. It also requires samples that are soluble in HNO_3 or other acids.

It is important to note that NAA, GD-MS, and ICP-MS directly measure the concentration of ^{232}Th and ^{238}U, and rely on the assumption of secular equilibrium

in the decay chains to predict the total background contribution that may be dominated by other isotopes, introducing additional uncertainties into the measurement. Direct gamma counting is an alternative that does not require this assumption. In this method, a p-type coaxial germanium detector run by the EXO collaboration in the Vue-del-Alpes underground laboratory in Switzerland was used to simply count the number of radioactive gamma emissions from samples. Since the activity of components going into the EXO-200 detector are expected to be on the order of μBq, direct counting can provide a relevant measurement only if the sample is counted for very long (years), or the sample mass is much larger then that going into the EXO-200 detector. Typically masses 100 times that used in the EXO-200 detector were counted, reducing the counting time from years to days. Thus this method is generally used on small, bulk components such as screws. In addition this method was used to occasionally normalize other measurement techniques. Advantages over NAA and MS include that is not destructive to the sample material, and that there are no restrictions on material type.

A special technique was used to measure ^{210}Pb contamination in the lead shielding. An ion-implanted silicon detector was used for detection of the 5304 keV alphas from ^{210}Po, a decay product of ^{210}Pb (see figure 3.5).

Finally, the ^{222}Rn emanation of major components installed in the xenon system were assessed using an electrostatic counter. The counter uses an inert gas (usually N_2) to guide radon atoms emanated from a sample into a counting chamber. There, a photodiode held at HV attracts the negatively charged decay products of ^{222}Rn. Once collected, the alpha decays of these isotopes are detected, and the ^{222}Rn emanation rate of the sample is inferred.

Over 300 materials and components were measured using these techniques. An extensive table of results from this materials qualification campaign can be found in reference [78]. Results pertaining to major detector components will be presented in chapters 4 and 5.

Design of the EXO-200 detector began with a rough selection of possible detector materials based on data from past experiments (for example, stainless steel was rejected in favor of copper, massive and relatively radioactive photomultiplier tubes

were rejected in favor of far lighter and radio quiet Avalanche Photodiodes (APDs), etc). Acceptable levels of contamination in bulk materials were then achieved by sampling and choosing the best manufacturer and lot from a large selection. In the case of complex detector components, such as flex cables, grid wires, or APDs, the number of manufacturers producing the desired component was low, and initial purity requirements were rarely met. Instead, extensive effort went into supervising and modifying the fabrication process of these components in order to minimize the impurity levels. Even in the case of suitably pure bulk materials (e.g. copper for the TPC), extreme care was required to ensure contaminants were not introduced during the processing of the material (machining, welding, etc). These unique efforts pertaining to particular detector components are described in relevant sections of chapters 4 and 5. Contamination measurements were performed at various steps in the handling and fabrication of final parts, allowing isolation of the sources of contamination and an understanding of ultimate contamination levels.

3.5 Surface Contamination

Surface cleanliness of all detector components was an essential consideration, both in minimizing ultimate background rates and in analyzing intrinsic contamination. Great effort was put into minimizing contamination of this kind and ensuring consistency in measured and installed components. First, a standard cleaning procedure was developed and used on the majority of detector components:

1. Rinse using acetone, a degreasing solvent (small parts underwent ultrasonic cleaning while immersed for 15 minutes, followed by a rinse with fresh solvent). Materials attacked by acetone did not receive this treatment.

2. Rinse using ethanol, a less aggressive degreasing solvent (small parts underwent ultrasonic cleaning while immersed for 15 minutes, followed by a rinse with fresh solvent). Isopropanol was substituted for ethanol when cleaning materials attacked by ethanol. Ethanol or isopropanol is used because both can be purchased commercially in a form more pure than acetone.

3. 0.5M - 1.5M HNO_3 rinse. Copper and copper based alloys underwent the more dilute treatment. In some cases, 1-2M HCl was substituted (for example in the flexible cables due to the very small thickness of the copper traces).

4. Deionized water rinse.

The acetone and ethanol rinses dissolve and remove organic contaminants, primarily oil, grease, and macroscopic dust and dirt. Semiconductor-grade chemicals were used. The acid and water rinses dissolve and remove metallic and ionic contaminants. The HNO_3 and HCl used were 15.8 molar and 11.7 molar trace-metal grade purchased from Fisher Scientific, and diluted using deionized water filtered on site with measured resistivity of 18 MΩ-cm.

The efficacy of this cleaning procedure is evident in the most stringent limits set by our most sensitive contamination measurements. In addition, efficacy was measured directly by wipe testing. Whatman Grade-42 filter papers[80] were used to soak up 0.1 molar HNO_3 spread over 0.1 m^2 of treated and untreated copper. Radioactive analysis of these filter papers revealed a 95% reduction in the surface contamination of the treated copper as compared to the untreated copper.

The cleaning procedure outlined above was followed as consistently as possible. Some materials and components required a modified cleaning procedure, depending on material properties and level of contamination. These exceptions are noted throughout chapters 4 and 5. In all measurements of finished EXO-200 parts, surface treatment of analysis samples was identical to treatment of installed components.

3.6 Monte Carlo

A Geant3[81] Monte Carlo was used to translate measured sources of radioactive backgrounds to $0\nu\beta\beta$ and $2\nu\beta\beta$ background impacts for EXO-200. Due to the scale of the qualification campaign, the simulation was designed for speed and on-demand construction decisions. The simulation geometry included all major components within and including the lead shield, and was accurate up to the millimeter scale. Muon veto panels were also simulated. Detailed detector response was not simulated. Only

the locations and magnitudes of energy depositions above detection threshold (400 keV) and within the active volume and muon veto was recorded. Detector spatial resolution was simulated by smearing location information with σ = 1cm. Energy resolution and electronic noise were similarly simulated by smearing energies with $\sigma = (0.015 \cdot \mathrm{E} + 800\ e^- \cdot 12.1\mathrm{eV}/e^-)$. Physics beyond the energy deposition was not considered (specifically, ionization and scintillation deposition modes were not distinguished, and otherwise significant factors such as attenuation length, reflectivity, and electric field strength were ignored). Only simple counting of energy depositions within the $0\nu\beta\beta$ and $2\nu\beta\beta$ windows, defined as 2458±74 keV and 400-2000 keV, was used in analyzing background impact. Fitting of background spectra above signal was not performed. Hit location information was used only to cut multi-site events (track length > 2cm in any dimension), and reject all events within 2 cm of the LXe vessel walls.

Many physics generators are used to simulate all isotopes of concern for EXO-200. The full ^{232}Th and ^{238}U decay chains were simulated, including all alpha, beta, and gamma emissions. Time correlation of emissions was simulated as well. The ^{60}Co generator included angular correlations of gammas. A ^{222}Rn generator was used to simulate radon in air gaps between lead shielding and the cryostat. A ^{210}Pb generator was used to simulate ^{210}Pb contamination of the lead shielding itself, as well as ^{210}Pb plating of detector components due to exposure to ^{222}Rn contaminated air during storage and handling. Other simulated isotopes included ^{51}Cr, ^{54}Mn, ^{56}Co, ^{58}Co, ^{59}Fe, ^{65}Zn, ^{85}Kr, ^{135}Xe, ^{137}Xe, ^{136}Cs, and ^{137}Cs. $0\nu\beta\beta$ and $2\nu\beta\beta$ decays were simulated by selection from correlated electron momentum distributions. Finally, an underground muon generator, including energy and angle distributions, was used to aid construction of the muon veto and assess cosmogenic activation of copper during fabrication and handling.

The physics generators were used to simulate sources of radiation spread evenly through various volumes of the detector. Since ^{40}K, ^{232}Th, and ^{238}U contamination is present in every component of the detector, hit efficiencies in number of $0\nu\beta\beta$ or $2\nu\beta\beta$ background counts per radioactive decay for various volumes throughout the detector are presented here (see tables 3.2 and 3.3). The specific background impact

Volume	^{40}K (2ν)	^{232}Th (2ν)	^{238}U (2ν)
TPC and LXe vessel	6.16×10^{-3}	6.05×10^{-2}	4.53×10^{-2}
Flexible cables	4.15×10^{-3}	4.42×10^{-2}	3.37×10^{-2}
HV cable	1.46×10^{-3}	1.32×10^{-2}	1.06×10^{-2}
Cryostat and vacuum space	4.79×10^{-6}	5.53×10^{-5}	3.47×10^{-5}
Cryostat hardware, lead paint	7.32×10^{-7}	1.23×10^{-5}	7.32×10^{-6}
Lead barrel and inner walls	1.34×10^{-7}	1.76×10^{-6}	1.05×10^{-6}
Outer front lead wall	8.8×10^{-10}	1.8×10^{-8}	7.3×10^{-9}

Table 3.2: Monte Carlo hit efficiencies in $2\nu\beta\beta$ background counts per radioactive decay for ^{40}K, ^{232}Th, and ^{238}U decays in various detector volumes.

Volume	^{232}Th (0ν)	^{238}U (0ν)
TPC (incl. LXe vessel)	2.30×10^{-4}	3.87×10^{-4}
Flexible cables	1.79×10^{-4}	1.13×10^{-4}
HV cable	1.01×10^{-4}	6.36×10^{-5}
Cryostat and Vacuum space	9.37×10^{-7}	1.51×10^{-7}
Cryostat hardware, lead paint	2.82×10^{-7}	3.64×10^{-8}
Lead barrel and inner walls	4.30×10^{-8}	2.21×10^{-9}
Outer front lead wall	3.3×10^{-10}	$<1.6\times10^{-10}$

Table 3.3: Monte Carlo hit efficiencies in $0\nu\beta\beta$ background counts per radioactive decay for ^{232}Th and ^{238}U decays in various detector volumes.

of these contaminants in every major component of the detector is calculated based on these hit efficiencies and measured contamination levels, and is presented throughout chapters 4 and 5.

The hit efficiencies for cosmogenically activated isotopes is presented in the following section. Hit efficiencies for other radioactive isotopes are presented along with specific background impact results in relevant sections of chapters 4 and 5.

3.7 Cosmogenics

The background rate R in counts/year due to a pure sample of mass M exposed to cosmic rays for a time t and placed in the EXO-200 detector is given by

$$R = \sum_i \left(365 \cdot P_i \cdot a \cdot M \cdot (1 - 2^{-t/\tau_i})(2^{-t_c/\tau_i})\epsilon_i\right) \tag{3.3}$$

where t is given in days, P_i is the cosmogenic production rate of isotope i at sea level in $kg^{-1} \cdot day^{-1}$ (given for copper in table 3.4), a is the cosmogenic neutron flux attenuation factor due to a concrete overburden, M is the mass in kg, τ_i is the half life of the isotope i in days, t_c is the cooldown period (cosmic ray neutron flux = zero) in days, and ϵ_i is the hit efficiency for isotope i given in table 3.4. a was simulated using the FLUKA[82] Monte Carlo package for storage of EXO components at Stanford underground facilities, and transport in concrete shielded shipping containers. Results are shown in figure 3.7.

This information will be useful as a reference when backgrounds due to cosmogenic activation of the LXe vessel, TPC components, and cryostat are discussed in sections 4.5 and 5.2.

Decay (channel)	TPC	Cryostat	$T_{1/2}$ [days]	P $[kg^{-1}{\cdot}day^{-1}]$
^{54}Mn (2ν)	3.23×10^{-2}	1.67×10^{-5}	312	32.5
^{56}Co (0ν)	2.28×10^{-4}	2.91×10^{-6}	77.3	22.9
^{56}Co (2ν)	3.34×10^{-2}	1.53×10^{-4}		
^{58}Co (2ν)	3.36×10^{-2}	1.60×10^{-5}	70.8	159.6
^{59}Fe (2ν)	3.08×10^{-2}	4.51×10^{-5}	44.5	6.5
^{60}Co (0ν)	5.70×10^{-5}	$< 1\times10^{-10}$	1925	97.4
^{60}Co (2ν)	3.87×10^{-2}	1.03×10^{-4}		
^{65}Zn (2ν)	1.65×10^{-2}	1.95×10^{-5}	244	<46.8*

Table 3.4: Monte Carlo hit efficiencies in $2\nu\beta\beta$ and $0\nu\beta\beta$ background counts per radioactive decay for ^{54}Mn, ^{56}Co, ^{58}Co, ^{59}Fe, ^{60}Co, ^{65}Zn decays in the TPC and cryostat copper. Only ^{56}Co and ^{60}Co have decay energies high enough to contribute to the $0\nu\beta\beta$ background. The half-life for each isotope and cosmogenic production rate at sea level[17] are also shown. *An upper limit on the production rate measured by the EXO Collaboration at Neuchatel.

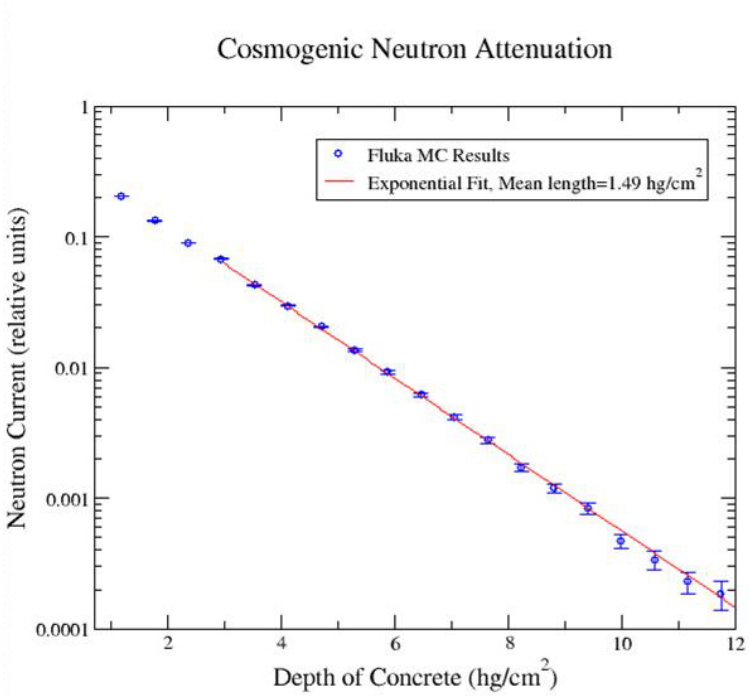

Figure 3.7: Simulated attenuation of cosmic ray neutron current due to a concrete overburden.

Chapter 4

The Liquid Xenon TPC

EXO-200 uses 200kg of LXe enriched to 80% in ^{136}Xe as source and medium for detection of $2\nu\beta\beta$ and $0\nu\beta\beta$. This xenon is contained inside a Time Projection Chamber (TPC). A detailed description of each major component of the LXe TPC is presented in this chapter.

4.1 Ionization Channel

A schematic representing each of the two grids used to collect ionization at either end of the TPC is shown in figure 4.1. Each grid is comprised of two parallel planes of wires. The wires in each plane are oriented 60 degrees from the wires in the other, allowing two-dimensional reconstruction of the ionization cloud location. The angle was chosen to match the natural shape of the detector planes defined by the close hexagonal packing of the round APDs.

The plane farthest from the cathode (referred to as anode, or the collection wires) is held at virtual ground potential by the readout electronics and is responsible for collection of ionization, which is read as a pulse with integrated charge proportional to the total charge collected. The plane between the cathode and anode (referred to as the induction wires) is held at negative potential, and reads an induction signal as ionization passes by them on their way to the collection wires, thus allowing two

dimensional reconstruction of the event topology. The induction wires are also responsible for shielding the anode from the drifting of positive xenon ions created in the ionization event. For the 3mm pitch used in EXO-200, 100% electron transparency of the induction wires is achieved when the electric field between the induction wires and anode is at least 160% that between the induction wires and cathode[83].

The anode and induction planes are comprised of 38 read out channels each. A channel spacing of 9 mm was chosen. This spacing provides a two dimensional spatial resolution of <1 cm, optimal for topological discrimination between background and signal (see section 2.8).

A wire pitch smaller than the channel spacing of 9 mm is required to (1) maintain a uniform electric field both near the shield wires and between the shield wires and anode and (2) increase shielding efficiency for events near the induction plane. On the other hand, closely spaced wires have a higher capacitance (resulting in higher electrical noise) and higher channel count. A wire pitch of 3 mm was chosen, with triplets of wires, connected together, constituting single channels. Finally, the perpendicular distance between the APD, anode, and induction wire planes is 6 mm, providing field uniformity in the volume between the anode and induction wires while allowing relatively low induction wire voltage as required to maintain electron transparency. This geometry results in >99% shielding efficiency and electric field uniformity 3 cm into the drift volume, an acceptably uniform field between induction wires and anode, and an anode channel capacitance to the APD plane of 0.51 pF/cm.

As with every detector component, minimization of radioactive contamination was an essential consideration in the design of the ionization wires. The unique design requirement in this case is sustaining tension and integrity of the wires through thermal cycling of the detector. Most systems of springs and connectors suited for this purpose involved many small parts fabricated from materials incompatible with our radiopurity requirements. A novel solution was found in photo etching, a commercial process in which a system of acids and photo-sensitive masks are used to dissolve intricate patterns into a metallic sheet. Vaga Industries[84] was contracted to photo etch wire triplets in 5-mil full hardness CA-510 Grade A phosphor-bronze sheet, purchased from E. Jordan Brookes Co [85] (see figure 4.2a). Springs were created

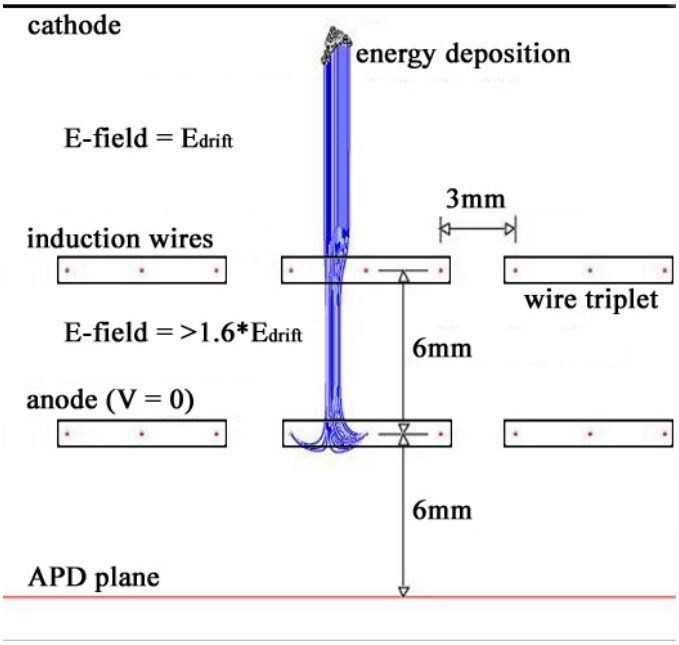

Figure 4.1: Simulation of the drift and collection of an electron cloud. The anode and induction wires are shown co-linear, though as constructed they are oriented at 60 degrees.

by bending extended tabs on both ends of the triplet into a rounded triangle. The springs behave linearly below 900g with spring constant 2950±75 g/cm, and begin to yield at 1000g. Individual wires in each triplet have a roughly hexagonal cross section measuring 127±40 μm wide. The unusual shape of the wires has no effect on their ability to capture electrons, because they are operating in LXe with unity gain. The optical transparency of each plane is 95.8%.

Custom 0-80 screws on either end of the triplet serve both as anchors for the springs and electrical connection to the wires (see figure 4.2b). 19 such anchoring screws are bolted to each of six (6±0.02) mm thick acrylic blocks mounted in a hexagonal pattern onto a copper support ring, as shown in figure 4.3. The screws bolted to four of the acrylic blocks are platinum plated and pass through flexible cables making an electrical connection. Anode wire-anchoring screws are mounted on one side of two of these blocks, whereas induction wire-anchoring screws are mounted on the opposite side of the other two, forming the 6 mm gap described above. The remaining pair of blocks have unplated anchoring screws on both sides, and anchor the ends of both anode and induction wires without making electrical connections. The 19 wire-triplet lengths vary linearly from 22.78 cm to 41.47 cm (anchoring screw to anchoring screw) along each acrylic block. As installed at room temperature, the springs in each wire generate a tension of 300-600 grams, sufficient to ensure wire displacements of <100 μm due to electrostatic forces between the APD, anode, and induction planes at full voltage. Due to the large coefficient of thermal expansion (CTE) of acrylic relative to copper and phosphor-bronze (see table 4.1) and the mounting geometry of the acrylic blocks on the copper support ring, the shortest 26 wire-triplets in each wire plane experience an increase in tension during cooldown, while the remaining 12 experience a decrease. The shortest channels effectively stretch by 0.28%, and the longest effectively compress by 0.05%, resulting in a change in tension during cooldown ranging from approximately +185g to -60g.

The low activity acrylic used in the EXO-200 TPC was graciously supplied by the Sudbury Neutrino Observatory collaboration. All acrylic machining was performed dry using air cooling and new carbide tools. Background contamination of the raw material was measured by NAA to be <0.4 pg/g ^{40}K, <4 pg/g ^{232}Th, and <4 pg/g ^{238}U

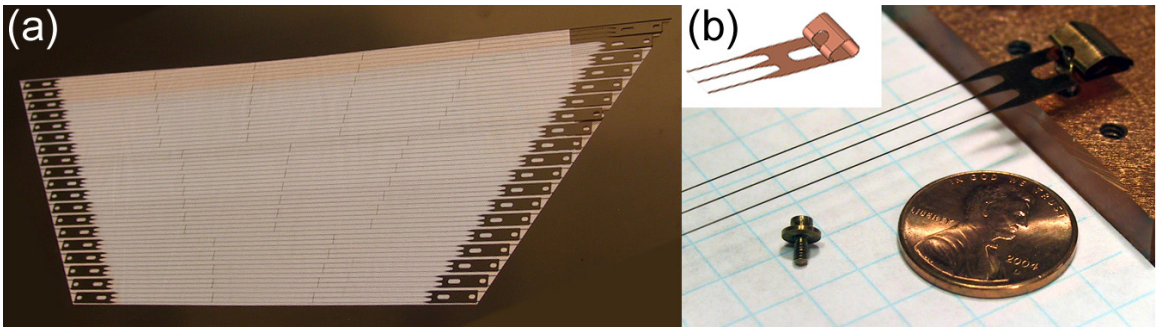

Figure 4.2: (a) Ionization wires photo etched on a phosphor-bronze sheet, as received from Vaga Industries. (b) An ionization wire spring mounted on a custom designed 0-80 screw.

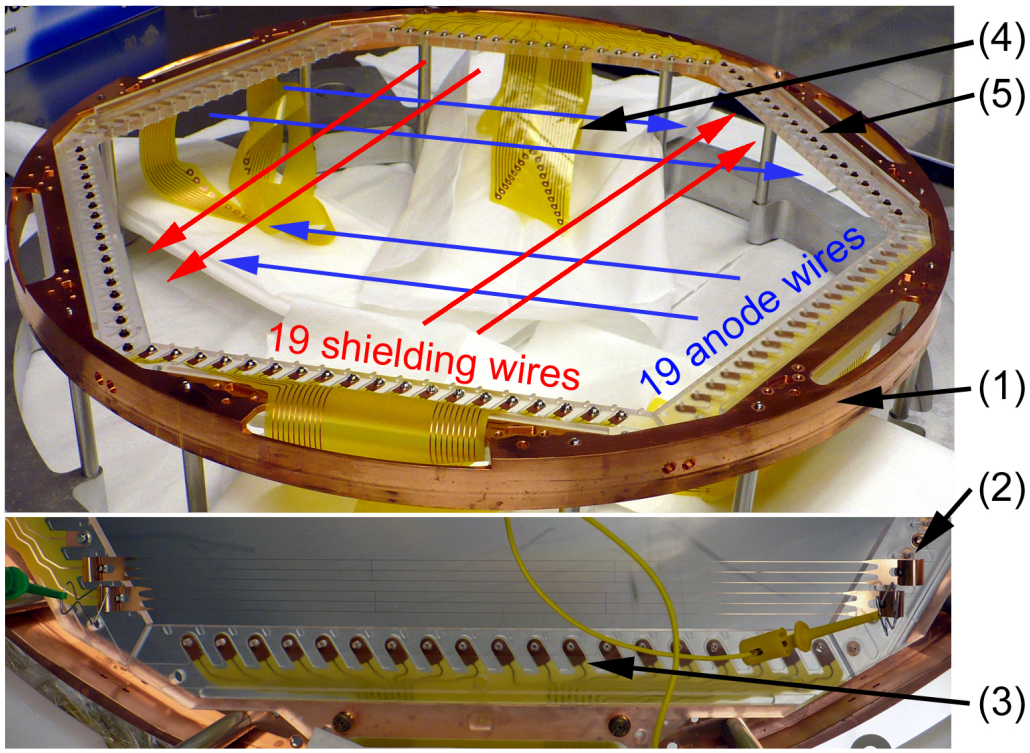

Figure 4.3: A copper support ring (1) holds six acrylic blocks in a hexagonal pattern. Anode wires (2) are mounted on one side of the acrylic blocks and induction wires (not shown) are mounted on the opposite side (3) providing a spacing of (6±0.02) mm between the wire planes. Four flexible cables (4) each make electrical connection to platinum plated 0-80 screws which anchor 19 wire triplets to each of four of the acrylic blocks. Unplated 0-80 screws on both sides of the remaining two acrylic blocks (5) serve only to anchor the other end of the wires and do not make electrical connection.

Material	CTE [μm/m/K]
Copper	16.9
Ca510 Phosphor-Bronze	17.8
Acrylic	73.6

Table 4.1: Coefficients of thermal expansion of materials relevant to ionization wire construction

(the SNO collaboration made more sensitive measurements prior to our receipt of the acrylic, finding <1 pg/g of both ^{232}Th and ^{238}U[86]). Following sections will describe further use of SNO acrylic throughout the TPC. In total, 1438g is used in the TPC, with an estimated background contribution of <174 $2\nu\beta\beta$ and <1 $0\nu\beta\beta$ event/year, corresponding to $< 0.4\%$ and $< 3.5\%$ of total background tolerance respectively.

Many of the phosphor-bronze components in the TPC were platinum plated to improve electrical contact. All platinum plating was performed in house by the SLAC plating shop. Prior to plating, all parts were treated in a 19% HCl solution, followed by 30 seconds in a "bright dip" solution (75% phosphoric acid, 8% nitric acid, 17% water). 1 Å of nickel was plated onto each part using an HCl / Nickel Chloride solution, to prevent the phosphor-bronze from diffusing into the platinum solution. Following this, Platinum S from Technic[87] was used to plate 300 nm of platinum on each part. ICPMS of platinum plated phosphor-bronze showed negligible increase in radioactive contamination due to plating.

Radioactive contamination of the ionization wires at various stages of fabrication and cleaning is listed in table 4.2. Before producing EXO-200 parts, the production process at Vaga Industries was observed and radioactive impurities in the chemicals used were measured. To improve radiopurity in EXO-200 parts, the etching bath was cleaned, and fresh etchant (ferric chloride) was used. In addition, potassium carbonate was eliminated from the production process and replaced with sodium carbonate. Despite these precautions, parts received from Vaga Industries and cleaned using the standard cleaning procedure (see section 3.5) saw increases in ^{232}Th and ^{238}U contamination of 635% and 32,000%. An aggressive cleaning procedure was developed, involving a prolonged soak in 3M HNO_3 at 60 °C, which removed over

Material	^{40}K [pg/g]	^{232}Th [pg/g]	^{238}U [pg/g]
Raw material	<9.4	7.4±1.7	<1
Uncleaned	<10.5	56±1	358±5
Standard cleaning	<10.5	47±2	320±2
Aggressive cleaning	<10.5	26.6±4.6	29.5±1.7

Table 4.2: Radioactive contamination of ionization wires with various cleaning treatments and of the raw material. Contamination levels given in pg/g, measured via ICPMS.

90% of the added ^{238}U contamination, although a 40% loss of mass was also observed.

The total mass of the ionization wires installed is 82.08g. Based on the Geant3 Monte Carlo and empirical contamination data after aggressive cleaning, the ionization wires are predicted to contribute 0.37-0.48 $0\nu\beta\beta$ background events per year due to ^{232}Th and ^{238}U contamination and 55-110 $2\nu\beta\beta$ background events per year due to ^{40}K contamination. This corresponds to 0.1-0.3% and 1.3-1.6% of background tolerance for $2\nu\beta\beta$ and $0\nu\beta\beta$ respectively.

4.2 Scintillation Channel

As discussed in chapter 2, many electrons liberated by ionizing radiation passing through LXe promptly recombine with xenon ions, producing 178 nm scintillation light. Statistical fluctuations in this recombination process results in relatively poor energy resolution if only the ionization channel is observed. Measurement of both the ionization and scintillation channels is crucial for optimizing energy resolution in LXe.

Photomultiplier Tubes (PMTs) are the popular choice for measuring scintillation light in current experiments. However, these devices are large and complex. They are generally built from materials incompatible with EXO-200 background requirements, in particular glass, ceramic, and metal alloys. Avalanche Photodiodes (APDs), an alternative to PMTs, are compact semi-conductor devices made mostly of silicon. They are fabricated in a very clean environment from pure raw materials, and in their 'bare' form (i.e. without standard ceramic encapsulation) they are very light

weight, with masses typically <1 g. Thus, they are well suited for the particularly low background requirements of EXO-200. They carry the disadvantage of a much lower gain (∼100 vs ∼1×10^6 for PMTs), but this is partially compensated for by much higher quantum efficiency (∼120% at 178 nm). In addition, when compared with a dark matter or solar neutrino detector for example, the signal expected in EXO-200 is large and sensitivity to single photons is not required. Finally, the electronic noise of the APDs is lowered when operating at LXe temperature rather than room temperature.

EXO-200 uses unencapsulated Large Area APDs[88] produced by Advanced Photonix, shown in figure 4.4a. APDs produced by Hamamatsu[89] and RMD[90] were investigated and rejected, due to the unavailability of bare devices and relatively low quantum efficiency (∼30%) at 178 nm respectively. In addition, APDs are much larger than competitors', allowing few channels in the detector. Each APD has a 16 mm diameter active area (200 mm^2), with an overall diameter between 19.6 mm and 21.1 mm. The thickness of each varies between 1.32 mm and 1.35 mm, with total mass of 528 mg. A schematic of an APD is shown in figure 4.4b. The devices consist of a p-type epitaxial layer grown on n-type neutron transmutation doped silicon. A cathode is created by plating 40 nm of Ti, 80 nm of Pt, and finally 400 nm of Au on one side of the wafer. A second silicon wafer, sand cut into a ring-shape and similarly gold plated, is bonded by a layer of Al (and with trace amounts of P and B) to the opposite side, forming an anode. The edge of the device is then beveled and coated with a polyimide film to improve breakdown and dark current characteristics. The capacitance of APDs under operating conditions (1400 V bias and LXe temperature) was found to be 125 pF.

Incoming scintillation photons are absorbed in an undepleted region in the first 5-8μm of the diode. Resultant electrons enter the drift region, where they are accelerated to energies sufficient to induce ionization. The avalanche is collected by the cathode, resulting in a current pulse with integrated charge proportional to the total energy of the incoming photons. Optimal energy resolution occurs at a gain of ∼100[22, 91].

Assembly of APDs at Advanced Photonix takes place in a class 1000 cleanroom

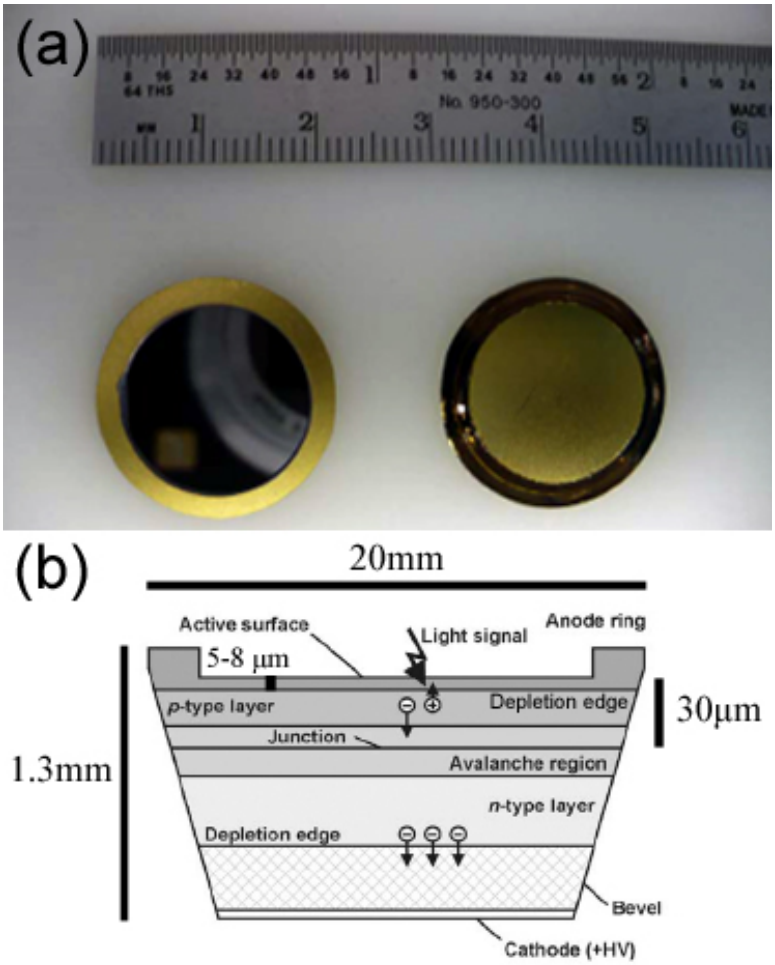

Figure 4.4: (a) An APD's active surface and gold plated anode (left) and gold plated cathode with polyimide coated beveled edge (right). (b) Cross section of a Large Area Avalanche Photo Diode. Image adapted from [22].

environment. Strong acids and solvents are used at several points during fabrication to minimize contamination that would otherwise degrade the performance of the devices. Very few contaminants are introduced into APDs during the fabrication process, and surface contamination of final parts is negligible. Once produced, each EXO-200 APD was placed inside a static dissipative plastic case in the class 1000 cleanroom environment. The cases were then packed into a stainless steel vacuum vessel purged with boil-off N_2 and transported from Advanced Photonix to Stanford University by car. They were unpacked inside a class 1000 cleanroom environment and stored in a boil-off N_2 purged drybox until installation. Bare APDs before and after transportation were handled using only a vacuum pen applied to the cathode. All EXO-200 APDs were tested and installed in the condition they were received. No additional cleaning was applied in order not to damage the very sensitive bare devices.

The gain, relative QE, and noise characteristics of all purchased APDs were measured at LXe temperature (170K)[91]. Gain measurements were obtained by observing the response of each APD to 5.9 keV x-rays from an ^{55}Fe source. These X-rays ionize the silicon in the same way scintillation photons do, except that over $\sim$1650 electron-hole pairs are produced for each X-ray photon, making detection of single photons possible at this energy. Detection of single photons is needed to deconvolve the gain measurement from the QE measurement. Relative QE measurements were made using a xenon scintillation light source by comparing the response of all APDs to that of an arbitrarily chosen APD at fixed gain. Electronic noise was taken as the RMS of the output of each APD with no signal. Noise contribution from electronics was not subtracted. The absolute QE of APDs is roughly 120% at 178 nm, based on measurements provided by API.

851 APDs were purchased. 184 of the initial sample were rejected due to instability or excessive noise when biased at 170K (Advanced Photonix qualifies and gurantees their APDs at room temperature only). Figure 4.5a shows a histogram of the relative QE of the remaining 667 APDs. A cutoff of QE = 0.8 was chosen semi-arbitrarily to eliminate the non-gaussian tail, cutting 30 devices. The 468 APDs exhibiting the lowest noise were then chosen from the remaining subset for installation, with the cut

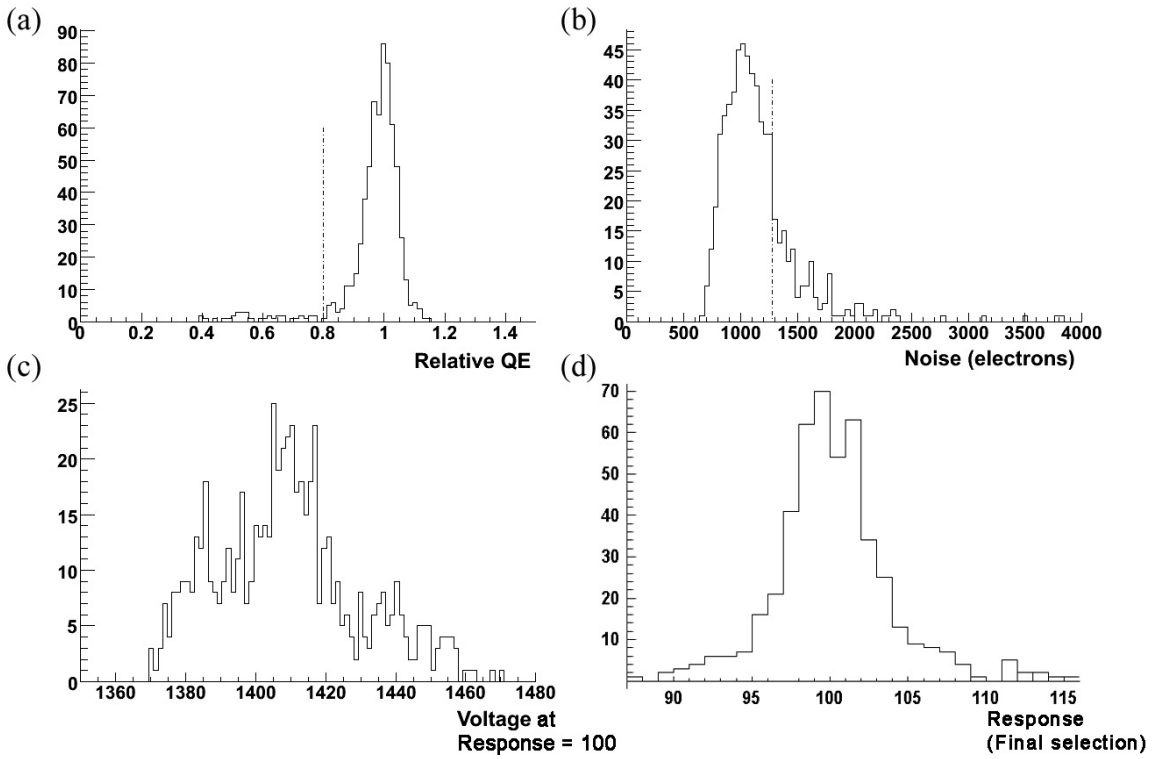

Figure 4.5: (a) Relative quantum efficiency (QE) of the 667 measurable EXO-200 APDs, with cut at 0.8 shown. (b) Electronic noise of the 637 APDs with QE > 0.8, with cut at 1280 electrons shown. (c) Voltage required for response (gain $\times$ rel. QE) $= 100$ for final selection of 468 APDs. (d) Response of final selection of APDs at operating voltage. All measurements taken at 170K.

Material	^{40}K [pg/g]	^{232}Th [pg/g]	^{238}U [pg/g]	Mass [g]
Si (epi*)	<0.92	<4.9	<4.9	303
Si (ring)	<0.14	114±12	13.3±2.4	218
Al	<7956	48200±4800	5510±580	3.25
Norsk Al	<11.7	45±2	440±2	
Au	N/A	612±18	79±2	3.13
Pt	N/A	32±2	241±4	0.73
Ti	<23.4	<0.1	<0.1	0.076

Table 4.3: Radioactive contamination of the stock raw materials at API which compose an APD in pg/g, and the quantity of material in each APD. The metals were measured by ICPMS. The Si was measured using NAA. *Epitaxial wafer

placed at 1280 electrons (see figure 4.5b).

APDs exhibit a large spread in the voltage required to achieve a fixed response. The voltage required to achieve a response (defined as gain × rel. QE) of 100 was used to characterize this spread in the final selection of APDs (see figure 4.5c). The spread was compensated for by separating the APDs into 12 voltage groups, each with a unique trim voltage, thus reducing the overall variation in operating APD response to 2.5% (σ) (see figure 4.5d).

Direct NAA of APDs is not possible due to the presence of Au which is activated by neutrons. (Extensive effort was put into developing APDs with Al contacts in place of Au, but such APDs were susceptible to build-up of static charge and were thus non-functional). Measurement of the radioactive contamination in APDs required a two-step process. The APDs were placed in aqua regia (a solution of concentrated nitric acid and hydrochloric acid with a molar ratio of 1:3) at 120°C for seven days. The metals and some polyimide were thus dissolved, leaving behind the silicon wafers. The metal solution was evaporated, reconstituted with nitric acid, and ICPMS was performed. NAA was used to measure contamination in the silicon wafers and remaining polyimide. Despite the extremely clean production process, contamination levels in APDs were found to be ∼300% higher than tolerable. Table 4.3 lists the intrinsic radioactive contamination of raw materials entering the fabrication of an APD, and the quantity of material in each device. Most of the contamination was traced to the

Component	^{40}K [pg/APD]	^{232}Th [pg/APD]	^{238}U [pg/APD]
Si (epi*)	<0.28	<1.5	<1.5
Si (ring)	<0.03	25±3	2.9±0.5
Other metals (best case)	<0.36	<2.1	<4.4
Other metals (worst case)	<0.62	7.8±1.4	8.9±1.6
Total worst case limit	<0.93	28.4-38.7	9.7-15.4

Table 4.4: Worst case radioactive contamination in production APDs in pg/APD. *Epitaxial wafer

aluminum being used, thus a much purer aluminum from Norsk Hydro ASA[92] was used in production of EXO-200 APDs. In addition, fresh ceramic crucibles were used to hold this aluminum, and the aluminum evaporator was run empty for one cycle upon transitioning from normal production to production of EXO-200 APDs using this pure aluminum.

The 851 APDs were delivered from Advanced Photonix to Stanford University in twelve batches over a period of two years. Several complete but rejected devices were included in each batch for radioactive contamination testing. Contamination levels were generally stable with time, varying within a factor of two. Table 4.4 shows contamination levels in the metals and silicon wafers of the best and worst batches measured. The combined total background contribution assuming all APDs are as contaminated as the worst batch is 184-291 and 1.1-1.6 $2\nu\beta\beta$ and $0\nu\beta\beta$ events/year, corresponding to 0.5-0.7% and 3.6-5.4% of total background tolerance respectively.

Two copper platters located 6 mm behind each anode wire plane hold 234 APDs each with a photosensitive packing ratio of 48% (See figure 4.6). The anodes of all 234 APDs are electrically connected together and held at -1.4kV. The contact surface of each APD platter is gold coated (details given below) to provide a stable and reliable contact. The APD planes were fabricated to accomodate 259 APDs, though after fabrication it was decided not to install several APDs because their field of view is either blocked or is outside the active volume. Each of the two APD planes is divided into six sectors, four containing 38 APDs each, with the remaining two containing 37 and 45 APDs, as shown in figure 4.7. Each of these twelve sectors corresponds to one of the twelve voltage groups mentioned in the previous paragraph.

Figure 4.6: Bare APDs are placed in a sector (1) on a gold plated APD platter (2). Platinum plated photo etched phosphor bronze springs (3) anchor gangs of 7 APDs (4) to the copper platter, and provide electrical contact between the cathodes of each APD and copper traces (5) on flexible cables (6). Acrylic washers (7) prevent electrical contact between mounting screws and the spring. Ionization wires can be seen through the partially filled APD platter (8).

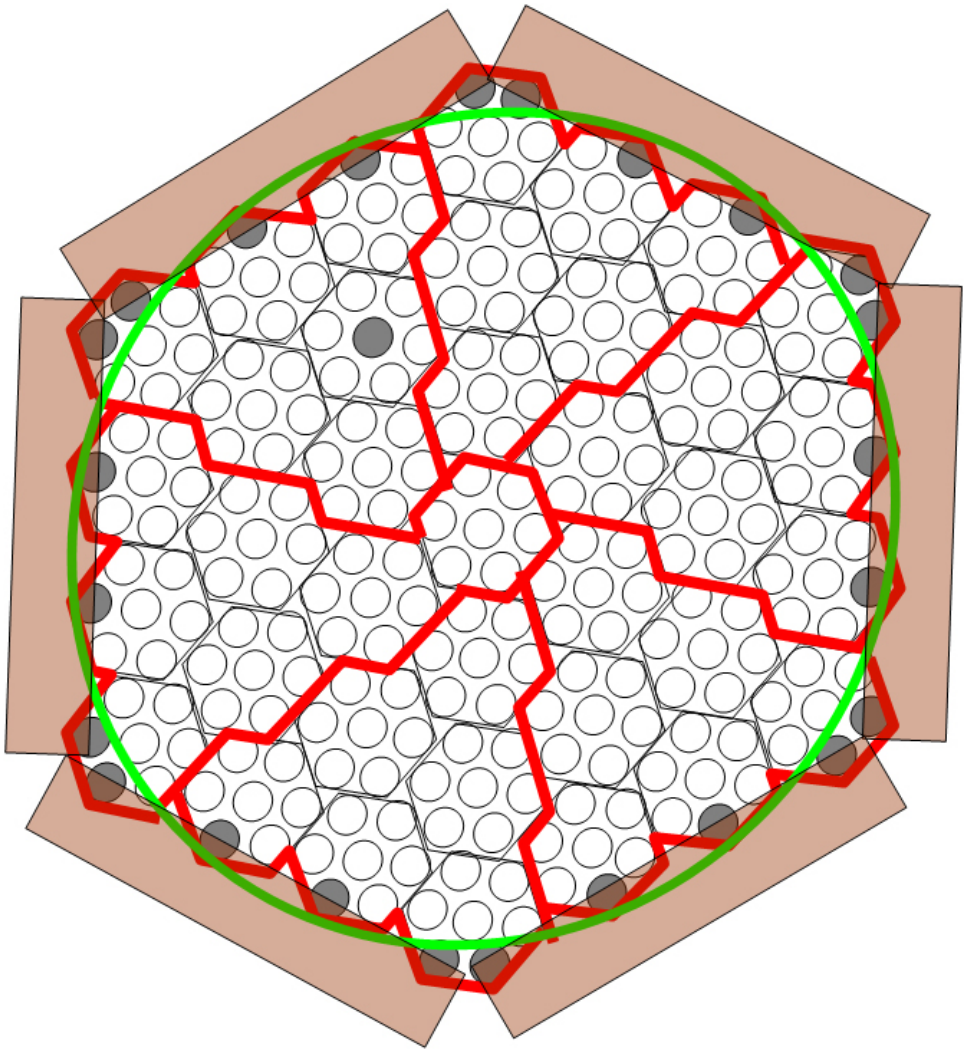

Figure 4.7: A figure representing the division of the APD platters into sectors. Gray circles indicate positions in which an APD is absent, either because its window is located outside of the active volume (indicated by a green circle) or because it is shadowed by ionization wires (indicated by brown rectangles). The LED diffuser is located at the gray circle closer to the center of the platter, in the upper left sector.

Material	^{40}K [pg/g]	^{232}Th [pg/g]	^{238}U [pg/g]
Nickel	N/A	14.7±3.5	<15.2
Gold	N/A	40.7±4.1	<13.4
MgF_2	<62.6	793±296	< 2170±144
Norsk Al	<11.7	45±2	440±2

Table 4.5: Radioactive contamination of the raw materials used to plate each APD platter in pg/g. Nickel, Gold and Aluminum were measured using ICPMS. MgF_2 was measured using direct counting.

The two sectors containing 37 APDs each contain an LED diffuser, the location of which is also indicated in figure 4.7. The diffuser consists of a Teflon disk, 20 mm in diameter and 1.35 mm in height, located in place of an APD. A fiber optic cable delivers light (either 178 nm or visible) to the diffuser, which can then be used to test basic functionality of the APDs during detector commissioning.

APD channels are created by grouping APDs into 'gangs of 7' (see inset in fig. 4.6), for a total of 74 gangs. Each gang is held in place by a 250 μm thick photo etched phosphor bronze spring, produced and cleaned in the same manner as the ionization wires described in section 4.1. These springs also serve to electrically connect the cathodes of all 7 APDs in the gang to a trace on a custom flexible cable. The springs are platinum plated to provide a stable and reliable contact, and custom acrylic washers prevent electrical contact between phosphor bronze mounting screws and the spring. Radioactive contamination of the springs was measured by ICPMs to be <8.2 pg/g ^{40}K, 13.8±2.1 pg/g ^{232}Th, and 27.5±1.6 pg/g ^{238}U. The total mass of the 74 springs is 129.5 g. These contribute 71-138 $2\nu\beta\beta$ and 0.5-0.6 $0\nu\beta\beta$ evt/yr, corresponding to 0.2-0.3% and 1.8-2.1% of tolerance.

Each APD sector is paired with one flexible cable, which carries the signals from all the cathodes of all the gangs in that sector to the electronics. The flexible cable also supplies all of the cathodes in each sector with a common trim voltage. Cathode trim voltages are provided by EMCO[93] CA Series 200V power supplies.

The coating of the APD platters was performed by vacuum evaporation by VPE Inc[94]. 300 Å of nickel followed by 1000 Å of gold are evaporated on the APD-bearing side of the platters. The opposite side of each platter, facing the fiducial volume of

the detector, is coated with 1000 Å of aluminum followed by 500 Å of magnesium fluoride. Prior to coating, both platters were cleaned as described in section 3.5, except that each platter was rinsed with HCl and HNO_3 separately, and the acid rinsing was performed twice. New crucibles were used to hold the raw metals during the evaporation process. Gold, nickel, and magnesium fluoride were purchased from Cerac Inc[95]. Aluminum was the same as that used in APD production. Intrinsic contamination of these raw materials is listed in table 4.5. A background analysis of 1 in^2 phosphor-bronze coupons, plated exactly as the APD platters were, showed a change of ^{232}Th (^{238}U) contamination from 3.1 (<4.6) pg/g to 9.0 (11.1) pg/g. Given the 1562g mass of each APD platter, coating of the platters is predicted to contribute 504-759 $2\nu\beta\beta$ and 3.6-5.8 $0\nu\beta\beta$, corresponding to 1.3-1.9% and 12.1-19.4% of tolerance.

The purpose of coating the APD platters with aluminum was to improve the reflective properties of the surfaces for VUV radiation. Further improvement of collection efficiency was obtained by lining the barrel of the fiducial volume with 1.5 mm tiles specially sintered using a clean process by Applied Plastics Technologies[96] using DuPont Teflon TE-6472[97] (see figure 4.8). NAA of the Teflon sheet showed 0.235±0.005 pg/g ^{40}K, <0.63 pg/g ^{232}Th, and <1.2 pg/g ^{238}U contamination. With a total Teflon reflector mass of 1675g, the background impact is predicted to be 20-65 $2\nu\beta\beta$ and <0.3 $0\nu\beta\beta$ evt/yr, corresponding to 0.1-0.2% and <1.1% of tolerance. The inner radius of the Teflon reflector lining is 18.3 cm.

Total reflectance of OFHC copper, Teflon, the APD active surface, and MgF_2 coated aluminum for 178 nm radiation was measured at room temperature in N_2 at SLAC using a xenon scintillation light source. Values of 5%, 62%, 52%, and 75% were obtained. Studies by Silva et al have found the total 178 nm vacuum reflectance to be 70%[23] for Teflon, and 5% - 10%[98] for copper, depending on the oxidation level, in agreement with measurements made at SLAC. In addition, they predict a total reflectance of 75% for Teflon in LXe based on the vacuum data. Due to the prevalence of Teflon in the TPC, their Teflon data has been reproduced here in figure 4.9. A detailed GEANT4 simulation based on the data obtained at SLAC and the detector geometry predicts an overall light collection efficiency of 9% for events at the

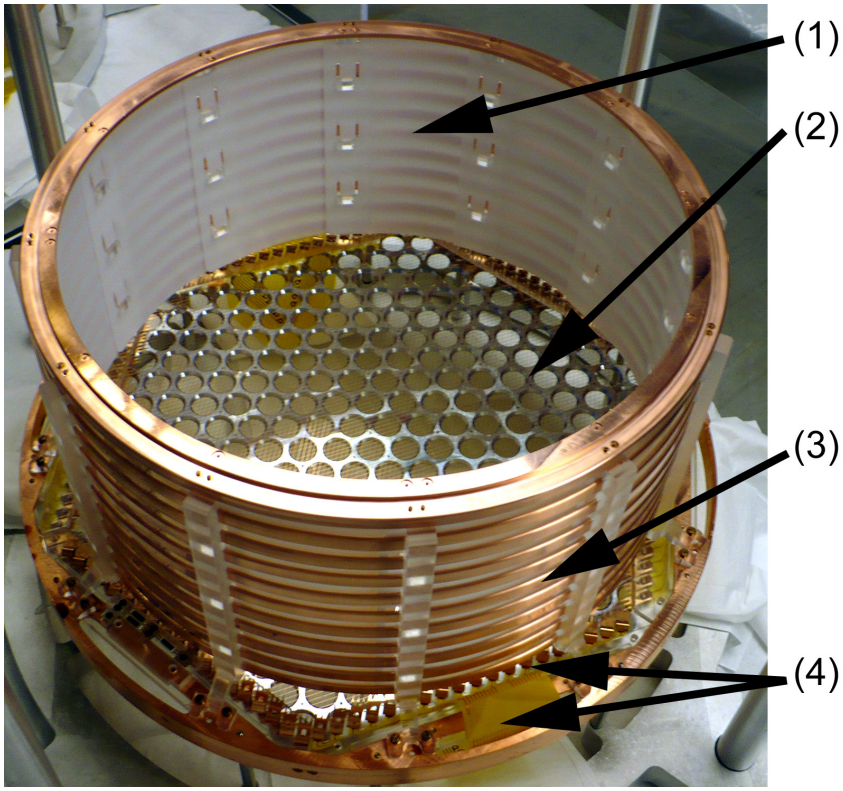

Figure 4.8: A view into the fiducial volume of one of the two EXO-200 TPC modules. Teflon tiles (1) serve as VUV reflectors. The aluminum plated APD platter (2) is visible, as well as the field cage (3), ionization wires, and flexible cables (4).

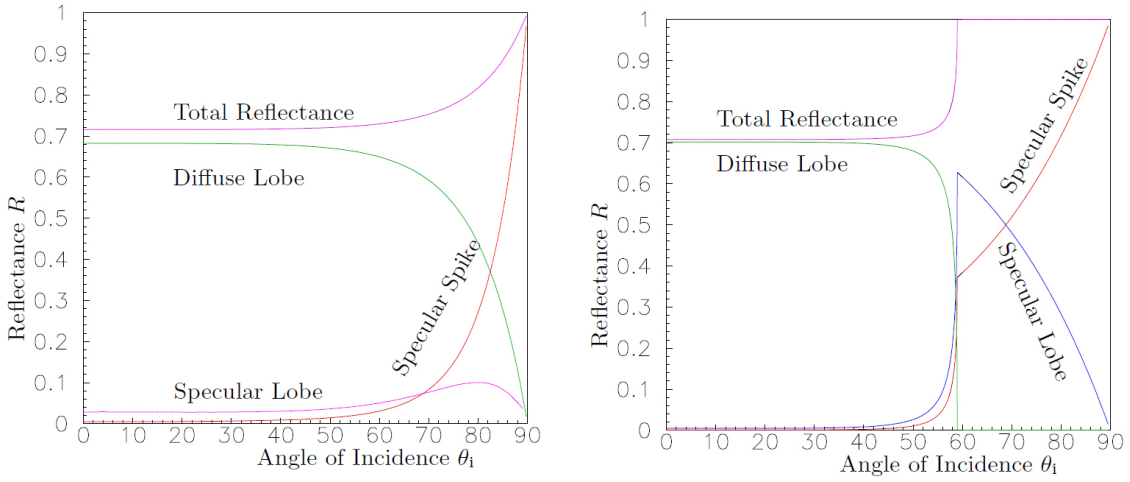

Figure 4.9: Measured reflectance of 178 nm radiation from Teflon in vacuum (left), and predicted reflectance in LXe (right). Images reproduced from [23].

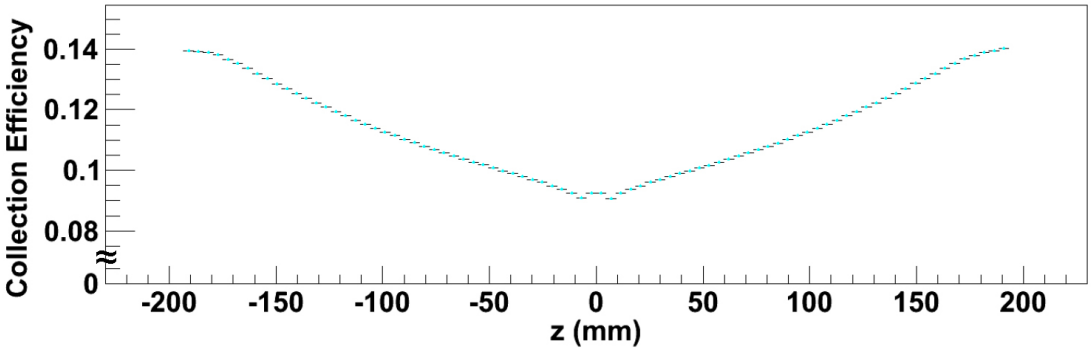

Figure 4.10: Simulated light collection efficiency as a function of z (distance from the center of the detector along its axis).

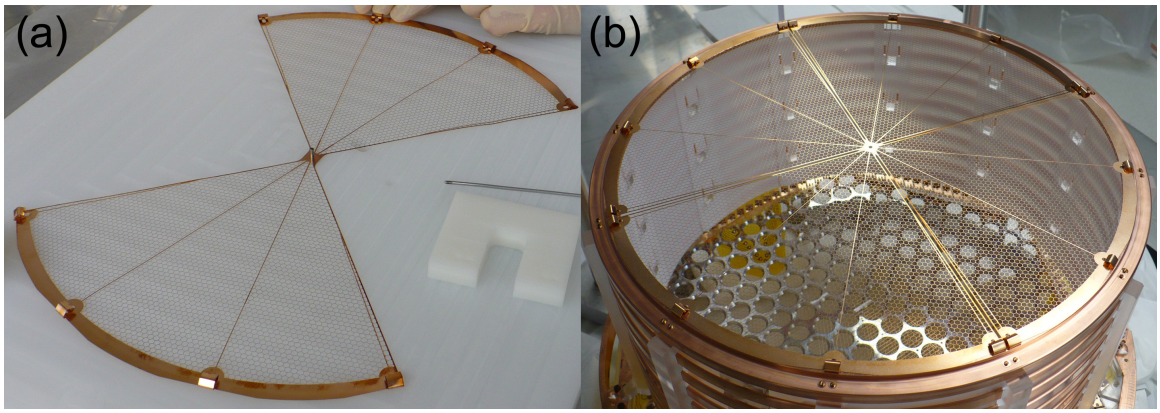

Figure 4.11: (a) One of the two phosphor-bronze photo etched parts comprising the cathode. (b) A complete installed cathode.

center of the detector, rising roughly linearly to 14% for events near either anode, as shown in figure 4.10.

4.3 Drift Field

Energy and spatial resolutions of the EXO-200 detector are strongly dependent on electric field strength and uniformity within the fiducial volume. Energy resolution in LXe improves with increasing electric field (see figure 2.3), though gains become small at fields >2kV/cm if a combined scintillation-ionization analysis is used[20, 52]. In addition, field uniformity is important in optimizing collection efficiency and spatial resolution. Thus, EXO-200 is constructed to operate with a maximum drift field of 3.7 kV/cm with better than 99% field uniformity throughout the fiducial volume.

The drift region of the detector is located between the two induction wire planes on either end of the TPC. It is divided into two identical halves by a phosphor-bronze[85] cathode (see figure 3.1). The cathode is constructed from two parts as a 127 μm thick wire mesh with 90% optical transparency (see figure 4.11a). The parts were photo etched at Vaga Industries in the same manner as the ionization wires, and utilize the same spring mechanism to maintain tension during thermal cycling (see section 4.1). The total mass of the cathode is 20.0g and contamination levels are similar to those previously quoted for ionization wires.

The cathode is mounted on one of the two TPC modules via a copper ring. Twelve custom anchoring screws of size 0-80, identical to those used to install ionization wires, anchor the cathode to the copper ring. Four of these screws placed at opposite corners of each cathode half are platinum plated to improve electrical contact. A similar copper ring also exists on the other TPC module for structural reasons, but is not loaded with a cathode grid.

High voltage is delivered to the cathode via an RG217 coaxial cable purchased from Pasternack Enterprises[99]. The 0.375 inch diameter cable is composed of a 0.108 inch diameter solid copper conductor surrounded by polyethylene insulator (the screen and outer jacket of the cable are removed). The total mass density of the modified cable is 1.11 g/cm. 59.5 cm of cable lies within the inner cryostat. Contamination of the cable was measured by direct counting to be 109 $\pm$ 52 pg/g ^{40}K, $<$ 96 pg/g ^{232}Th, and 337 $\pm$ 115 pg/g ^{238}U. Monte Carlo predicts a background contribution of 113-270 $2\nu\beta\beta$ and 0.4-0.8 $0\nu\beta\beta$ evt/yr (0.3% - 0.7% and 1.2% - 2.8% of tolerance respectively) for this component.

The high voltage cable is inserted into a 5/8 inch copper tube welded between the hatch of the inner vessel of the cryostat and a feedthrough on the chamber. The tube guides the cable to a platinum plated phosphor-bronze[85] spring embedded in a platinum plated copper receptacle. The receptacle is surrounded by DuPont Teflon TE-6472 specially sintered by Applied Plastics Technologies[96] and mounted within the high voltage feedthrough of the chamber (see figure 4.12). A tab on the high voltage receptacle penetrates the Teflon shielding and makes contact with a platinum plated photo etched phosphor-bronze leaf spring screwed onto the copper cathode ring of each of the TPC halves (see figure 4.13). A third platinum plated leaf spring located across from the high voltage connection makes a direct contact between the two copper cathode rings.

The drift region measures 19.2 cm from cathode to induction wires. A 75 kV Glassman[100] power supply generates the $\leq$ 3.7 kV/cm drift field. A 4 kV EMCO[93] C series power supply boosts the potential of the induction wires to 4 kV, resulting in a field strength of 6.7 kV/cm between the induction and collection wires. The residual 10 volt ripple at 55 kHz in the Glassman supply is filtered by a three stage

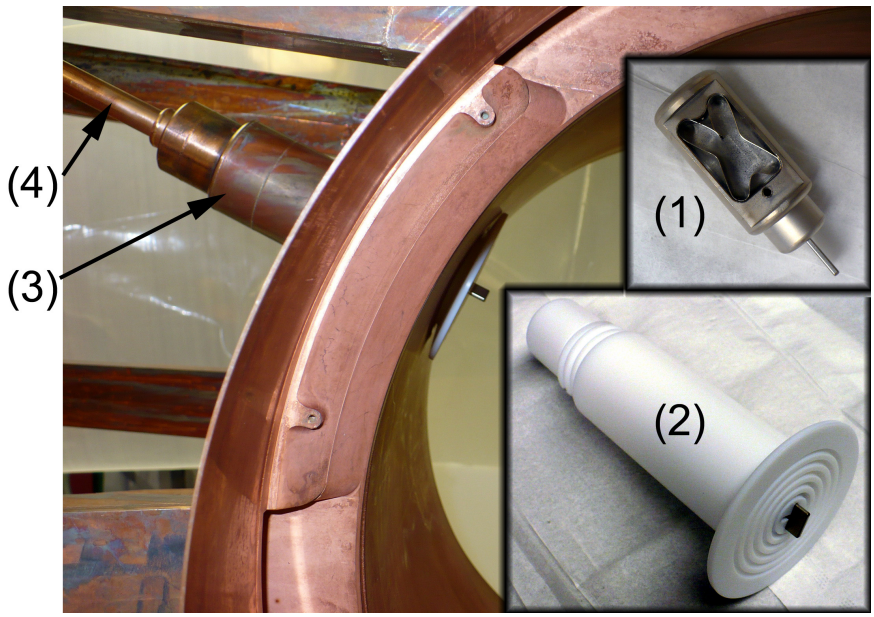

Figure 4.12: The high voltage delivery system: a platinum plated phosphor-bronze spring embedded in a custom machined platinum plated copper receptacle (1). The receptacle is surrounded by Teflon (2) and mounted within the high voltage feethrough (3) of the chamber. A copper tube (4) guides the high voltage cable from the inner cryostat hatch to the chamber.

Figure 4.13: A platinum plated leaf spring screwed onto the copper high voltage ring makes contact with the platinum plated tab on the high voltage cable receptacle.

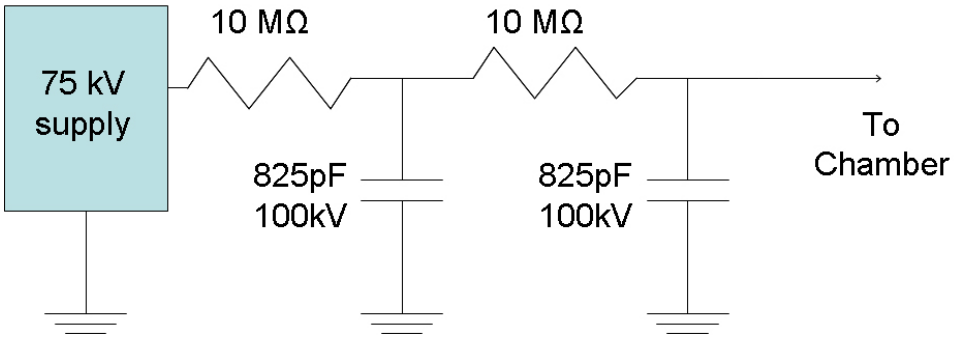

Figure 4.14: The HV filter.

Component	^{40}K [pg/g]	^{232}Th [pg/g]	^{238}U [pg/g]	Mass [mg]
Conductor Paste	5066±667	<7500	5240±770	3
Resistor Paste	632±152	<4200	11500±1800	3
Sapphire	<0.8	30±7	<25	164
Total per Resistor	34.3±4.1	<75	105±12	169

Table 4.6: Breakdown of radioactive contamination of a field cage resistor in pg/g. Mass of each component given in mg.

RC filter, using a 10 MΩ, 825 pF design (see figure 4.14).

The electric field established between the cathode and either induction grid is graded in ten steps, established by ten coaxial copper field shaping rings in each detector half. Each ring is 0.98 cm long, and 37.4 cm OD. The ring pitch is 1.69 cm. Two dimensional MAXWELL[101] simulations of this geometry assuming exact cylindrical symmetry predict that essentially all electrons are collected by the ionization wire planes in a cylinder of radius 0.8 cm smaller than the field shaping rings.

Ten identical resistors grade the potential in each of the field shaping rings (see figure 4.15). An additional three resistors make contact with the induction and collection wire planes. The resistors and field shaping rings are supported by acrylic blocks mounted to the copper support ring to which the wire and APD planes are anchored. Contact with each field shaping ring and between resistors is made by platinum plated phosphor-bronze springs, photo etched in the same manner as the

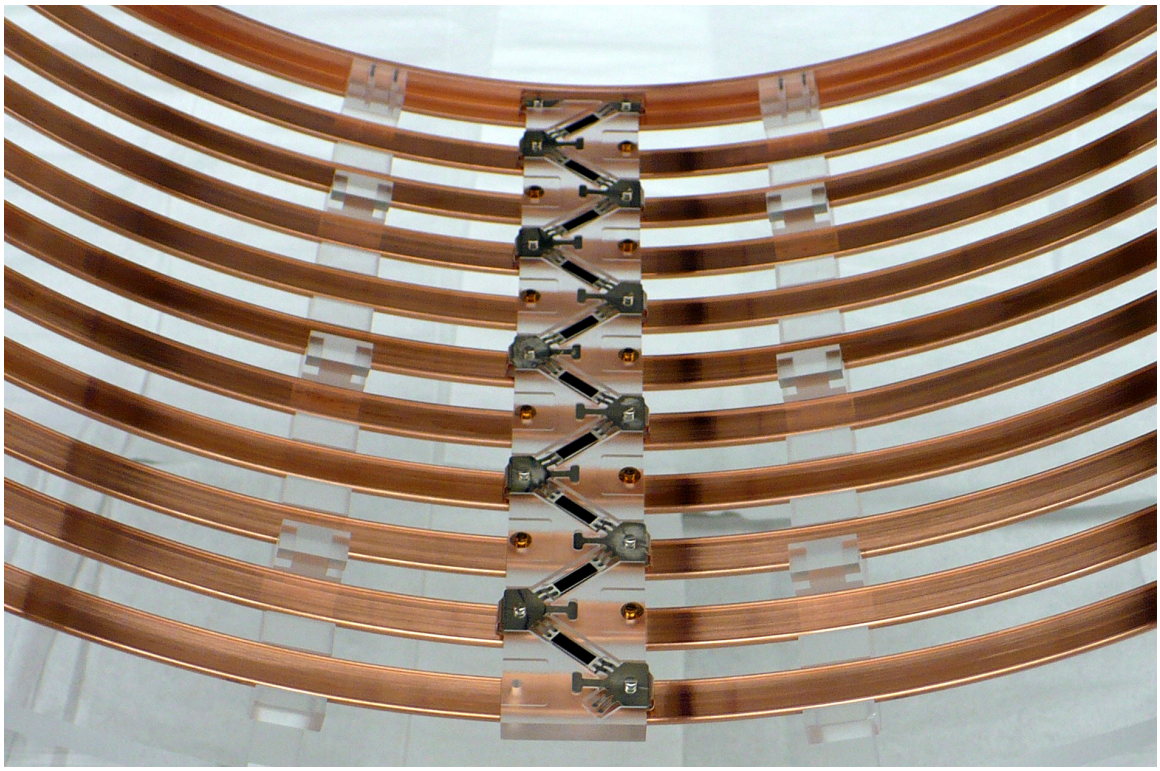

Figure 4.15: The resistor chain which grades the electric field in each TPC. Platinum plated phosphor-bronze springs make contact between the resistors and field shaping rings. The chain and field shaping rings are mounted on acrylic supports.

ionization wires. The resistors are custom made using thick film technology. A resistor and conductor paste, both by DuPont[102], are applied to a 0.33 x 1.31 x 0.09 cm sapphire substrate supplied by Swiss Jewel Co[103]. Fabrication of the resistors took place at Piconics[104]. 200 resistors were produced, from which two of the thirteen most closely matched sets were chosen for installation. The average resistance of each set is 0.879 and 0.908 GΩ, resulting in a total power dissipation of 1.1W at 3.7 kV/cm. Deviations from the mean of resistance in each set is less than 0.6%. Table 4.6 lists radioactive contamination of the resistor materials and fabricated parts. Background contribution from all 26 resistors is estimated to be 83-121 $2\nu\beta\beta$ and 0.4-0.5 $0\nu\beta\beta$ evts/yr, corresponding to 0.2-0.3% and 1.2-1.7% of tolerance respectively.

4.4 Signal Distribution

Due to the natural radioactive content of most electronic components, the electronics for the detector is located outside the lead shield, approximately 1 m from the LXe vessel (see figure 3.3). This was the result of a compromise, favoring a low background impact above lower electronic noise, which would be achieved with a cryogenic field-effect transistor (FET) located very close to the detector elements. Instead, scintillation and ionization signals, as well as APD and induction wire voltage, are carried from the APDs and wires to the electronics by an array of flexible cables. These cables were photo etched from adhesiveless polyimide flexible copper clad laminate[105] purchased through Nippon Steel Chemical Co[106].

A schematic showing the distribution of signals in one half of the TPC is shown in figure 4.16. The cables which make connections to detector components within the chamber are referred to here as interconnects in order to distinguish them from the cables which carry signal from the interconnects to the electronics, referred to here simply as cables. There are six cables, each of which lie within one of six rectangular tubes (referred to as 'legs') which are welded between the hatch of the inner cryostat and either end of the vessel (see figure 3.2). Each of the six cables services one of the two collection wire, induction wire, or APD planes.

Each of the four ionization wire planes makes contact with two interconnects,

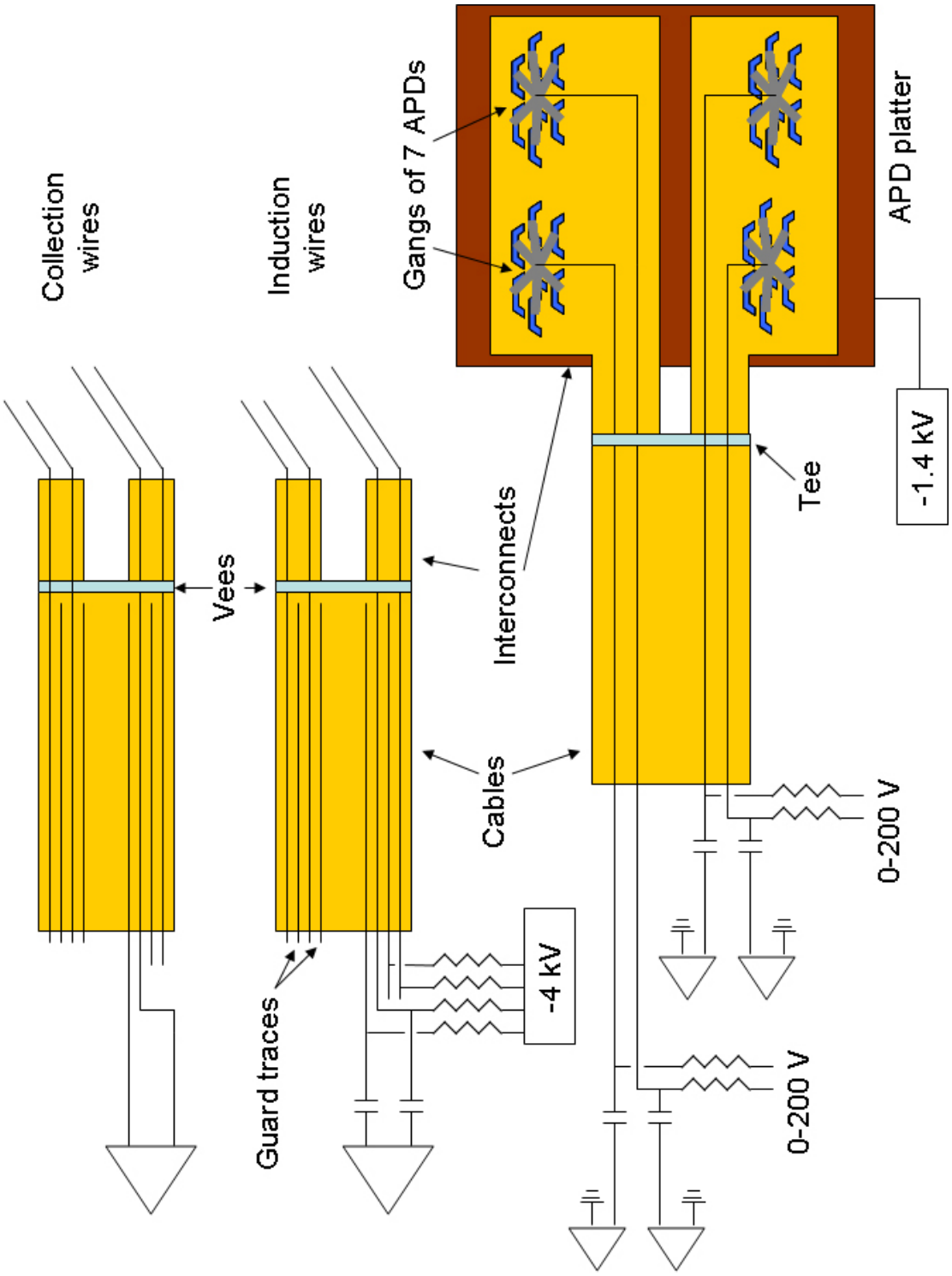

Figure 4.16: Schematic of signal distribution for one TPC half.

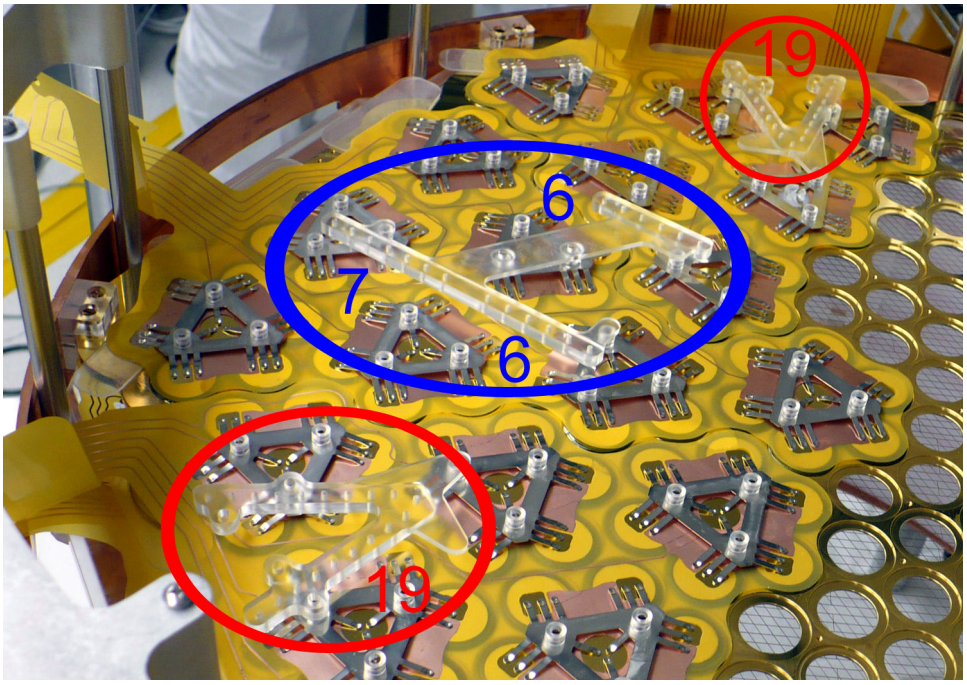

Figure 4.17: Acrylic 'T' (indicated in blue) and 'V' (indicated in red) blocks used to mate interconnects and cables. The number of channel connections made on each block is indicated.

each carrying 19 channels (see figure 4.3). Each APD plane makes contact to six interconnects, five carrying six channels and one carrying seven channels (see figure 4.6). The four pairs of ionization interconnects each mate with a cable on two acrylic 'V' shaped blocks bolted to the APD platter (see figure 4.17). Each of the two sets of six APD interconnects similarly mate with an APD cable on two 'T' shaped acrylic blocks.

A collection wire cable is shown in figure 4.18 (its features are representative of the induction wire and APD cables as well). The point of contact of the two sets of 19 traces with the acrylic 'V' blocks is indicated in the figure. Each cable is made up of several strips. When the cable is 'rolled' into a cable bundle, as shown in the figure, these strips lie on top of each other. The 25μm kapton substrate which the cables are made from breaks down at a bias of 5kV, and so is inadequate as an insulator for the 4kV induction wires. Thus, the cables are rolled around several sheets of 0.71 mm thick DuPont Teflon TE-6472 insulator. The Teflon sheet forming the cable bundle extends the length of each copper leg, stopping at the cable feedthrough located on the hatch of the inner cryostat.

Some of the strips etched into the cables are conducting planes, which serve a variety of purposes (see figure 4.19). In the case of the collection wire cables, such planes provide a 50 mΩ ground connection for the TPC. In the case of the induction wire cables, the potential of the traces can be as high as 4kV. The close proximity of these traces to the grounded vessel leg can result in significant microphonic induced noise. Thus, conducting planes biased at the trace voltage tightly surrounded the trace strips. Finally in the case of the APD cables, one conducting plane provides the $\sim$1.4kV bias to the APD platter. Its large width provides a low inductance AC return path, required by the very short $\sim$50ns rise time of the APD signals. This plane is placed very close to the traces to reduce ground loops, but this proximity creates a potential microphonic noise issue because the traces are biased far lower, at $\leq$200V. Thus a second grounded conducting plane is inserted between the traces and the first conducting plane.

The trace patterns on the collection and induction wire cables are very similar. There are two trace strips per cable, with 19 traces on each strip. Starting at the

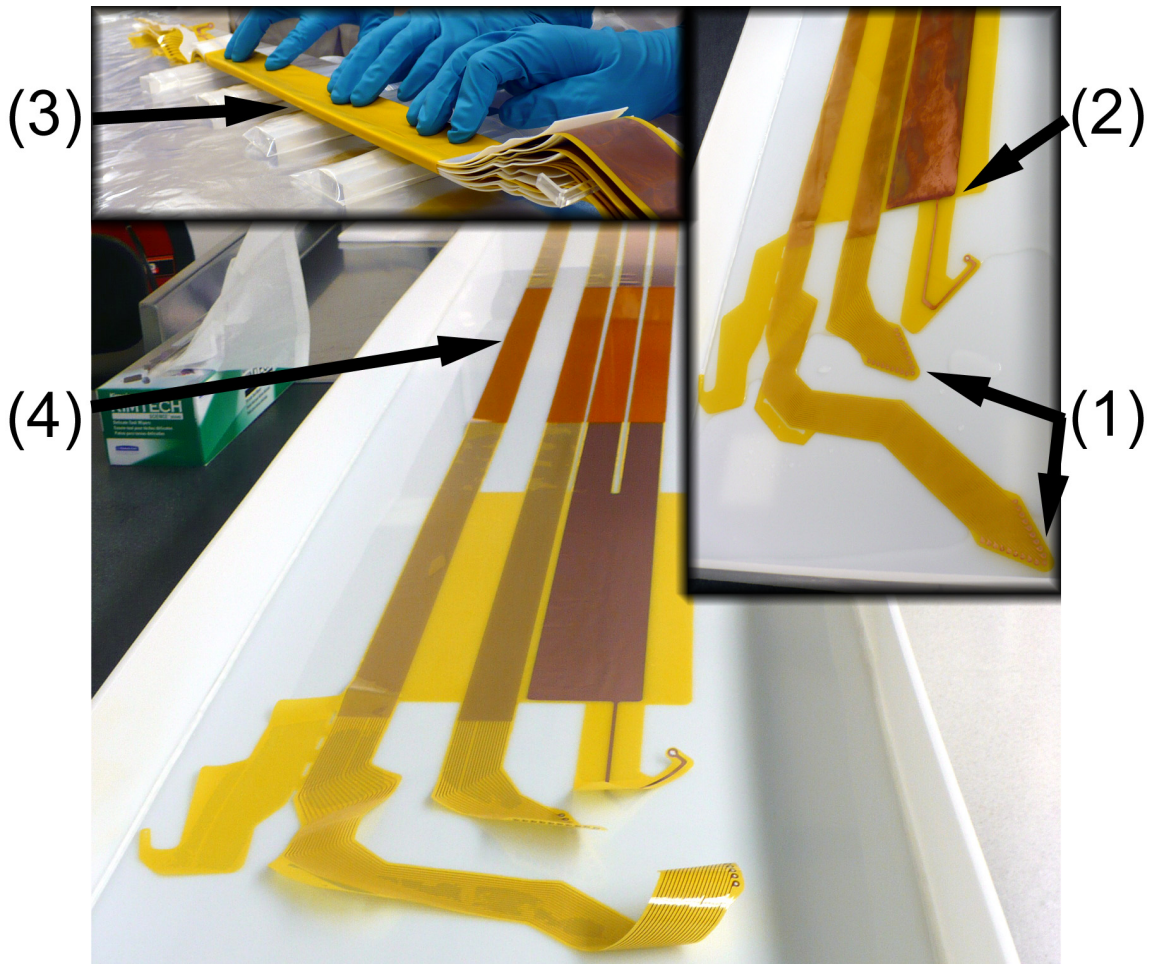

Figure 4.18: A collection wire cable. (1) Features at the head of the cable that mate with acrylic 'V' blocks. (2) Conducting planes used to mitigate microphonic noise and improve electrical connections. (3) The cable bundled with Teflon insulators. (4) Coverlay applied to cable outside of inner cryostat.

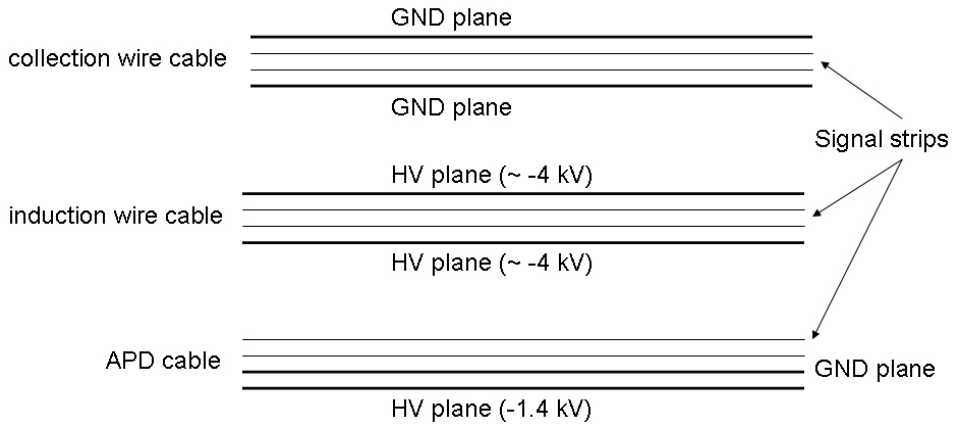

Figure 4.19: Schematic showing the conducting planes in each of the three types of cable.

electronics box, each trace is bordered on either side by guard traces, which are not connected to detectors and serve as ground in electronics comparators. The 20 guard traces terminate at the barrel of the TPC, with the remaining 19 signal traces continuing to the 'V' blocks on the back of each TPC half. Trace pitch is 1 mm, with a trace width of 0.5 mm. 2 mm of bare kapton lay to side of the outer most traces, for a total cable width of 43.5 mm.

Design of the trace pattern on the APD cables was dominated by the requirement that an APD failure of one APD would not bring the bias of one of the APD traces up to ∼1.4 kV, resulting in breakdown to a nearby trace at far lower potential. Thus the 37 traces on each APD cable were split among three strips, and guard traces were omitted. This allows a trace pitch of 3 mm.

Trace resistance for all of the cables was measured to be 20.5 mΩ/cm, resulting in a total resistance of ∼5 Ω for each trace. The capacitance between signal and guard traces on collection and induction cables was measured to be 30 pF.

Pyralux FR Coverlay[107] was applied to 68.6 cm of each cable, starting after the cables exit the inner cryostat hatch. These coverlays further insulate the conductors on the cable as well as increase cable durability. ICPMS measurements of the coverlay material revealed <3.2 pg/cm^2 ^{232}Th and 2.0±0.6 pg/cm^2 ^{238}U contamination, levels too high to use very close to the TPC, but negligible outside of the inner cryostat.

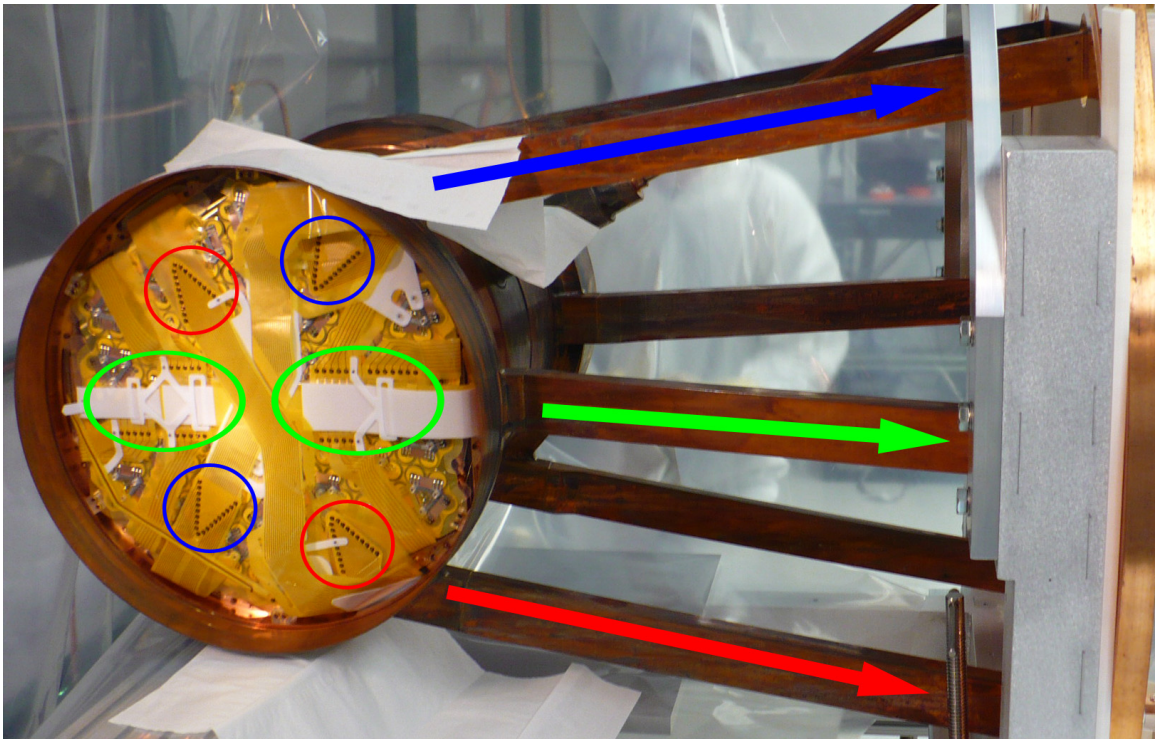

Figure 4.20: A view of one end of the TPC as installed in the copper vessel. The path and connections of induction wire cables are indicated in red. Blue similarly indicates collection wire cables, and green APD cables.

Figure 4.21: Two Teflon half circles prevent shorts to the copper end caps.

Figure 4.20 shows the back of one assembled detector half inside the LXe vessel. The connections that the three cable bundles make at the back of the detector plane are highlighted. Also visible in the figure are additional Teflon protectors, which constrain the cables and interconnects and prevent electrical shorts. Figure 4.21 shows two half circles of Teflon covering the entire cable network, offering additional protection from shorts to the copper end caps which seal the vessel. Holes in the Teflon half circles improve LXe circulation and purification. To further reduce the risk of electric breakdown or inadvertent electrical contact, the copper legs holding the cables are lined with 0.71 mm thick Teflon sheet.

All EXO-200 flexible cables were photo etched by FlexCTech[108]. The photo etching process was carefully monitored throughout production. Gloves, fresh chemicals, and new chemical containers were used though cupric chloride, the principal etchant, was too expensive to refresh. Several isopropanol rinses were added to the standard process. In addition, all interconnects were subject to a post-production plasma etch.

Upon receipt interconnects and cables were given different cleaning treatments. Interconnects were soaked in acetone then ethanol for one day each with a DI water rinse in between. They were then dipped in 7% and 3% HCl solutions for 20 seconds each, with 20 second rinses in fresh DI water following each acid dip. The parts were allowed to soak in fresh ethanol for another day before being stored in a dry box. Prior to insertion, the interconnects saw another two HCl dips, each followed by a rinse in DI water, and a final ethanol rinse.

Cables are much more delicate, but also located mostly farther from the active region of the detector. Thus they were subject to a less aggressive treatment. Each was soaked in acetone then ethanol for 15 minutes, with DI water rinses after each soak. They were physically agitated by wiping with a cloth during soaking. This was followed by 1 minute soaks in 7% and 3% HCl solutions, with a DI water rinse between soaks. Finally, the cables were subject to two fresh DI water rinses, then an ethanol soak before being pat completely dry with cloth wipes.

The mass density of flexible cable varies between 3.6 and 14.8 mg/cm^2 depending the density of copper trace (the coverlay adds an additional 6.6 mg/cm^2). The total

Component	^{232}Th [pg/cm^2]	^{238}U [pg/cm^2]	Total area [cm^2]
cables	<1.7	5.7±0.7	7406
interconnects	<2.3	4.7±0.7	10825

Table 4.7: Average radioactive contamination of flexible cables in pg/cm^2. ^{40}K contamination levels are unavailable because ICPMS was used.

mass of cable and interconnects installed is 133 g. Despite great effort, the contamination of cleaned flexible cables (shown per unit area in table 4.7) is relatively high. Based on these measurements Monte Carlo predicts a total background contribution of 1062-1755 $2\nu\beta\beta$ evt/yr and 3.6-6.0 $0\nu\beta\beta$ evt/yr, corresponding to 2.7-4.4% and 11.9-20.1% of tolerance, for both interconnects and cables.

4.5 Liquid Xenon Vessel

The TPC is housed in a thin copper pressure vessel. This vessel is welded to the hatch of the inner cryostat (see figures 3.2 and 4.20). The driving concern behind the vessel's design was reducing background impact by minimizing total mass. The design criteria required that the vessel be able to withstand a 33.3 kPa differential pressure at the height of the center of the vessel. Minimizing the volume of inactive isotopically enriched LXe was also a significant concern due to its high cost.

The LXe vessel (see figure 4.22) is a cylindrical tube of inner diameter 39.62 cm with flared ends of radius 45.47 cm. Two rectangular legs separated azimuthally by 20° extend from each end of the vessel. A third leg on each end, bisecting the azimuthal angle subtended by the other two, extends outward at 15° from the plane of the other two legs. The cross section of each leg matches the thickness of the cable bundle inside it to minimize the volume of inactive xenon. As viewed looking at the inner face of the inner cryostat hatch, the upper left and lower right legs have inside cross section of 2.54 cm × 5.08 cm, the upper right and lower left legs have cross section 1.27 cm × 5.08 cm, and the middle legs have cross section 2.14 cm × 5.08 cm. A feedthrough at the center of the barrel houses the the cathode HV connection. The far end of each vessel leg mates with a disk shaped 'foot' which is TIG welded to

Figure 4.22: The LXe vessel without end caps (left). A vessel endcap (right).

the inner cryostat hatch. The wall thickness of most of the vessel is 1.5 mm. The end caps of the vessel are reinforced by 12 spokes, 2.56 cm high. The barrel is reinforced by four 6.4 mm long regions of 2.9 mm radial wall thickness. The inner surfaces of the end caps are separated by 44.5 cm.

Detailed finite element analysis (FEA) was performed on the vessel design. The copper used to fabricate the vessel was assumed to be equivalent to the weakest high purity copper listed in the ASME Code: C10200 SB-187 copper rod, with minimum specified yield strength of 42 MPa and minimum specified tensile strength of 150 MPa. Buoyancy, liquid head effects both inside and outside the vessel, and buckling were considered in the calculations. All realistic combinations of full and empty vessel and cryostat were examined. The following maximum stress guidelines were used:

- Primary membrane stress: 28.5 MPa
- Primary membrane plus bending stress: 42.7 MPa
- Primary local membrane plus secondary bending stress: 85.4 MPa.
- Shear stress: 14.2 MPa.

The FEA showed that vessel stresses in all possible configurations lie below the maximum tolerable:

- Maximum vertical vessel displacement of 0.5 mm occurs when the vessel is full of LXe and immersed in HFE.

- Maximum primary stress intensity occurs when the vessel is empty and immersed in HFE with a 26.8 kPa external overpressure. In this case the stress in the end caps is 20.4 MPa. Extrapolation suggests that maximum allowable primary membrane stress would be exceeded at an external overpressure of 41.3 kPa.

- Maximum secondary stress occurs when both the vessel and inner cryostat are empty with no pressure differential. In this case a secondary stress of 32.2 MPa occurs at the junction of the middle vessel leg on the left and body.

- Maximum shear stress occurs when the vessel is full of LXe, immersed in HFE, and an external overpressure of 26.8 kPa is applied. In this case a shear stress of 1.1 MPa occurs at the leg/hatch junction for the thinner of the lowest two legs. Membrane plus bending stress at this location in this case is 20.7 MPa.

- The explosive (implosive) pressure rating of the barrel is 204 (41.9) kPa.

- The worst case buckling scenario for the legs of the vessel occurs for the thinner of the two lowest legs when the vessel is empty, immersed in HFE, and an external overpressure of 5psi is applied. This leg experiences a load of 65 kg, well below the predicted buckling load of 3300 kg.

The LXe vessel was constructed from high purity OFRP electrolytic copper cast at Norddeutsche Affinerie (now Aurubis) in Hamburg Germany[109]. Once formed and rolled into 25mm and 5mm sheet, the copper was stored in a concrete bunker at DESY[110] for 90 days. The copper was then rolled, taking 20 days at sea level, then transported to Stanford University by sea in a 2 m.w.e shielded shipping container, taking 45 days.

Storage and machining of the copper at Stanford University took place with 7 m.w.e concrete overburden over a period of 3 years. Copper for the vessel was in large part machined using a new computer numerical control machine. Some parts

Component	^{40}K	^{232}Th	^{238}U	Quantity
tig welding	N/A	4±3 pg/cm^2	10±3 pg/cm^2	93.2 cm
e-beam welding	N/A	8±2 pg/cm^2	< 12 pg/cm^2	2058 cm
Vessel + TPC copper	<6.4 pg/g	<3.6 pg/g	<3.8 pg/g	31614g + 9826g

Table 4.8: Background contamination of the copper used to fabricate the vessel and some TPC components, in pg/g. Contamination added by welding shown in ng/cm. Total length of weld in the copper vessel, and mass of the vessel and tpc components are also shown.

were machined on an older lathe. Only new carbide tools and ValCool-VP-700-005-B[111] coolant diluted with DI Water was used.

47 welds were required to fabricate the vessel. 2058 cm of copper were welded using electron beam welding at Applied Fusion[112]. The remaining 93.2 cm (final two endcap welds, and the connection of the HV tube to the HV feedthrough on the barrel) were TIG welded at Stanford University in a class 1000 cleanroom environment. Ceriated tungsten tips were used for TIG welding. Prior to each weld, weld surfaces were cleaned as described in section 3.5. In total, the welding at Applied Fusion took < 2 days at sea level.

Once the vessel was fully machined and welded (except for the endcap and HV tube welds), the entire vessel was cleaned as described in section 3.5. HCl was used instead of HNO_3. The six vessel feet were then TIG welded to the inner cryostat hatch, the HV tube was TIG welded in place, and the TPC halves were inserted into each end of the vessel. Cables were then fed through the legs and connected to the TPC. After all connections were verified, the end caps were TIG welded onto the vessel. The weld surface on the vessel was not cleaned prior to welding due to the proximity of the very delicate TPC components.

Transport to WIPP took place in a 2 m.w.e shielded shipping container over 36 hours. Once at WIPP, the TPC lay without taking data for > 240 days.

Intrinsic contamination of the copper used to fabricate the vessel, as well as contamination added during welding, is shown in table 4.8. Some TPC components (the support frame, cathode support rings, field shaping rings, and APD platters) were fabricated using the same copper batch, and are included in this background analysis.

Isotope	$2\nu\beta\beta$ [evt/yr]	$0\nu\beta\beta$ [evt/yr]	$T_{1/2}$ [days]
^{54}Mn	<251	0	312
^{56}Co	<43	<0.30	77.3
^{58}Co	<258	0	70.8
^{59}Fe	<3	0	44.5
^{60}Co	<745	<1.10	1925
^{65}Zn	<158	0	244
Total	<1459	<1.39	

Table 4.9: Upper estimate of the contribution to background rate in counts/year for cosmogenic isotopes activated in the LXe vessel.

The welds increase total ^{232}Th and ^{238}U background contamination of the vessel by 18%, assuming contamination levels at upper limits. Total background contribution of the vessel and copper TPC components is estimated to be 108-18219 $2\nu\beta\beta$ and 0.5-32.9 $0\nu\beta\beta$ events/year, corresponding to 0.3-45.6% and 1.6-109.6% of tolerance respectively.

For analysis of cosmogenic activation, the production sequence outlined above was conservatively simplified to:

1. 30 days at sea level
2. 3 years at 7 m.w.e
3. 2 days at sea level
4. 1.5 days at 2 m.w.e
5. 240 days of cooldown

An upper estimate for the total contribution to yearly background rate for each cosmogenic isotope at the end of cooldown is listed in table 4.9, based on the equations, production rates, and hit efficiencies given in section 3.7. This corresponds to <3.6% of $2\nu\beta\beta$ and <4.6% of $0\nu\beta\beta$ tolerance.

The largest contribution comes from ^{60}Co, which is also the longest lived isotope, with a half life roughly equal to the ∼5 yr life of the experiment. Contributions from other isotopes becomes small on a time scale of ∼1 yr.

Source	^{222}Rn atoms/day
Teflon tiles	<28
Flexible cables	<23
APD Spiders	<673
Ionization wires	<421

Table 4.10: Major contributors to radon emanation in the TPC.

4.6 Other TPC Considerations

As discussed in section 3.2, ^{222}Rn emanation of TPC components is a significant potential $0\nu\beta\beta$ background. Simulation has shown that the $0\nu\beta\beta$ hit efficiency for ^{222}Rn decay in the LXe is 0.0039 $0\nu\beta\beta$ background/decay. Thus, the continuous presence of one ^{222}Rn atom in the detector at any given time (corresponding to an emanation rate of Log(2)/3.8 = 0.18 atoms/decay) results in

$$ln(2)/0.0104 \cdot 0.0039 = 0.26 \tag{4.1}$$

$0\nu\beta\beta$ background events/yr. (0.0104 is the ^{222}Rn half-life in years.)

Table 4.10 shows upper limits measured for some of the TPC components by radon counting. Unfortunately, radon emanation from these components is extremely difficult to quantify at the ∼atom/day level without a detector as sensitive as EXO-200 itself. These upper limits say little about the tolerability of radon emanation from within the TPC.

Also mentioned in section 3.2 is the issue of ^{210}Pb plating of TPC components or the LXe vessel during construction and handling. No quantitative study of this method of surface contamination was performed. If one conservatively assumes that every radon decay within the volume of the vessel (55 l) results in a ^{210}Pb atom plated to the TPC, and that the radon level in air is 150 mBq/l, one calculates that 0.7 mBq will the plated to the TPC for every day of exposure to air. Monte Carlo simulation shows a $2\nu\beta\beta$ hit efficiency of 2.4×10^{-3} for each ^{210}Pb decay on the interior surface of the TPC. Thus one would expect a yearly $2\nu\beta\beta$ background contribution of 54 events for each day of exposure to air. While work was not being performed on the TPC

or LXe vessel, all TPC components and the inside of the LXe vessel were kept under a boil-off N2 atmosphere, in which any ^{222}Rn contamination had decayed away. A conservative estimate of 2 months exposure to air, at 8 hrs/day, after the final acid cleaning of each component gives 1075 $2\nu\beta\beta$ evt/yr, or 2.7% of tolerance.

The outside of the LXe vessel was not stored under ^{222}Rn-free atmosphere. The $2\nu\beta\beta$ hit efficiency of ^{210}Pb plated to the outside of the LXe vessel was calculated to be 1.7×10^{-5}, a factor of 200 less than the hit efficiency for the inside wall of the TPC. If one assumes a plating rate equal to that calculated above for the inner TPC walls, and one year of exposure to air after the final acid cleaning of the LXe vessel, one finds the contribution from external ^{210}Pb plating to be 140 $2\nu\beta\beta$ evt/yr, or 0.3% of tolerance.

Finally, a study on the efficiency of discrimination of gamma events from $2\nu\beta\beta$ and $0\nu\beta\beta$ using topology has been performed by Monte Carlo. The background rejection criterion requires that an event produce a signal on only a single wire channel, or an adjacent pair of wire channels for each of the wire planes on a detector half. It also requires that the event energy depositions be contained within 2 cm in the axial dimension of the detector. Events which satisfy this criterion are referred to as 'single site' events. The background rejection efficiency of these criterion depends strongly on the mean free path of the gammas involved, which depends on the energy of each gamma (see section 2.8). The gamma energy in turn depends on the decaying isotope and its location in the detector. The background rejection efficiency ranges from 75% to 98%, with a typical value of 85% for $0\nu\beta\beta$ candidates. Since $2\nu\beta\beta$ events have lower energy, background gammas at these energies have a shorter mean free path, making the rejection efficiency smaller. Monte Carlo predicts a rejection efficiency of 50% to 80% for $2\nu\beta\beta$ candidate events. These background rejection efficiencies are already included in the Monte Carlo hit efficiencies given in tables 3.2, 3.3, and 3.4.

Also of interest is the acceptance efficiency of $2\nu\beta\beta$ and $0\nu\beta\beta$ events based on these criteria. Based on the very short mean free path of electrons in LXe indicated in figure 2.4, one might hypothesize that very few $\nu\beta\beta$ events would be rejected. Unfortunately, in many cases the scattering of electrons in LXe produce bremsstrahlung radiation, which can travel a many cm from the decay site (or even outside the detector) before

interacting. Since $2\nu\beta\beta$ produces electrons with lower energy, the corresponding bremsstrahlung radiation does not penetrate as far, and the acceptance efficiency increases. The acceptance efficiencies are predicted to be 86.8% for $0\nu\beta\beta$, and 96.8% for $2\nu\beta\beta$.

Chapter 5

External Detector Components

The LXe TPC thus far presented is welded to the inner hatch of the inner vessel of a double walled copper cryostat. The cryostat is surrounded by a lead shield. Three fluid systems service the cryostat, providing cooling, HFE, and xenon. The entire experiment is located in a class 100 clean room at the Waste Isolation Pilot Plant near Carlsbad, New Mexico. This chapter will present details on each of these aspects of EXO-200.

5.1 Inner Cryostat

A schematic of the double walled copper cryostat is shown in figure 3.2. The cross section of the inner cryostat is a regular dodecagon of inner height 143.8 cm (shown in figure 5.1). The corners are rounded with inner radius 8 cm. The wall thickness of all plates is 2.7 cm. The total copper mass of the inner cryostat is 2740 kg.

The inside distance between front and back plates of the inner cryostat is 146.8 cm. When mounted in the inner cryostat, the center of the chamber is located 74.6 cm from the hatch and back wall, 71.2 cm vertically from the inner walls, and 71.9 cm horizontally from the inner walls. Total volume of the inner cryostat without the LXe vessel is 2440 liters.

The inner cryostat volume is filled with 3M Novec Engineered Fluid HFE-7000[75], referred to here as HFE. HFE is moved into and out of the cryostat via two ports.

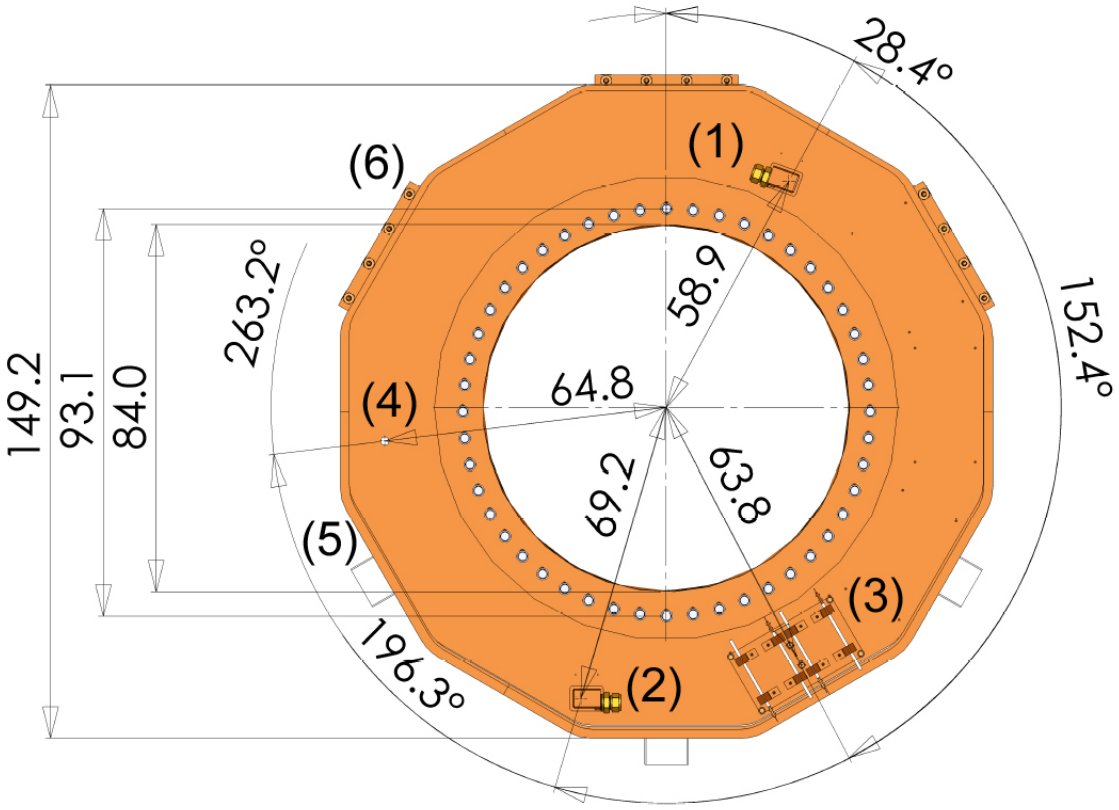

Figure 5.1: Diagram of the front face of the inner cryostat. (1) HFE Outlet, (2) HFE Inlet, (3) Cryostat heater, (4) Calibration feedthrough, (5) Teflon pads, (6) Heat Exchangers. Measurements in cm.

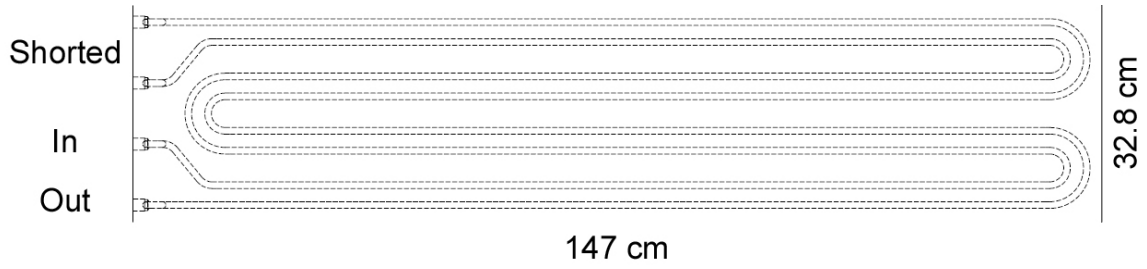

Figure 5.2: The refrigerant path in each of the three heat exchangers welded to the top of the inner cryostat.

The inlet port is located at the bottom of the cryostat, on the front face at 69.2 cm radius and an angle of 196.3° from vertical. The outlet port is located at the top, 59.0 cm radius and an angle of 28.4°. A face seal connection using indium plated copper gaskets adapts a copper right-angle block welded on each port to 1 inch Swagelok fitting. A copper tube is connected to each port inside the cryostat, reaching within 2 cm of the bottom and top of the cryostat.

A heater, consisting of two 32 mil Ni-Cr wires from MWS Wire Industries[113] sandwiched between 90 μm of kapton and a 5 mm thick copper plate, is located at 63.8 cm radius at an angle of 152.4°. The heater measures 15.5 cm $\times$ 27.4 cm. The kapton used is fully etched flexible cable stock, and prevents electrical connection between the cryostat the heater power source.

Finally, a feedthrough for calibration sources is located at radius 64.8 cm and an angle of 263.2°.

A total of 7 Teflon pads, measuring 5.11 cm in thickness and 10 cm square, support the inner cryostat and distance it from the outer cryostat. Two pads are located at the 4:00 and 8:00 positions, and three at the 6:00 position when facing the front of the inner cryostat. The front edges of the pads are located 9.6 cm, 69.6 cm, and 129.6 cm from the front face of the inner cryostat. The inner cryostat is longitudinally referenced to the outer by the front center pad. The remaining pads are not constrained.

Three heat exchangers were obtained by machining refrigerant paths, shown in figure 5.2, into three copper plates, 32.8 cm $\times$ 147 cm, then welding the plates to

the inner cryostat itself. A face seal connection using indium plated copper gaskets adapts each heat exchanger port to 1/2 inch Swagelok fitting.

An 83.6 cm diameter opening is cut into the front plate of the cryostat. A bolt circle of diameter 93.1 cm surrounds this opening and accommodates 48 1/2-13 stainless steel helicoils from Emhart Teknologies[114], used in fastening the hatch of the inner cryostat. The bolts and lock washers used to fasten the hatch were purchased from McMaster-Carr[115] and made from silicon-bronze. Each was vented at the Stanford machine shop. The hatch, shown in figure 5.3, is comprised of a 2.5 cm thick disk of copper, 103.0 cm in diameter. 6 ports of 7.0 cm diameter accommodate the chamber feet, with a 7th port of 4.7 cm used for the HV tube.

Because the inner cryostat is at LXe temperatures during normal operations, elastomer o-rings could not be used to seal any of its ports. The hatch is instead sealed to a polished surface on the front wall of the inner cryostat using a custom made "U-Mega" seal gasket created by Jetseal[24]. The gasket was formed from 0.8 mm thick 1/2 hard phosphor-bronze sheet, purchased from Lamineries Matthey SA[116]. The sealing tips of the gasket were coated at the SLAC plating shop with 125 μm of indium. The cross section of the gasket is shown in figure 5.4. A 87.9 cm diameter, 0.826 cm wide, 0.465 cm deep groove cut into the hatch houses the U-Mega seal. Four phosphor-bronze retaining tabs hold the U-Mega seal in place during hatch installation.

The 6 feet of the chamber are TIG welded to 6 ports on the inner cryostat hatch. Feedthrus for the flexible cables passing through each chamber leg are formed in copper flanges using a two component epoxy by MasterBond[117] (see figure 5.5). Fabrication of each feedthru was a two step process. First, pieces of U-shaped acrylic were bonded to the cables using a very small amount of epoxy, forming a sealed cup. Liquid epoxy was then poured into the cup, bonding the cables and cup to a very thin copper lip on each flange. The very thin lip allowed the epoxy to contract and expand without cracking through thermal cycling. An identical method was used to create cable feedthroughs through the outer cryostat hatch.

Potting of a cable through both hatch flanges took place prior to cable installation. The cable with flanges was then inserted into a leg of the chamber (which was welded

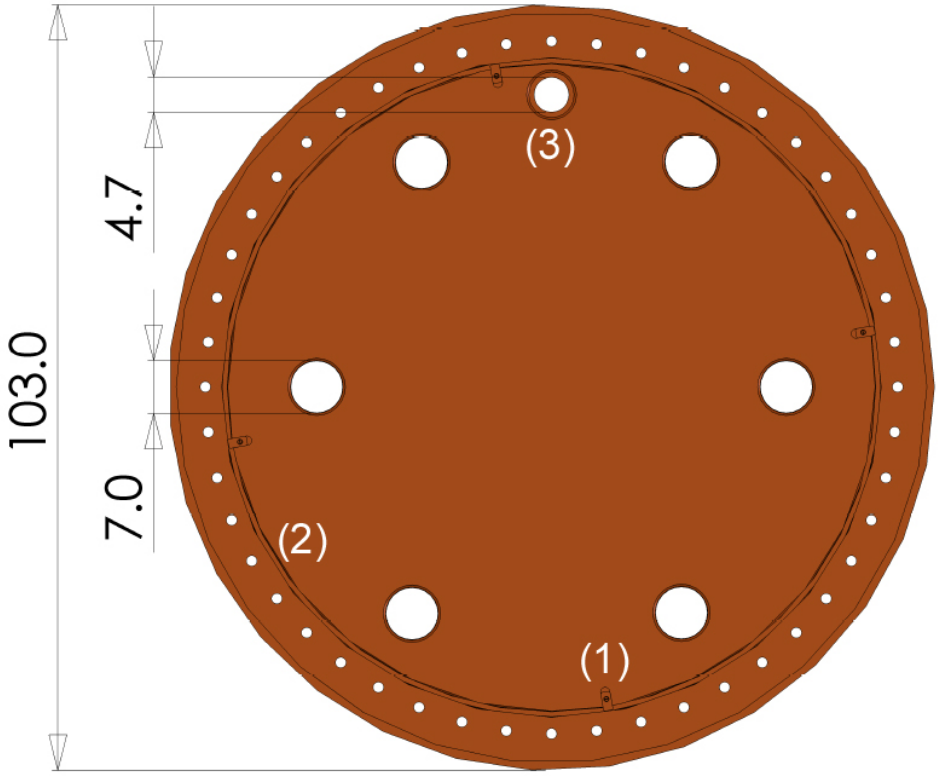

Figure 5.3: Inside view of the inner cryostat hatch. (1) Retaining tabs for holding the U-Mega seal in place, (2) U-Mega seal groove, (3) HV port. Measurements in cm.

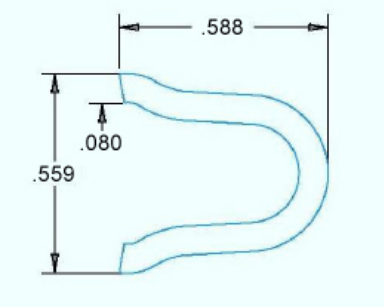

Figure 5.4: The cross section of the U-Mega seal purchased from Jetseal[24]. Measurements in cm.

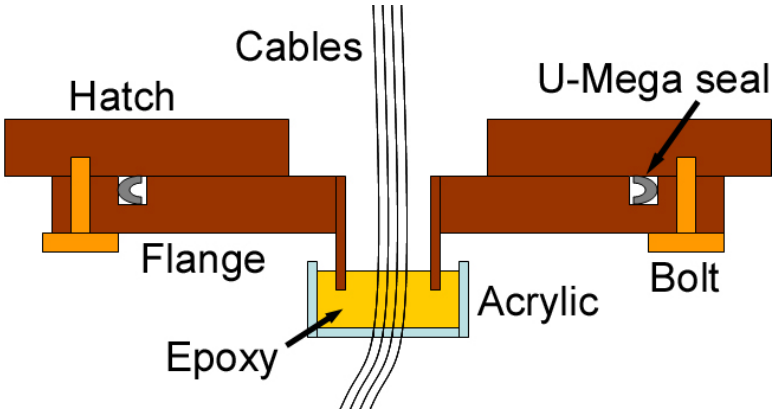

Figure 5.5: A schematic of a cable feedthrough flange on the inner cryostat hatch. Cable feedthrough flanges on the outer cryostat hatch use a silicon o-ring in place of a U-mega seal.

to the inner cryostat hatch). The inner cryostat hatch flanges were bolted to the inner cryostat hatch, while the outer cryostat hatch flanges were held in place on the inner cryostat hatch by copper brackets. The outer cryostat hatch flanges were then bolted to the inside of the outer cryostat hatch only after both the inner cryostat and outer cryostat hatches were sealed (see figures 5.6 and 5.7). The length of cables lying between the inner and outer cryostat hatches is protected on either side by teflon strain reliefs.

The upper shielding wire cable flange has a 1/2 inch xenon input port as well as a feedthrough for cables. The lower shielding wire cable similarly has a xenon output port, though this port has a 1 inch diameter since it is also used for initial evacuation of the chamber. The inner cryostat cable flanges seal to the inner cryostat hatch using 9.7 cm diameter "U-Mega" seals. (The outer cryostat cable flanges were sealed to the outer hatch using o-rings, as described in the following section.)

The full surface of the inner cryostat is wrapped in 5 layers of aluminized mylar super insulation from Sheldahl[118]. 4.96×10^5 cm^2 of superisulation is used. A very small amount of kapton tape of unknown origin (from the stockroom of the Stanford Physics department) was used to secure the super insulation to the cryostat. Contamination in the tape was measured using direct counting, allowing use of the very material that was counted.

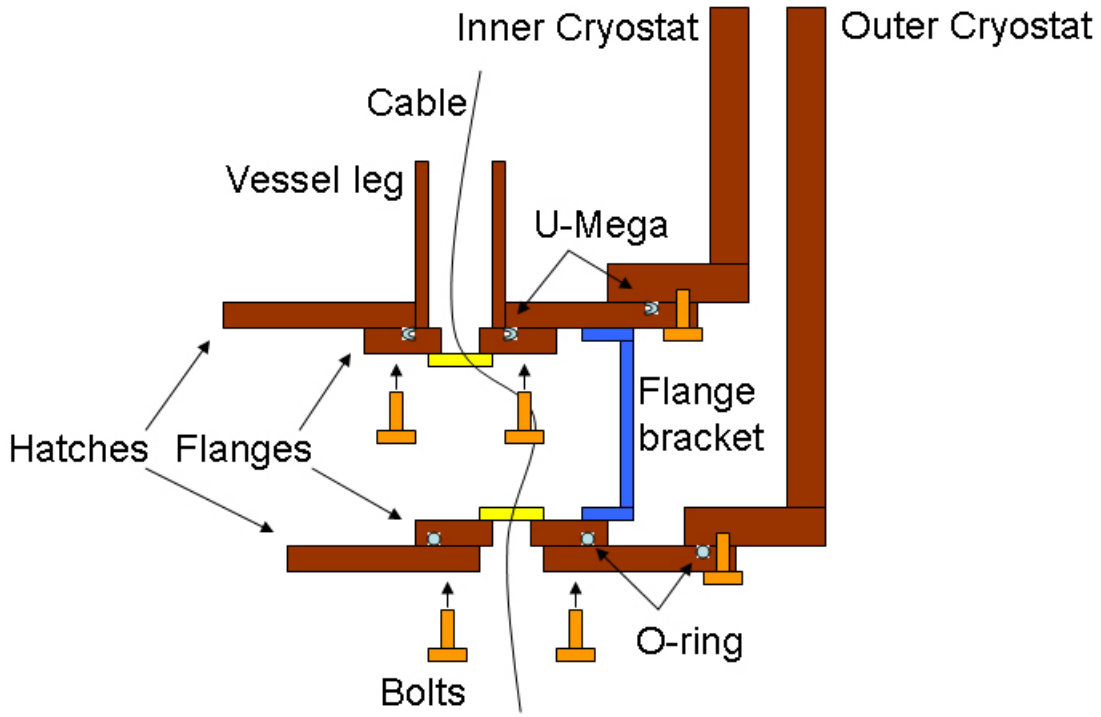

Figure 5.6: A schematic of a cable fed through the inner and outer cryostat hatches.

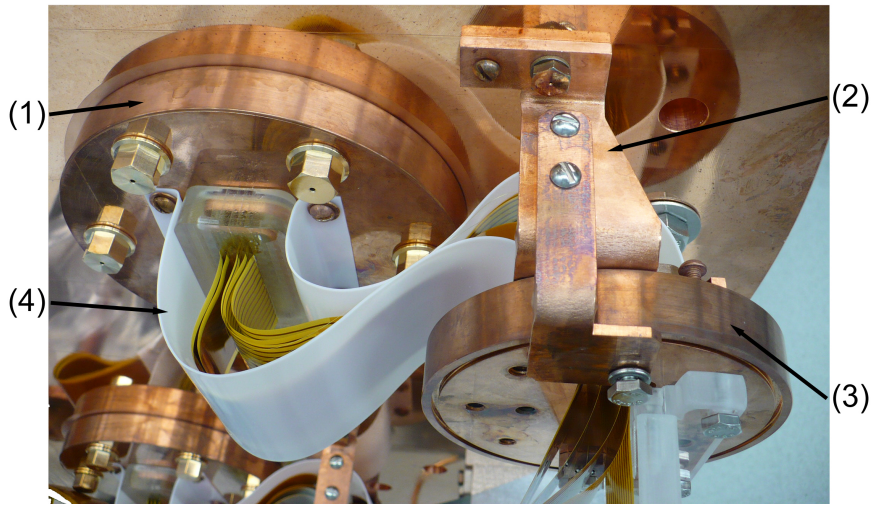

Figure 5.7: A view of a cable installed on the inner cryostat hatch. (1) The inner cryostat cable flange. (2) The outer cryostat cable flange bracket. (3) The outer cryostat cable flange. (4) The teflon strain relief.

Material	^{40}K [pg/g]	^{232}Th [pg/g]	^{238}U [pg/g]	Mass [g]
Ni-Cr Wire	44±10	438±91	496±63	29
Helicoils	<27.5	<55.7	<148	1498
Epoxy	<106	< 886	<310	351
Hatch bolts	44.6±23.1	<379	211±81	6144
Hatch lock washers	16.1±1.6	7.68±2.36	<4.15	653
Kapton tape	<4360	<5370	<5822	30
U-Mega Seal	<29	50±3	78±4	2778
Inner cryostat copper	0.05	<0.8	<0.8	2.74×10^6
Super Ins. [pg/cm^2, cm^2]	0.048±0.003	<1.6	5.1±1.2	4.96×10^5

Table 5.1: Radioactive contamination and total installed mass of many inner cryostat components in pg/g, except as noted for super insulation. The first 6 entries were measured using direct counting. The remaining 3 were measured using ICP-MS. Total masses of epoxy, helicoils, and hatch bolts/washers reflect those used on both the inner and outer cryostat.

The copper used to fabricate the cryostat came from Aurubis[109] (formerly Norddeutsche Affinerie), the same source as copper used to fabricate the TPC. Favorable conditions during the ICP-MS analysis of this lot of copper made more sensitive contamination measurements of ^{40}K, ^{232}Th, and ^{238}U possible.

Radioactive contamination of each of the above described components is given in table 5.1. These components together contribute 53-185 $2\nu\beta\beta$ evt/yr and 0.2-1.2 $0\nu\beta\beta$ evt/yr, corresponding to 0.1-0.5% and 0.6-4.0% of tolerance. Construction details, and an analysis of background impact due to cosmogenic activation, will be presented at the end of section 5.2.

5.2 Outer Cryostat

The cross section of the outer cryostat is a dodecagon of outer height 166.2 cm. The corners are rounded with outer radius 10.7 cm. The wall thickness of barrel and back wall is 2.7 cm. The back wall is reinforced with an additional 2.7 cm thick plate 80 cm in diameter. The inside distance from the reinforcement plate to front of the outer cryostat is 165 cm.

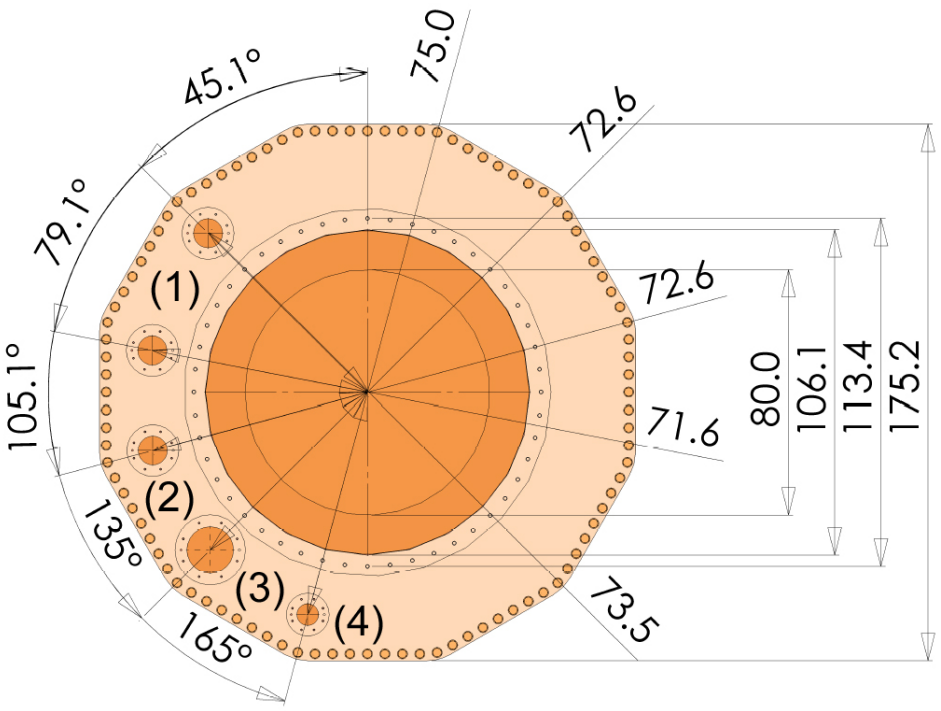

Figure 5.8: Diagram of the front face of the outer cryostat. (1) Refrigeration feedthroughs, (2) Thermocouple feedthrough, (3) HFE feedthrough, (4) Vacuum feedthrough.

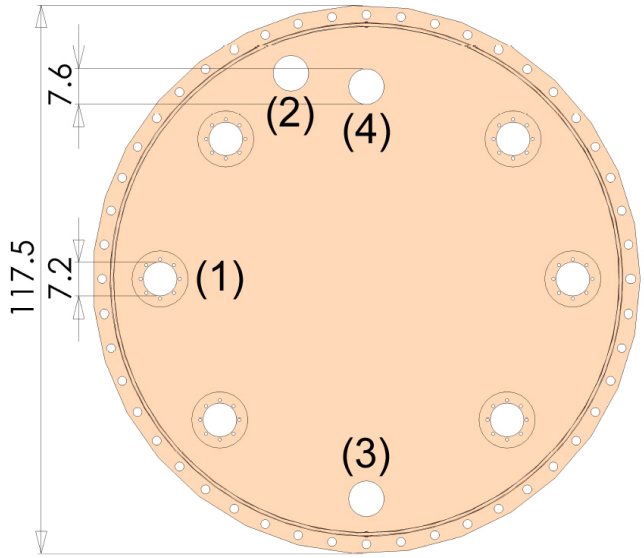

Figure 5.9: Inside view of the outer cryostat hatch. (1) 6 cable ports, (2) xenon inlet port, (3) xenon outlet port, (4) HV port.

The front of the outer cryostat is comprised of a removable 'crown' (see figure 5.8), allowing insertion of the inner cryostat. The crown mounts onto a dodecagonal lip of height 175.2 cm. 96 5/8-11 silicon-bronze bolts and washers, purchased from McMaster-Carr[119], screw into helicoils and fasten the crown. An opening with 106.1 cm diameter allows access to the inner cryostat hatch. A 113.4 cm diameter bolt circle accommodates 48 1/2-13 stainless steel helicoils, used to seal the outer cryostat hatch.

To the left of the hatch lie 5 ports. The first two, located at 73.5 cm radius, 45.1°, and 71.6 cm radius, 79.1° from vertical, have diameter 9.5 cm and service refrigerant. The third, located at 72.6 cm, 105.1°, also has diameter 9.5 cm and services thermocouple wires for measuring inner cryostat temperature. The fourth, located at 72.6 cm, 135.0°, has diameter 15.2 cm and services HFE. Finally the fifth, located at 75.0 cm, 165°, has diameter 7.1 cm and services vacuum pumps for the vacuum space.

Refrigerant and HFE pass through stainless steel feedthroughs electron beam welded onto copper elbows, which mate to the crown ports. The stainless portion of this assembly lies behind the lead wall, and so does not impact the background. The refrigerant feedthrough connects to a series of 1/2 inch copper tubes purchased at Metallica[120], which transport the refrigerant to the heat exchangers. Two 1 inch copper tubes, purchased from McMaster Carr[121], similarly carry HFE to ports on the inner cryostat.

42 thermocouples, supplied by Omega Engineering[122], are mounted at various positions on the surface of the inner cryostat. A feedthrough was created by potting the thermocouple leads into a hole in a copper flange. In this case the feed through flange remains at room temperature, relieving the need to accomodate differing CTEs and allowing a simpler design. Acrylic was not used to hold the epoxy during curing. Instead, a rubber dam was created, which did not bond to the epoxy and was removed after curing.

The hatch of the outer cryostat is shown in figure 5.9. Six 7.2 cm ports allow the passage of cables. The xenon inlet and outlet ports on inner cryostat hatch cable flanges are welded to 1/2 inch and 1 inch tubes, which pass through 7.6 cm xenon

Material	^{40}K [pg/g]	^{232}Th [pg/g]	^{238}U [pg/g]	Mass [g]
Crown bolts	<5.9	72±8	83±6	10272
Crown washers	<7.0	50±4	43±5	1440
1/2 inch tubing	<N/A	<2	<1.5	2463
1 inch tubing	<3.1	< 40±2	<1.5	2819
Simolex O-rings	111.1	<10000	<10000	449
Thermocouple wire	483±288	< 2930	< 1345	161
Outer cryostat copper	0.05	<0.8	<0.8	3.16×10^6

Table 5.2: Radioactive contamination of many outer cryostat components in pg/g. The first four items were measured by ICP-MS. The last was measured by direct counting.

Surface	^{232}Th [ng]	^{238}U [ng]
Outer, Outer cryostat	24	82
Inner, Outer cryostat	23-250	79-250
Outer, Inner cryostat	20-210	70-210
Inner, Inner cryostat	18-200	63-200
Total	85-684	294-742

Table 5.3: Surface contamination analysis of the inner and outer surfaces of the inner and outer cryostat. Contamination levels were assessed using a swipe test (see text). Contamination density of the outer surface of the outer cryostat is assumed as minimum value for the contamination density of the other surfaces.

inlet and outlet ports on the outer cryostat hatch. Finally, a third 7.6 cm port allows passage of the HV cable. The outer hatch cable flanges mate to the inside of the outer hatch. The other three ports mate to copper/stainless elbows similar to those described above. The outer cryostat hatch, crown, and all ports are sealed using silicone o-rings purchased from Simolex[123].

Radioactive contamination of the above components and the cryostat copper is shown in table 5.2. These components together contribute 14-171 $2\nu\beta\beta$ evt/yr 0.1-1.4 $0\nu\beta\beta$ evt/yr, corresponding to <0.4% and 0.2-4.6% of tolerance. The contribution of these components to $2\nu\beta\beta$ background is negligible.

Upon receipt, the outer surface of the outer cryostat was cleaned as described in section 3.5. The inner cryostat was then removed, and the inner surface of the outer

cryostat, and all surfaces of the inner cryostat were cleaned using only solvents (no acid etching was performed). Whatman[80] filter papers soaked in mild HNO_3 were then used to sample portions of the various surfaces. A contamination of 0.2 pg/cm^2 ^{232}Th and 0.7 pg/cm^2 ^{232}U was found on the outer surface of the outer cryostat. Contamination upper limits of 2 pg/cm^2 were set for the rest of the surfaces. The results of NAA of the filter papers are shown in table 5.3, scaled to the full surface area of each portion of the cryostat. This corresponds to <0.1 $0\nu\beta\beta$ events/year, or 0.1% - 0.4% of tolerance. Contribution to the $2\nu\beta\beta$ background is negligible.

The inner and outer vessels of the cryostat were constructed and electron beam welded at SDMS[124] in Grenoble, France. The copper was stored under a 10 m.w.e concrete overburden between machining and welding runs. Upon completion, the cryostat was shipped by surface to Stanford University, where it spent 1 year. It was then shipped to WIPP, as has been there for 2.5 years. For analysis of cosmogenic activation, the production sequence was conservatively simplified to:

1. 45 days at sea level
2. 1 year at 7 m.w.e
3. 1.5 days at sea level
4. 2.5 years of cooldown

Total cosmogenic contribution of the cryostat to yearly $0\nu\beta\beta$ background rate is negligible, based on the equations, production rates, and hit efficiencies given in section 3.7. Contribution to $2\nu\beta\beta$ background rate is 283 events/year, dominated almost entirely by ^{60}Co. This corresponds to 0.7% of tolerance.

5.3 Cryogenic System

The cryogenic system consists of three Polycold PFC-672HC[125] refrigerators, connected to refrigerant feedthroughs on the outer cryostat via vacuum insulated lines. The refrigerators are each capable of extracting 1500W from the inner cryostat. A

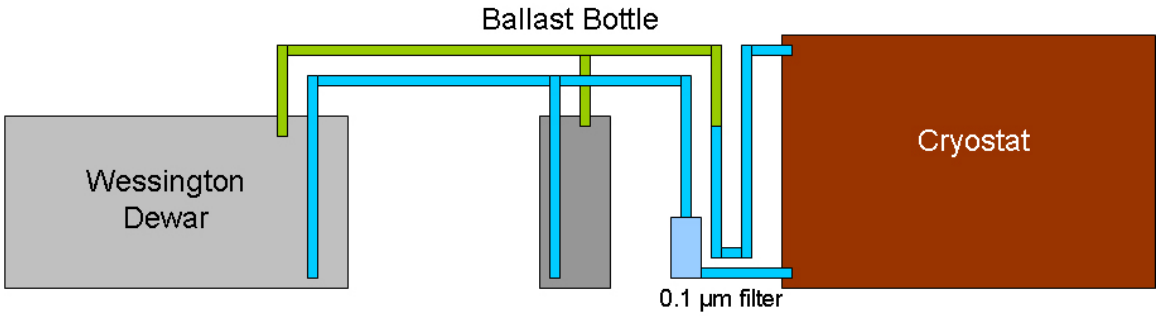

Figure 5.10: A schematic of the HFE system. Green indicates gas phase, blue indicates liquid phase.

chiller from BV Thermal Systems[126] services each refrigerator. Each refrigerator/chiller pair cools one inner cryostat heat exchanger, providing triple redundancy for the cryogenic system. A proprietary hydro-fluorocarbon/argon gas mixture is used as refrigerant. The radiopurity of this gas mixture has not yet been measured.

5.4 HFE System

A simplified schematic of the HFE system is shown in figure 5.10. When not in use, the HFE is stored in a custom cryogenic dewar, referred to here as the HFE dewar. The dewar has two spigots, one with a dip tube that reaches its bottom, and a second which accesses the vapor above the liquid. These tubes connect to the HFE inlet and outlet of the inner cryostat. Heaters mounted to a 100 liter ballast bottle, generally kept ∼50% full of HFE, are used to regulate the pressure in the inner cryostat by adjusting the vapor pressure of the HFE in the ballast bottle. Figure 5.11 shows the vapor pressure of HFE as a function of temperature. A 'U' in the gas phase tube connecting the HFE dewar and cryostat allows the HFE gas/liquid transition to occur at room temperature, which prevents warm liquid HFE in the ballast bottle from being cryogenically pumped into the cryostat. HFE is pneumatically pushed into and out of the cryostat, ballast bottle, and HFE dewar using 99.999% grade bottled N_2.

Relevant properties of HFE are listed in table 5.4. Of significant note is that HFE

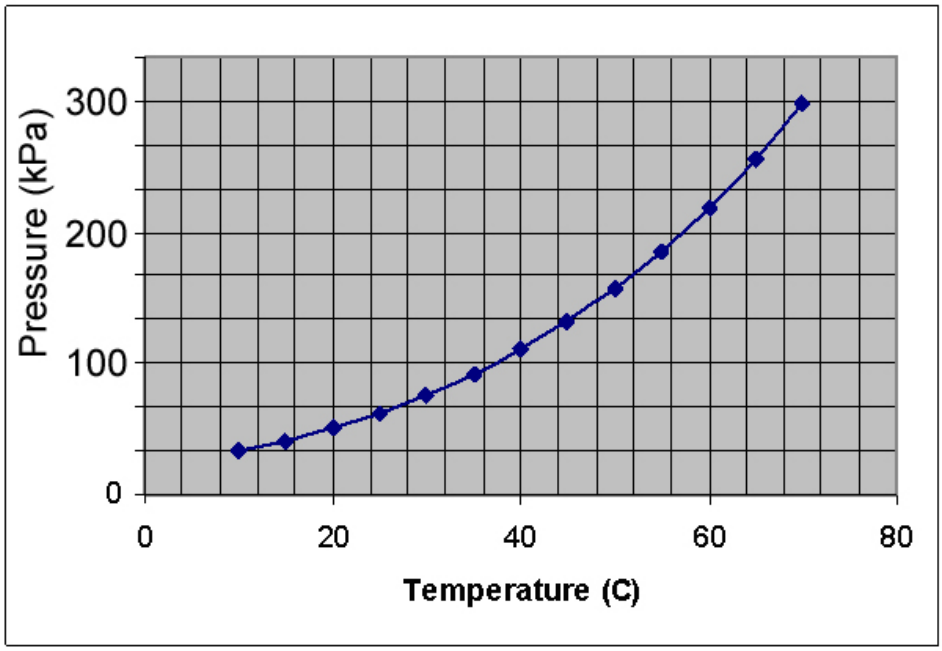

Figure 5.11: The vapor pressure of HFE as a function of temperature.

Property	Value
Molecular Weight	200 g/mol
Freeze point	150.65 K
Boiling point @ atm	307 K
Heat of Vaporization	142 J/g
Solubility of N_2	55 vol %
Density vs T	2.26 - T/347.2 g/cm^3
Specific heat vs T	382 + 3.08·T J/kg·K
Thermal conductivity vs T	0.13 - T/5102 W/m·K

Table 5.4: Relevant properties of HFE at 298K, unless otherwise noted.

Method	^{40}K [pg/g]	^{232}Th [pg/g]	^{238}U [pg/g]
Requirement	<0.077	<0.010	<0.010
NAA	<0.068	<3.7	<7.3
NAA w/ evaporation	<0.017	<0.015	<0.015

Table 5.5: Purity requirements, and two NAA measurements, for ^{40}K, ^{232}Th, and ^{238}U contamination of HFE. Values given in pg/g.

liquid density increases from 1.40 g/cm^3 at room temperature to 1.77 g/cm^3 at 170K. Thus 3050 room temperature liters (4270 kg) of HFE are required to fill the cryostat. An additional ∼100 liters (140 kg) fill the ballast bottle and HFE plumbing.

The radiopurity requirements for HFE are extreme because of its large mass and proximity to the TPC. Table 5.5 lists the purity requirements for ^{40}K, ^{232}Th, and ^{238}U, along with two NAA measurement methods. The first is standard NAA, which does not provide the sensitivity required to qualify the material. In the second method, 1018.8g of HFE was evaporated, leaving 5.3 mg of residue. NAA was then performed on this residue. In order to estimate the retention coefficient for ^{40}K, ^{232}Th, and ^{238}U in the evaporation process, ^{220}Rn was bubbled through a separate sample of HFE, loading it with radioactive ^{212}Pb. Direct counting before and after evaporation of this sample revealed a retention coefficient of 20%. This value is assumed for retention of ^{40}K, ^{232}Th, and ^{238}U. This evaporation NAA method increased sensitivity to ^{232}Th, and ^{238}U to 0.015 pg/g. The results make HFE the cleanest material found by the EXO collaboration, making it particularly suitable for its task.

In addition to the standard contaminants, ^{210}Pb and ^{85}Kr contamination was considered. ^{210}Pb can be introduced into the HFE via ^{222}Rn in dissolved air. According to 3M, the HFE was saturated with air during manufacturing (at 55% by volume). Conservatively assuming that the radon level in this air was 150 mBq/l (the EPA recommended action limit for radon contamination), the HFE was loaded with 215 Bq of ^{222}Rn, which decayed to 100 mBq of ^{210}Pb. The $2\nu\beta\beta$ hit efficiency of ^{210}Pb attached to the outside of the LXe vessel was calculated by Monte Carlo to be 1.7×10^{-5}events/decay (impact on $0\nu\beta\beta$ levels was calculated to be negligible). This hit efficiency is obviously very conservative, given that one would expect most of the

Source	$2\nu\beta\beta$ [evt/yr]	$0\nu\beta\beta$ [evt/yr]
Intrinsic K, Th, U	<1254	< 2.4
^{210}Pb	<107	0
^{85}Kr	250	0
Dewar K, Th, U	<2657	<15.0
Total	250-4268	< 17.4

Table 5.6: Background impact of HFE, broken down into various sources, in events/year.

^{210}Pb to precipitate onto the much larger surface of the inner cryostat. We assume here that through handling of the HFE once received, we have re-saturated the HFE with fresh air no more than once.

^{85}Kr ($T_{1/2} = 10.8$ yr) a weak gamma line at 514 keV (0.43% B.R.) and bremsstrahlung radiation due to a 687 keV β (99.5% B.R.) can contribute to the $2\nu\beta\beta$ background. Assuming an atmospheric concentration of 1 mBq/l[127] at the time and place of HFE production, the HFE is loaded with 1.2 Bq of ^{85}Kr. The $2\nu\beta\beta$ hit efficiency of ^{85}Kr in the HFE was calculated by Monte Carlo to be 6.6×10^{-6} events/decay.

Finally, although the HFE dewar walls were degreased and etched using solutions of phosphoric, hydrofluoric, and nitric acid during assembly, trace contaminants left behind could dissolve in the HFE and contaminate it. To test this, 5632g of HFE were introduced into the dewar. The dewar was then tilted back and forth, allowing the HFE to sample an estimated 4.5% of the inner wall of the container. This HFE was then extracted and analyzed by NAA. Scaling the results to the full mass of HFE and full inner surface of the dewar, contamination limits of <0.006 pg/g ^{40}K, <0.083 pg/g ^{232}Th, and <0.099 pg/g ^{238}U are predicted.

A background impact analysis of each of the discussed HFE contamination sources is shown in table 5.6. The total impact to background is 0.6% - 10.7% of $2\nu\beta\beta$, and <58.0% of $0\nu\beta\beta$ tolerance. This upper limit is dominated by the poor sensitivity measurement of the contamination introduced by the walls of the HFE dewar.

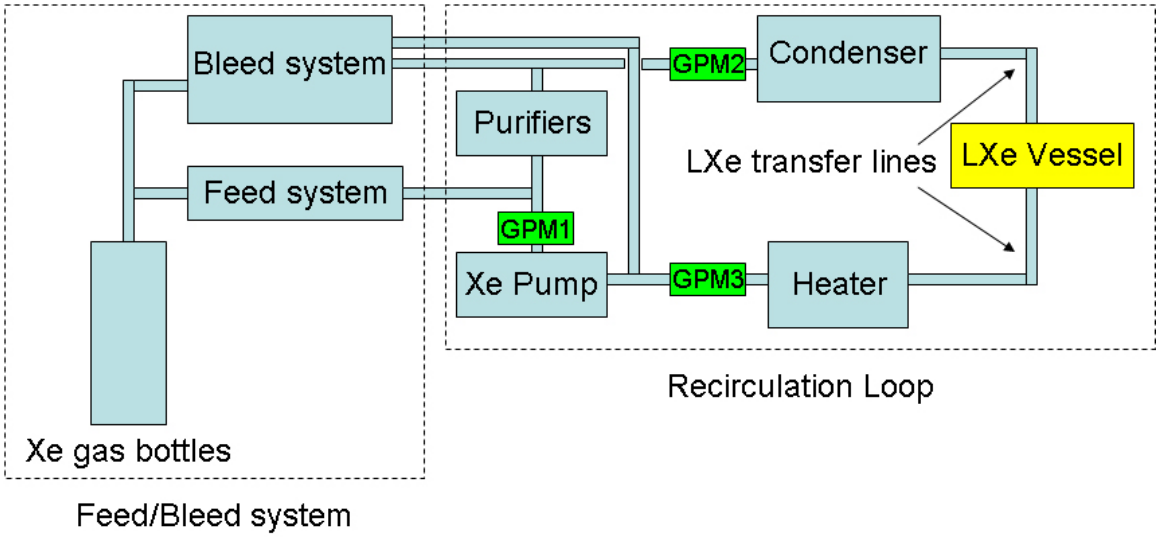

Figure 5.12: A schematic of the xenon system.

5.5 Xenon System

A simplified schematic of the xenon system is shown in figure 5.12. The xenon system has two primary functions:

1. The transfer of xenon from gas bottles to the LXe vessel and back, including continuous, precise regulation of the LXe vessel pressure in order to maintain a pressure difference across the walls of the TPC of less than 34.5 kPa.

2. Purification of the LXe. The nominal gas phase purification rate for the xenon system was arbitrarily chosen to be 20 SLPM.

Xenon is moved from gas bottles to the LXe vessel via the feed system. The feed system consists of two identical redundant paths. A regulator reduces the xenon pressure from ∼800 psia to ∼30 psia. A computer controlled block valve and proportional valve in series then regulates the flow of xenon into the recirculation path. The pressure rating of the block valve exceeds 1000 psia, allowing it to hold off bottle pressure in case of catastrophic regulator failure.

Xenon is moved from the vessel back to gas bottles by the bleed system. The central component of the bleed system is a pair of redundant two-stage compressors,

each with a compressing rate of 53 l/m at $>$ 1500 torr input (the flow rate drops to $\sim$10 l/m at 750 torr input, and zero at 600 torr input). The compressors are connected to a 50 l buffer volume, which is maintained using a pressure switch at $\sim$650 torr. This buffer volume is separated from the LXe vessel by a pair of parallel proportional valves followed by a pair of parallel block valves, which tap the circulation path before the xenon pump and after the purifiers.

The feed system and bleed system (together referred to as the feed/bleed system) are used both to fill and empty the xenon vessel, and to continuously regulate its pressure, matching it to the pressure of the HFE in order to minimize stress in the thin copper walls.

As described in section 2.3, electron capture due to chemical impurities in the LXe results in attenuation of the ionization signal. Thus, removal of impurities contaminating the xenon, and minimizing the source of these impurities, are driving concerns for the xenon system. There are several sources of impurities in the xenon. First, impurities are inherent in the bottled xenon at the ppm level. Second, the construction of the high pressure portion of the system is not compliant with ultra-high-vacuum practices (for example many of the fittings in each are Swagelok). Sub-optimal cleanliness, as well as outgassing of the internal components, is problematic. Finally, all components in the xenon system, including the plumbing itself, outgases impurities at some level. Of particular concern is the high diffusion rate and solubility of chemical impurities in the large amount of Teflon, acrylic, and kapton present in the TPC (submersed directly in the LXe).

In steady state operation of the xenon system, the pressure in the LXe vessel is stable to within $\sim$10 torr, allowing the block valves of the feed/bleed system to remain closed almost indefinitely. This essentially eliminates the first two sources of impurities described above. The feed system taps into the circulation loop immediately before a redundant pair of Saes PS4MT3R1 purifiers, so that on the rare occasions that the feed system is activated during steady state operation, the added gas is immediately purified. This placement is also advantageous in cleansing impurities during initial fill of the vessel.

The redundant pair of Saes purifiers is also used to remove impurities continuously introduced via outgassing of all parts of the xenon system. In order to achieve an attenuation of $< 1\%$ over the TPC drift distance of 19.2 cm, impurities of < 40 ppt O_2 equivalent are required in the LXe, based on the information in section 2.3. At the nominal recirculation rate of 20 SLPM, the xenon volume can be turned over once in 1.15 days, requiring that the contamination rate due to outgassing be < 35 ppt O_2 equivalent/day, or 5×10^{-8} mol O_2 equivalent/day. In order to reduce the effects of outgassing of plastics in the TPC, all plastic parts were dry N_2 baked prior to insertion. In addition, the TPC was kept under dry N_2 purge throughout assembly. Replacing O_2 and H_2O in the plastics with N_2 in this way should reduce outgassing effects by a factor of 1×10^2 - 1×10^4, depending on the electron attachment rate of N_2 compared to O_2. A quantitative estimate of the total contamination rate of the xenon system has not yet been performed.

The purity of the xenon is measured by three Gas Purity Monitors (GPMs). The GPMs consist of a tungsten filament and an anode. The tungsten filament is heated, and the resultant electrons are captured by the anode. Impurities in the gaseous xenon absorb electrons in much the same way they do in the liquid phase. In this way, the current read by the anode is positivly correlated with the purity of the gas. The GPMs are placed immediately before and after the purifiers, and immediately before the Xe pump. This allows the efficiency of the purifiers and the outgassing of the chamber to be determined and tracked.

A xenon condenser (see figure 5.13) liquefies xenon added to or circulated around the xenon system. The condenser is composed of 6.6 m of 3/8 inch copper tubing wound around the upper half of a copper block. A second coil, wound around the lower half of the copper block carries refrigerant supplied by a Polycold refrigerator, provides 600 W of cooling power. A heater placed in between the coils is used to regulate the temperature of the upper half of the block. 10 thermocouples measure the temperature in various places on the copper block and coils. Heat leaks in the condenser consume 250 W of cooling power, leaving 350 W for condensing, corresponding to a maximum condensing rate of 38 SLPM.

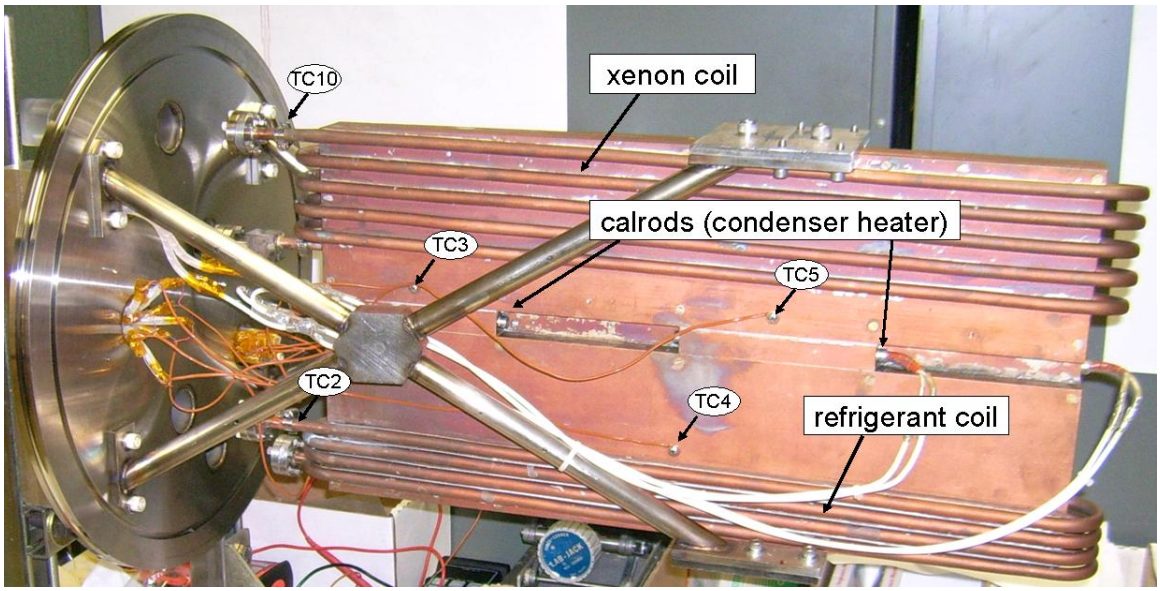

Figure 5.13: The LXe condenser.

Upon exiting the condenser, LXe enters a vacuum insulated line, which transfers the liquid from the condenser down to the xenon input feedthrough on the cryostat. During steady state operation, the LXe vessel is completely filled, and the transfer line itself remains partly full of LXe.

The xenon output feedthrough on the cryostat also connects to a transfer line. This line connects to the LXe heater, which provides the energy required to boil LXe during recirculation or recovery of the xenon. The heater consists of a heating element buried inside a copper cylinder. LXe travels through the cylinder, absorbing heat added to it.

Finally, a gas phase xenon pump circulates xenon around the circulation loop (see figure 5.14). The pump body is a honed stainless steel cylinder. A magnet embedded inside a stainless steel piston couples to a ring magnet outside of the stainless cylinder, which drives the piston back and forth. The piston makes a dynamic seal to the walls of the cylinder using accurately machined sealing rings made from ultra-high-molecular-weight polyethylene (UHMWPE). No lubricants are used. Reed valves in either end of the honed cylinder allow xenon into and out of the pump. Since Xe gas is present on either side of the Teflon piston, any leakage around the piston poses no

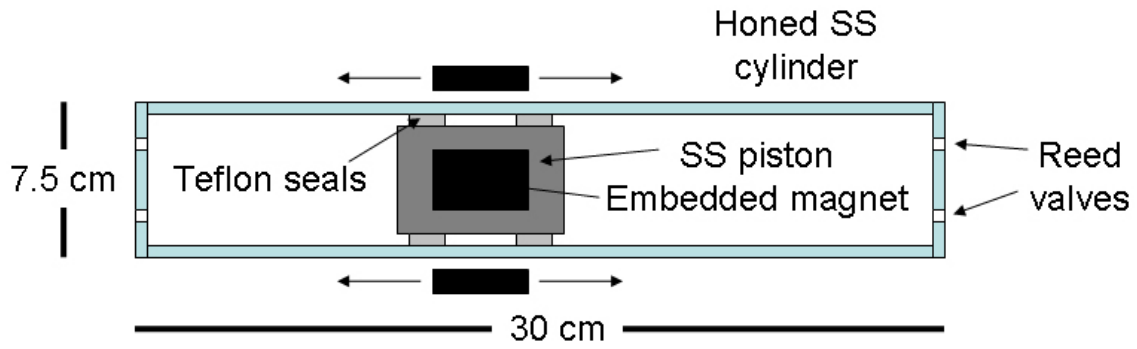

Figure 5.14: A schematic of the xenon recirculation pump.

Source	^{222}Rn atoms/day
SAES Purifiers	<110
Valve Seats	<20
Xe system plumbing	90±25
Xe system filters	50±10
Total	<270

Table 5.7: Major contributors to radon emanation in the xenon system.

contamination issue, and only reduces efficiency of the pump. Maximum pumping rate of this pump is 60 SLPM. A maximum pressure gradient of 650 torr can be created before the ring magnet decouples from the piston. Particulate generated by the friction between the seals and the honed stainless steel cylinder is captured by two filters, located immediately before and after the SAES purifiers.

As discussed in section 3.2, radon emanation is a concern for the xenon plumbing. The major radon contributors are shown in table 5.7. Since there is little that can be done about ^{222}Rn emanated from within the TPC components themselves (see section 4.6), a ^{222}Rn trap with $> 99.99\%$ efficiency is being developed which would effectively eliminate ^{222}Rn ingress from outside the TPC. Such a trap would be located just prior to the condenser, and would function by routing gaseous Xe through a mesh of metal cooled at a temperature such that the difference in vapor pressure between Rn and Xe results in preferential trapping of ^{222}Rn. The trapping time is designed to be longer than the ^{222}Rn decay time (3.8 days), insuring that the ^{222}Rn decays in the trap. As

Material	^{40}K [pg/g]	^{232}Th [pg/g]	^{238}U [pg/g]	mass[g]
Lead	<1.8	<10	<10	5.94×10^7
Coating	83±30	<134	804±300	300

Table 5.8: Radioactive contamination in the lead shielding.

of this writing, this trap has not been installed.

5.6 Lead Shielding, VETO and Underground Installation

The detector thus far described is located inside a class-100 cleanroom at the Waste Isolation Pilot Plant, a salt mine near Carlsbad NM. It is buried 2150 ft (1700 m.w.e) under ground. This environment provides lower backgrounds when compared to more ordinary locations. The most significant primordial radioactivity contamination is located in the salt walls. Two other backgrounds were described in section 3.2: atmospheric ^{222}Rn, and cosmic ray muons and their spallation products.

Direct counting of salt samples showed an average contamination of 124±2, 66±11, and 27±3 g/ng of ^{40}K, ^{232}Th, ^{238}U in the salt surrounding EXO-200. A 25cm thick lead shield surrounds the EXO-200 detector (see figure 3.3) and protects it from this radioactivity and any other external radioactivity. Penetrations in the front lead wall allow passage of the many cryostat feedthrus described above. A second lead wall, located 10cm from the first, eliminates direct line of sight openings, preventing radiation from entering the detector. Given this geometry, a Monte Carlo simulation predicts a negligible 5 $2\nu\beta\beta$ evt/yr contribution to the $2\nu\beta\beta$ background due to radioactive contaminants in the salt, and <1 evt/yr contribution to the $0\nu\beta\beta$ background.

The lead for EXO-200 was purchased from Doe Run Co[128] and cast by JL Goslar[129]. The shield was cast as many interlocking bricks. Gaps between bricks measured <1 mm, with no direct line of sight through the shield once both front walls are installed. A 10 μm epoxy coating encapsulates each brick. Since the shield itself

is also a source of radiation, the lead was selected for low activity. Measured contamination levels and total mass for the lead shielding and coating are shown in table 5.8. The total contribution to the backgrounds expected from the primordial nuclides in the lead shielding (with negligible contribution from the coating) is <503 $2\nu\beta\beta$ and <3.8 $0\nu\beta\beta$ evt/yr, corresponding to <1.3% and <12.6% of tolerance respectively.

^{210}Pb contamination of the lead shielding was measured to be 25±5 mBq/g. The $2\nu\beta\beta$ hit efficiency for the lead shielding (not including negligible contribution from the outer lead wall) was found to be 3.18×10^{-11} evt/decay. Thus, the predicted contribution to $2\nu\beta\beta$ background is 1273±255 $2\nu\beta\beta$ evt/yr, corresponding 3.2±0.6% of tolerance.

Since gaps exist in lead shielding, atmospheric ^{222}Rn can enter the small space between the lead shielding and cryostat and decay. In order to assess the severity of this problem, EXO-200 measured the Rn activity in the air at WIPP and found a concentration of 14.8±1.6 mBq/l. The surface area of the cryostat is 1.41×10^{5} cm^2. The hit efficiency for these decays is predicted by Monte Carlo to be 2.0×10^{-5} $2\nu\beta\beta$ evt/yr, and 9.0×10^{-8} $0\nu\beta\beta$ evt/yr. With this information, one can calculate the ^{222}Rn background per mm of air gap between the lead shield and cryostat to be 130 $2\nu\beta\beta$ evt/(yr·mm) and 0.6 $0\nu\beta\beta$ evt/(yr·mm), corresponding to 0.3%/mm and 2.0%/mm of tolerance respectively.

The thickness of the air gap is not known with great accuracy, and is expected to be between 1 mm and 3 mm thick. Should background from ^{222}Rn prove to be significant, a solution to mitigate the problem has been proposed and involves erecting a hermetic enclosure outside the lead shielding purged with air that was stored a sufficiently long time to eliminate its ^{222}Rn content. Small diameter air tubes were installed between the lead shield and cryostat to purge the air gap in the event such a system is required.

Although the cosmic ray muon flux at WIPP is highly suppressed (it was measured to be 3.1×10^{-7} s^{-1}·cm^{-2}·sr^{-1}[76]), it can still cause significant background. A Monte Carlo study was performed in which muons of a particular energy, with a ratio of μ^+/μ^- of 1.25, were generated over an area of 1024 m^2, 4 m above the LXe vessel. The muon momenta had a $cos^2(\theta)$ angular distribution and were isotropic in ϕ. The

energies simulated ranged from 10 to 600 GeV.

The study found that >99% of the background contribution came from muons following a path that passed within 100 cm of the detector. It also found that after rejecting events producing more than one ionization site, >99.9% of the background contribution came from muon spallation products, with <0.1% of the background coming from muons themselves entering the TPC. In conclusion, the study found that the total contribution to the background would be 15±1 $0\nu\beta\beta$ evt/yr, and 1106±8 $2\nu\beta\beta$ evt/yr.

To mitigate this problem, an active veto system was installed. It consists of 30 plastic scintillator panels, approximately 350cmm×65cm×5cm each read out by 8 photo multiplier tubes (PMTs). The muon detection efficiency of each panel at operating threshold was experimentally determined to be 97.6%. The location of the panels with respect to the cleanroom and lead shield is shown in red in figure 5.15, and provides angular coverage of 97%. Thus the total efficiency of the veto system is predicted to be 94.7%, reducing the cosmic ray backgrounds contribution to 59±1 $2\nu\beta\beta$ evt/yr and 0.8±0.1 $0\nu\beta\beta$, corresponding to 0.15% and 2.7±0.2% of tolerance respectively.

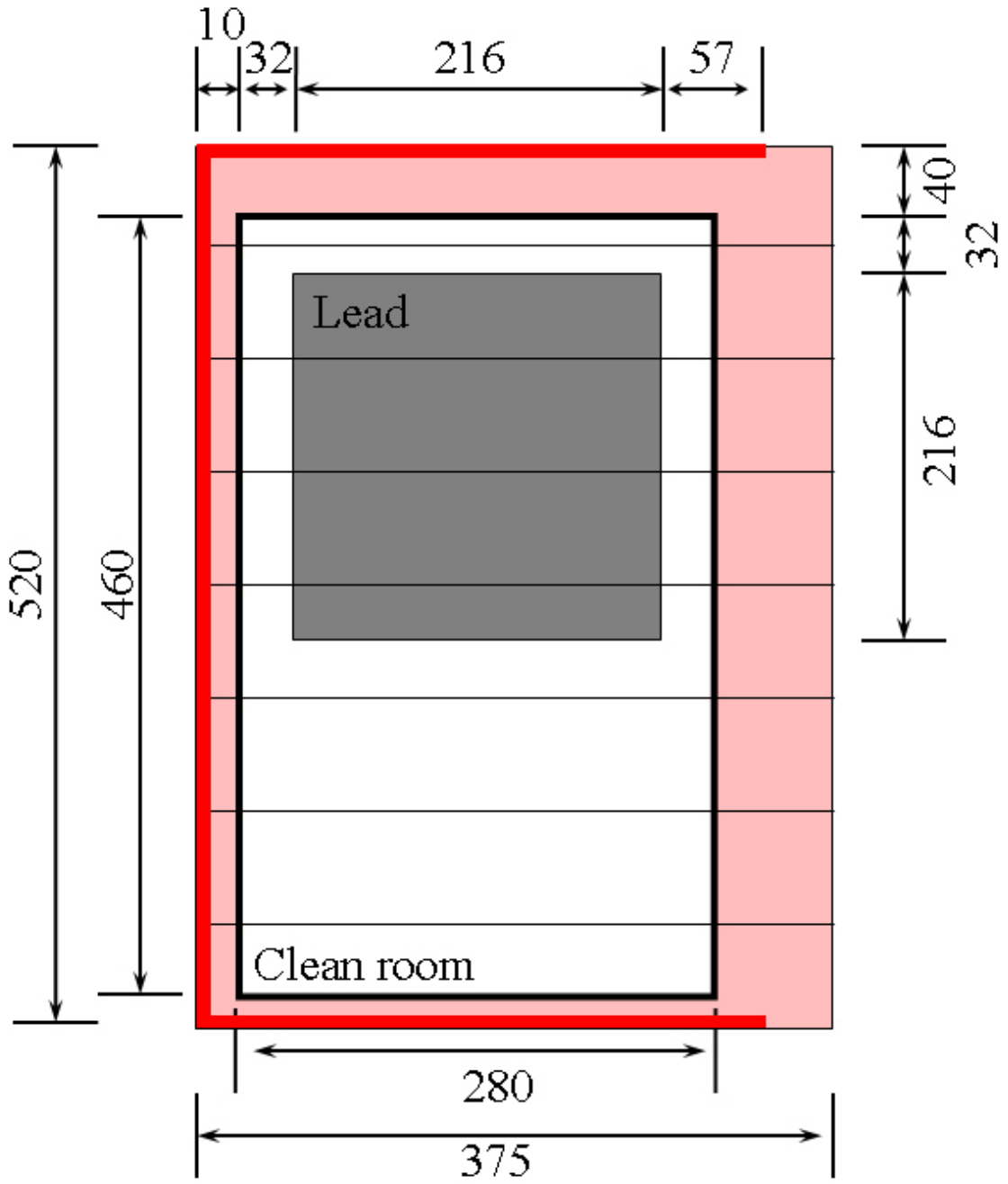

Figure 5.15: A schematic of the VETO panels, shown in red.

Chapter 6

Electronics and Calibration

6.1 Electronics

A schematic of the EXO-200 electronics is shown in figure 6.1. 18 Front End Cards (referred to here as FECs) continuously digitize ionization and scintillation signals carried by the cables and transmit the data to the Trigger Event Module (referred to here as the TEM). The TEM generates events based on user controlled trigger settings, and transmits these events to the control PC for storage and analysis. A distribution board accepts commands and clock signals from the TEM and distributes them as appropriate to the FECs.

Three of the 18 FECs service each of the collection wire, induction wire, and APD cables on each chamber half. There are total of 76 collection wire and induction wire channels, and 74 APD channels, with each FEC servicing 12 or 13 channels. The FECs are housed in two copper chassis located just outside of the first lead wall (see figure 3.3). Each chassis contains FECs for one chamber half. Copper conduits carry cables from the outer cryostat hatch cable flanges to the chassis, and shield the cables from electromagnetic interference.

A schematic of an FEC is shown in figure 6.2. Each signal first enters one input of a charge amplifier. In the case of ionization wire channels, the second charge amplifier input is connected to the cable guard traces. APD cables do not have guard traces, so the second charge amplifier is connected to ground in this case. Capacitors are

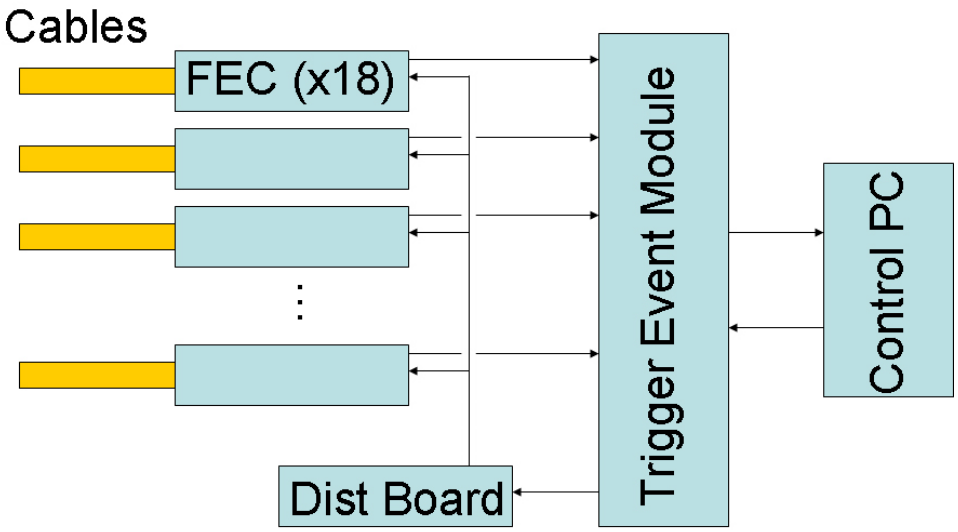

Figure 6.1: Schematic of the EXO-200 electronics.

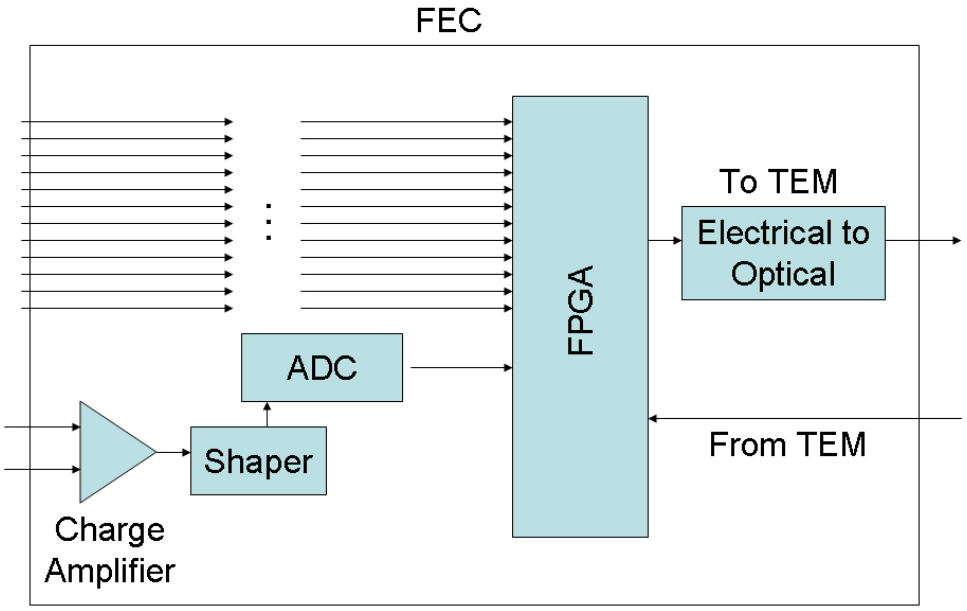

Figure 6.2: Schematic of a Front End Card.

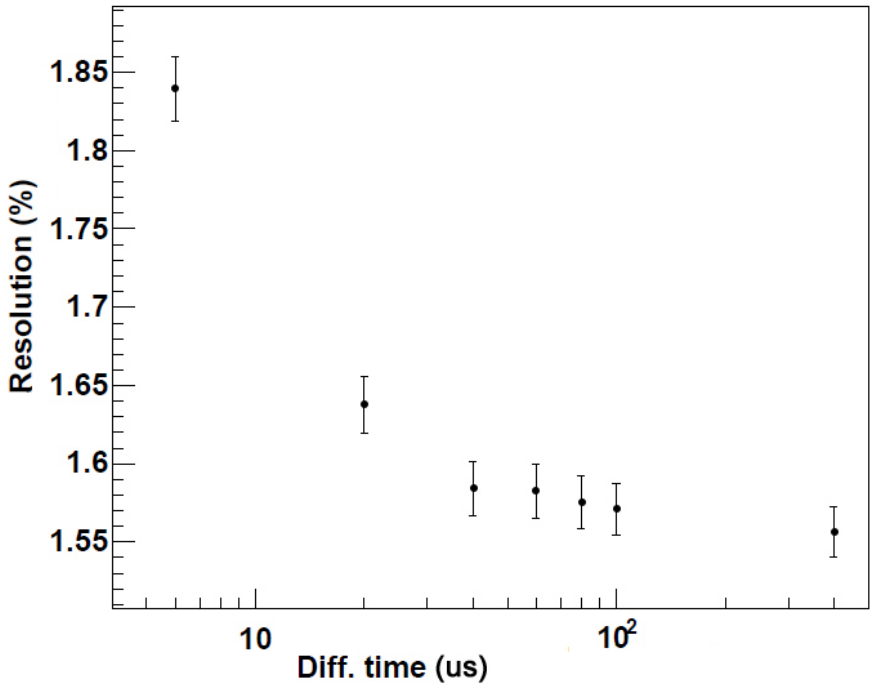

Figure 6.3: Actual detector resolution for ionization alone as a function of first differentiation time, assuming 1.5% intrinsic LXe energy resolution and 800 electrons of noise contributed by electronics (see text below).

used to decouple the FECs from the high DC potential of the induction wires and APDs, as illustrated in figure 4.16.

Upon exiting the charge amplifier, each signal is then passed through a shaper. The shaper consists of an integrating circuit with shaping time 2 μs, and three differentiating circuits. The latter of the two differentiating circuits have shaping times of 2 ms and 1 s. Monte Carlo studies of shaping times between 6 and 400 μs for the first differentiating circuit show that energy resolution obtained after fitting improves with increasing differentiation time, as shown for collection wires in figure 6.3. This is occurs for two reasons. Firstly, an increased differentiation time increases the time span, and hence number of samples, in the signal available for fitting, thus improving statistics of the fit. Secondly, a longer pulse is less sensitive to variations in the time distribution of charge collection due to differences in event topology and electron drift

trajectories. On the other hand, shorter differentiation times improve the response to low-frequency microphonic induced noise and reduce the chance of signal pile-up, although the magnitude of these effects is difficult to predict.

Following each shaper is a 12-bit, 1 MHz analog to digital converter (ADC). The 12 - 13 now digital signals are then all passed to a single field-programmable gate array (FPGA), which assembles each μs digital samples into a string of 16 2-byte words. This digital data is then passed to the TEM via fiber optic cable.

Based on trigger conditions and algorithms, the TEM assembles the continuous stream of digital data provided by the 18 FECs into events of up to 2048 samples (corresponding at 2.048 ms at the FEC ADC sampling rate of 1 MHz). Each sample contains 16 2-byte words for each of the 18 cards, as well as information used to identify the event.

The TEM sends data to the control PC using a National Instruments PCI-6534 digital board[130] (a second identical board is used to send commands from the control PC to the TEM). This board has a maximum transfer rate of 80 MB/s, corresponding to an event rate of 67.8 Hz at 2048 samples/event.

The signal-to-ground capacitance of the collection wire channels and induction wire channels were measured to be 30$\pm$2 pF and 37$\pm$3 pF, respectively. The capacitance for APD channels has not yet been measured at cryogenic temperatures and with the APD bias on, though is expected to be $\sim$875 pF based on studies of individual APDs.

Prior to installation, the inputs of the ionization channel (APD) boards were loaded with 200 pF (1 nF) capacitors in order to estimate the total electronic noise. The ionization channel boards measured 850$\pm$150 electrons, and the APD channel boards measured 1650$\pm$200 electrons, where the errors represent the range of values measured.

This noise can be compared to the experimental energy resolution, represented in electrons. A $0\nu\beta\beta$ event, depositing 2.458 MeV into the LXe volume, will produce 1.58×10^5 electrons and 1.37×10^5 photons based on the W-values listed in tables 2.4 and 2.5. Based on initial EXO studies[20], EXO-200 is expected to achieve an ionization energy resolution at this energy of 1.8% (σ/E), and a scintillation energy

Source	Weak Strength [kBq]	Strong Strength [kBq]	Lines [keV]
^{60}Co	0.5	7.2	1173, 1333
^{137}Cs	3.0	14.8	662
^{208}Tl	1.5	38.4	2615

Table 6.1: The six calibration sources (two strengths for each of three isotopes) used for calibration of the detector. Relevant gamma lines are listed as well.

resolution at this energy of 4.0% (σ/E). For the ionization channels, this corresponds to ∼2800 electrons. 850 electrons represents a 4.5% effect on this energy resolution. This is verified in figure 6.3 in the limit that the first differentiation time becomes long, allowing very accurate measurement of pulse height.

The scintillation channel collects only about 10% of the light, but has a gain of 100. In addition, the signal is spread over all 74 channels, introducing a factor of $1/\sqrt{74}$ assuming the noise in all the channels add in quadrature. Thus, the APD energy resolution is calculated to be 6400 electrons/channel. 1650 electrons represents a 3.3% effect on this energy resolution.

6.2 Detector Calibration

The response of the TPC to ionizing events of a given energy is dependent on the position of that event in the detector for a variety of reasons, including drift field non-uniformity, reflections of scintillation light throughout the TPC, channel to channel differences in signal response, etc. For these reasons an energy scale calibration procedure for the detector has been developed and is described here.

The calibration procedure involves measuring the detector response to three radioactive sources (listed in table 6.1) placed very near the TPC. Two strengths of each of the sources were purchased. These sources produce a broad spectrum of gamma interactions in the TPC. Of interest in calibration are those interactions which lie in a 'photoelectric peak'. These are gammas emitted by the radioactive source which do not interact with any matter prior to producing a single site event in the LXe (see figure 6.4 for an example). These events are useful for calibration because the energy

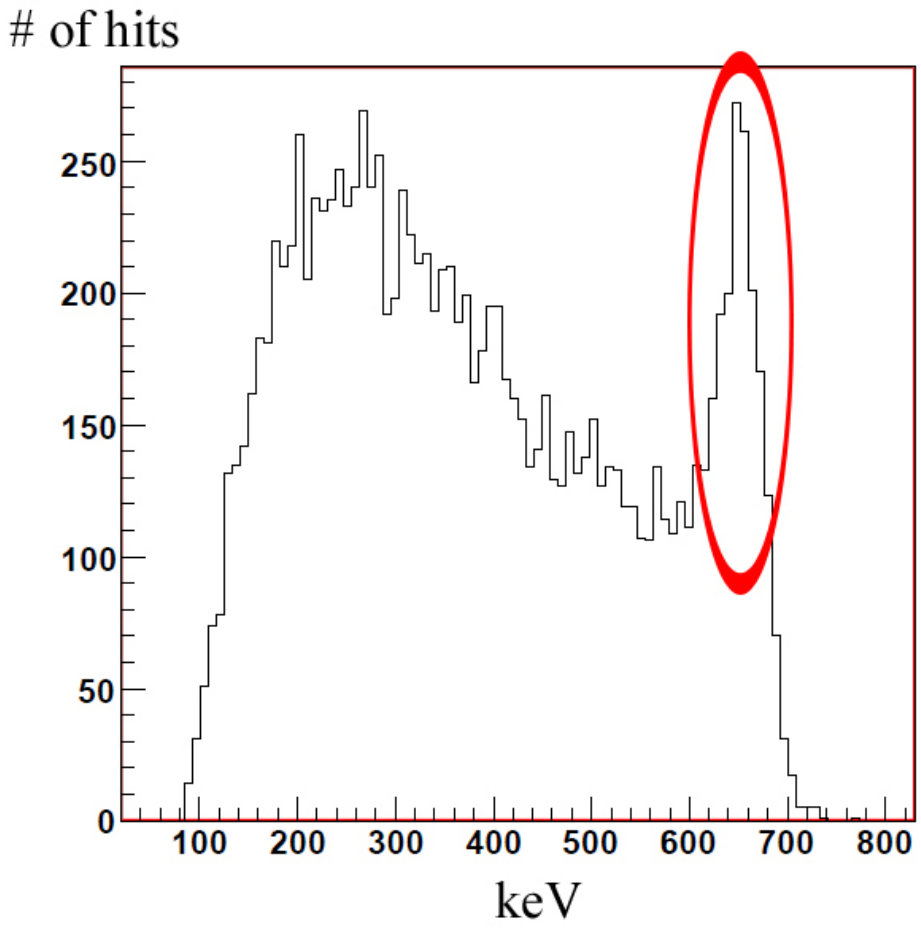

Figure 6.4: Monte Carlo simulation of the response produced by a ^{137}Cs source. The photoelectric peak is circled in red.

Figure 6.5: A calibration source is crimped to a stainless steel cable, strung with Teflon beads to reduce friction within the calibration tube.

of the event is exactly the well known energy of the gamma line. The strengths of the weak sources were chosen to produce a total event rate of ∼80 Hz in the detector. The strengths of the strong sources were chosen to produce an event rate of ∼80 Hz in the photoelectric peaks of each source throughout the detector. The event rate of ∼80 Hz was chosen in each case to roughly match the maximum throughput of the data acquisition system.

In analyzing the calibration data the TPC is divided into 296 subvolumes. The subvolumes are created by dividing the TPC into 37 hexagonal columns, each aligned with a gang of 7 APDs. The TPC is then divided into 8 slices along its length. The volume of each subvolume is 120 cm^3. The responses to each of the calibration source photoelectric peaks are determined to better than 0.1% in each subvolume.

The radioactive sources are welded into stainless steel capsules measuring 16.5 mm in length and 2.3 mm in diameter. The capsules are crimped to a 0.97 mm stainless steel cable. 3.2 mm teflon beads are strung along the cable to reduce friction within the calibration tube (see figure 6.5). The beads are separated by 5.8 mm long 1.6 mm diameter stainless steel tubes.

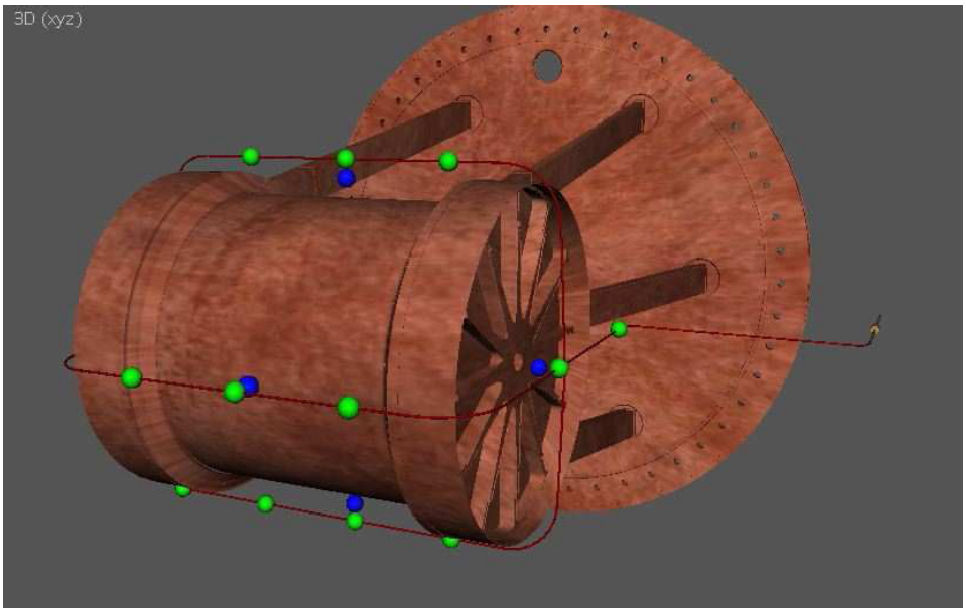

Figure 6.6: The calibration tube, through which calibration sources are fed. Green points indicate source positions investigated by Monte Carlo. Blue points indicate chosen calibration positions.

The sources are fed into a 3/8 inch copper tube, which passes as previously described through feedthrougs in the inner and outer cryostat vessels (see figure 6.6). The copper tube is supported by 1 mm copper wire, bolted to the top of the inner cryostat. 19 calibration points were investigated by Monte Carlo, 5 of which were ultimately chosen: One at the center of each end cap, and three around the barrel, midway between the end caps. Table 6.2 shows the minimum number of photoelectric peak events required in each subvolume to achieve better than 0.1% accuracy in response assuming 1.5% energy resolution at 2.458 MeV and that energy resolution scales as $1/\sqrt{E}$. It also shows the amount of time needed to acquire these events for each source.

The calibration tubing and copper wire (the only components of the calibration system permanently installed in the detector), were purchased from Metallica[120]. Table 6.3 shows the background contamination of these materials, measured by direct counting. The total contributions to the $2\nu\beta\beta$ and $0\nu\beta\beta$ backgrounds are shown in table 6.4.

Source	Position	# of req. events	Time required [min]
^{60}Co	Endcap	415	211
^{137}Cs	Endcap	835	206
^{228}Th	Endcap	211	357
^{60}Co	Barrel	415	281
^{137}Cs	Barrel	835	485
^{228}Th	Barrel	211	110

Table 6.2: The minimum number of photopeak events required to achieve 0.1% energy accuracy in each detector subvolume is listed. The worst case exposure times needed to acquire these events using the weak sources are also shown. Times for the strong sources scale as the intensity of the source, given in table 6.1

Material	^{40}K [pg/g]	^{232}Th [pg/g]	^{238}U [pg/g]	mass[g]
Tubing	<64	8.2±1.5	7.3±2	500
Wire	<304	45.2±3.2	10.9±3.4	144.2

Table 6.3: The minimum number of photopeak events required to achieve 0.1% energy accuracy in each detector subvolume is listed. The worst case exposure times needed to aquire these events using the weak sources are also shown. Times for the strong sources scale as the intensity of the source, given in table 6.1

Material	$2\nu\beta\beta$ [evt/yr (%)]	$0\nu\beta\beta$ [evt/yr (%)]
Tubing	<4509 (11.3)	0.20 - 0.44 (0.6 - 1.4)
Wire	<6184 (15.5)	0.23 - 0.35 (0.8 - 1.2)

Table 6.4: Background contributions of the calibration tubing and wire.

Chapter 7

Expected Sensitivity of EXO-200 to $T_{1/2}^{0\nu\beta\beta}$

As stated in section 3.3, the $T_{1/2}^{0\nu\beta\beta}$ sensitivity can be expressed as

$$T_{1/2}^{0\nu\beta\beta} = (2.5 \times 10^{26}/mol) \left[\frac{a\epsilon}{A}\right] \left[\frac{MT}{b\Delta E}\right]^{1/2} \tag{7.1}$$

EXO-200 uses Xe enriched to 80.6% ($a = 0.806$) in ^{136}Xe ($A = 135.9$). A mass M = 114.7 kg lies within the active volume of the detector. In determining $T_{1/2}^{0\nu\beta\beta}$ sensitivity, the remaining parameters are ΔE, ϵ, b, and T.

The energy resolution of the detector (which is proportional to the energy window ΔE) depends on many factors. First is the strength of the drift field. As shown in figure 2.3, detector energy resolution increases with increasing drift field strength. EXO-200 is capable of generating a maximum drift field of 3.7 kV/cm, which we assume here will be the operating value.

Second is energy resolution of ionization and scintillation individually, each of which depend on respective collection efficiencies. For events which interact at least 0.8 cm from the field shaping rings (0.55 cm from the Teflon reflector tiles), it is predicted that 100% of ionization electrons which do not recombine are collected. This defines the fiducial volume of the detector, at a radius of 17.8 cm. The inner

radius of the LXe vessel is 19.8 cm, thus providing 2 cm of inactive LXe shielding around the barrel (3 cm of inactive LXe shielding lie beyond each induction plane). Together with the 38.4 cm drift length, this defines the fiducial volume of the detector, which totals 114.7 kg. Based on prior LXe research by the EXO collaboration and others[20, 52], and the assumptions about energy resolution scaling given in section 2.7, we expect a noise subtracted ionization energy resolution of 1.8% (σ/E) at the $0\nu\beta\beta$ Q-value of 2.458 MeV.

The energy resolution expected from scintillation alone is difficult to predict, since light collection efficiency is far less than 100%. Detailed Monte Carlo simulation, including reflectivity estimates of all major detector components, predicts a light collection efficiency which varies almost linearly from 10% for events near the cathode to 14% for events near either anode. A light collection efficiency of 3% was found by the EXO collaboration[20] to produce a resolution of 8.3% at 570 keV, corresponding to 4.0% at 2.458 MeV. This is taken as a lower limit on the noise subtracted scintillation energy resolution expected in EXO-200.

Thirdly, electronic noise will degrade detector energy resolution. We expect to find 850 electrons of noise on the ionization channels, and 1650 electrons of noise on the APD channels. Electronic noise is expected to have a 4.5% and 3.3% effect on the energy resolution of ionization and scintillation detection, assuming the intrinsic values of energy resolution mentioned above and a long differentiation time is chosen in the hardware as discussed on section 6.1. Other factors, such as microphonic noise, are difficult to predict and could potentially have a significant effect on energy resolution.

Finally, the physics of scintillation-ionization anti-correlation plays a role, and is not yet completely understood. Work by the EXO Collaboration[20] and Aprile et al[52] predict a noise subtracted energy resolution of 1.44% and 0.87% at 2.458 MeV. We conservatively estimate a final detector energy resolution of 1.5%, corresponding to a ΔE of 146 keV (2384 keV - 2531 keV, or Q $\pm$ 2σ).

The $0\nu\beta\beta$ detection efficiency (ϵ) is given by the total simulated $0\nu\beta\beta$ detection efficiency during data taking (T in equation 7.1 will then refer to experiment live-time). As discussed in section 4.6, the single site criterion accepts 86.8% of events.

Source	$2\nu\beta\beta$ [evt/yr (%)]	$0\nu\beta\beta$ [evt/yr (%)]
Cryostat (cosmogenic)	283 (0.7)	$\sim$0
Cryostat (surface)	5-15 ($\sim$0)	<0.1 (0.1-0.4)
Teflon tiles	20-65 (0.1-0.2)	<0.3 (<1.1)
Cathode	13-27 (<0.1)	0.1 (0.3-0.4)
Calibration wire	15-555 (<1.4)	0.1-0.2 (0.4-0.5)
Super Insulation	27-49 (<0.2)	0.1-0.3 (0.4-0.9)
Calibration tubing	54-1198 (0.1-3.0)	0.2-0.3 (0.6-1.1)
Ionization wires	55-110 (0.1-0.3)	0.4-0.5 (1.3-1.6)
Field Shaping Resistors	83-121 (0.2-0.3)	0.4-0.5 (1.2-1.7)
APD Springs	71-138 (0.2-0.3)	0.5-0.6 (1.8-2.1)
Cryostat (intrinsic)	12-110 (<0.3)	<0.8 (<2.8)
HV Cable	113-270 0.3-0.7	0.4-0.8 (1.2-2.8)
Cosmic Rays	58-60 (0.2)	0.7-0.9 (2.5-2.9)
Acrylic	<174 (<0.4)	<1.0 (<3.5)
LXe Vessel (cosmogenic)	1459 (3.6)	1.4 (4.6)
Cryostat hardware	28-197 (0.1-0.5)	0.1-1.4 (0.4-4.8)
APDs	184-291 (0.5-0.7)	1.1-1.6 (3.6-5.4)
Lead	1018-2031 (2.5-5.1)	<3.8 (<12.6)
APD platter coating	504-759 (1.3-1.9)	3.6-5.8 (12.1-19.4)
Cables + interconnects	1062-1755 (2.7-4.4)	3.6-6.0 (11.9-20.1)
HFE	250-4268 (0.6-10.7)	<17.5 (<58.2)
LXe Vessel (intrinsic)	108-18219 (0.3-45.6)	0.5-32.9 (1.6-109.6)
Total	5422-32152 (13.6-80.4)	13.2-77.0 (44.0-256.7)

Table 7.1: Summary of the $2\nu\beta\beta$ and $0\nu\beta\beta$ background contributions for EXO-200. Percentage of background tolerance is shown for each source in parenthesis.

In addition, it is required that all events create signals on both the induction plane and the anode (some events can produce a very weak induction signal which is lost in electronic noise). This criterion has an acceptance efficiency of 97.4%. Finally, a cut is made requiring that all $0\nu\beta\beta$ events lie within the $0\nu\beta\beta$ window. The efficiency of this cut is 91.4% (Bremsstrahlung radiation which escapes the detector entirely is responsible for the majority of events which fail this cut). In total, 77.3% of $0\nu\beta\beta$ events are accepted.

Table 7.1 summarizes the total predicted $2\nu\beta\beta$ and $0\nu\beta\beta$ backgrounds for the EXO-200 experiment. Background due to radon emanation from TPC components

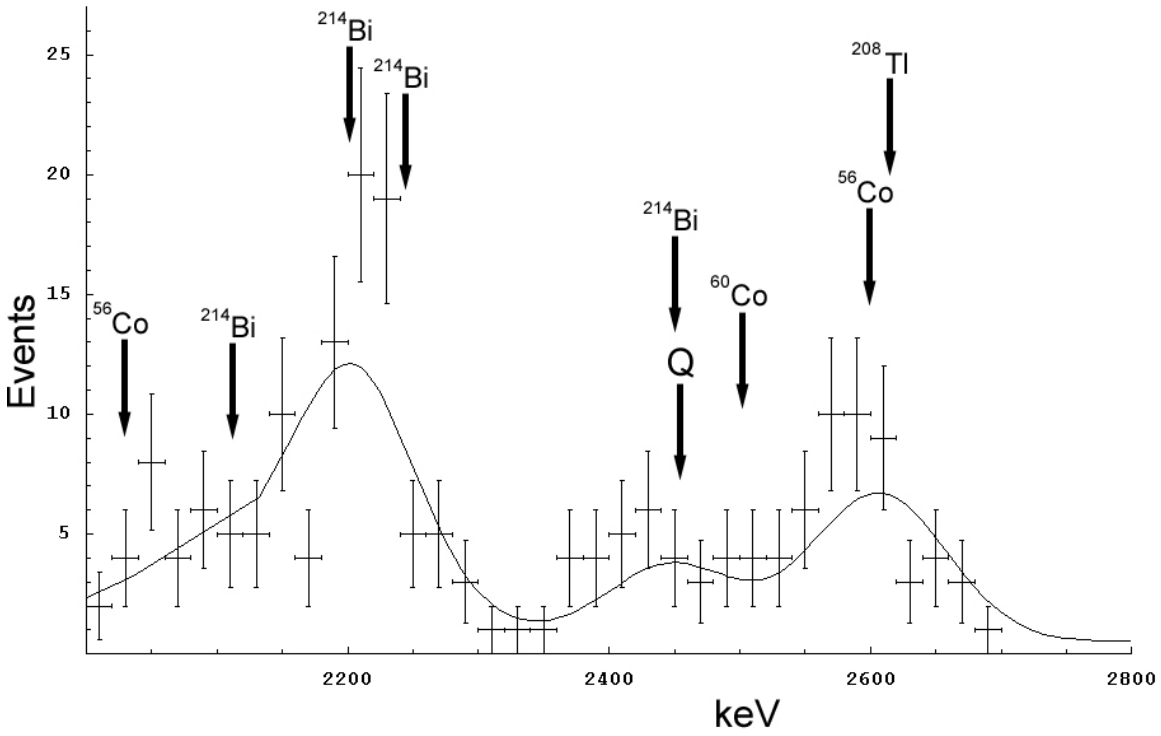

Figure 7.1: An example of an energy spectrum near the $2\nu\beta\beta$ endpoint, with $2\nu\beta\beta$ signal subtracted. 100 ^{214}Bi, 20 ^{208}Tl, and 30 ^{56}Co events were simulated, the intensities chosen simply to better illustrate the position of the decay lines. A detector resolution of 1.5% (σ/E) is used. The solid curve represents the simulated intensities of the background sources.

is not included due to the lack of accurate emanation measurements. Background due to radon emanation from the xenon system plumbing is not included under the assumption that a radon trap will eliminate this source of background. Background due to radon decay within the cryostat-lead gap is not included under the assumption that a radon tent will eliminate this source of background. Finally, background due to ^{210}Pb plating of the inner surfaces of the LXe vessel is not included due to the lack of a measurement of the ^{210}Pb concentration at this location.

When EXO-200 data is collected, the $0\nu\beta\beta$ background rate will have to be estimated and subtracted from the observed signal due to the gamma decay lines from ^{56}Co, ^{60}Co, ^{208}Tl and particularly ^{214}Bi with energies which fall within the $0\nu\beta\beta$ window (see figure 3.4). The number of counts resulting from this subtraction will be a

measure of the $0\nu\beta\beta$ rate, with a statistical uncertainty equal to the uncertainty of the original signal added to the uncertainty in the background rate itself. The $0\nu\beta\beta$ background rate will be estimated based on the strength of other prominent gamma lines from the same isotopes (the background from ^{60}Co coming from a coincidence of 1173 keV and 1332 keV gammas will be estimated based on the strengths of the individual lines). Figure 7.1 shows an illustration of an energy spectrum near the $2\nu\beta\beta$ endpoint (the solid curve represents the simulated intensities of the background sources), with the $2\nu\beta\beta$ signal subtracted and negligible $0\nu\beta\beta$ signal. It is clear that ^{214}Bi contributes most heavily to the $0\nu\beta\beta$ background, and that a prominent ^{214}Bi line at 2204 keV (5.08% intensity) can be used to estimate the contribution of ^{214}Bi to the $0\nu\beta\beta$ signal. This technique can also be applied to the other isotopes shown.

Based on the values given above, and assuming a purely statistical analysis within the $2\nu\beta\beta$ and $0\nu\beta\beta$ windows, a 90% CL sensitivity to $T_{1/2}^{0\nu\beta\beta} = (2.1 - 5.1)\times10^{25}$ is expected within two years ($T_{1/2}^{0\nu\beta\beta} = (3.3 - 8.1)\times10^{25}$ within five years). This corresponds to $\langle m_{\beta\beta}\rangle = 101 - 325$ meV after two years, ($\langle m_{\beta\beta}\rangle = 81 - 259$ meV after five years).

Appendix A

Energy Resolution Studies in an All-Teflon LXe TPC

The LXe vessel is potentially the single largest contributor to the EXO-200 backgrounds. For this reason, alternative materials were considered in its design including quartz, polycarbonate, and acrylic. DuPont Teflon TE-6472[97], a modified polytetrafluoroethylene (PTFE), proved to be the most promising alternative. Contamination levels of the raw material, as delivered by DuPont, were measured by NAA to be 0.2 ± 0.02 pg/g ^{40}K, <0.26 pg/g ^{232}Th, and < 0.35 pg/g ^{238}U, making it the most radio-quiet solid measured by the EXO-200 collaboration.

A novel welding technique was developed in collaboration with Applied Plastics Technology[96] (APT) to build vessels from this material and a prototype all TE-6472 LXe TPC was constructed and studied. The results of this effort are presented in this chapter as well as in [25].

After the work presented in this chapter, an all Teflon EXO-200 LXe vessel was designed, and prototypes were manufactured by APT. Although Teflon was ultimately rejected in favor of copper for the EXO-200 LXe vessel (primarily due to time constraints), the research and development performed indicate a high probability of success for producing an all-Teflon LXe TPC of the magnitude required by EXO-200.

A.1 The Teflon Chamber

TE-6472 is considered a modified PTFE due to the addition of a thermoplastic fluoropolymer, which turns unmodified PTFE into a weldable material. Raw TE-6472 is provided by DuPont as fine pellets. Useable material is produced first by sintering, which involves pressing the pellets in a mold with a ∼3:1 compression ratio, then baking the mold in a N_2 atmosphere. Sintered TE-6472 (referred to now simply as Teflon) has a density of 2.2 g/cm^3 at 20 °C. Once sintered, Teflon parts can be produced by conventional machining. These parts can be then be welded by heating the material to ∼450 °C under pressure for ∼2 hrs.

Weldability is extremely useful in constructing a hermetically sealed all Teflon TPC. The use of some flanges, gaskets, or fasteners (which are likely more radioactive than Teflon) is unavoidable, since a transition to a traditional metal plumbing system is necessary somewhere. Teflon weldability allows these fixtures to be located far away from the TPC. In addition, since the TPC does not need to be inserted into the vessel through the fixtures, the fixtures can be made small. This not only reduces the background impact of the fixtures, but also reduces the difficulty of sealing the detector using cryogenically compatible materials with coefficients of thermal expansion (∼1.5×10^{-5} K^{-1} for metals) much smaller than that of Teflon (2×10^{-4} K^{-1}). Finally, the ability to weld sintered parts together allows the construction of arbitrarily large components from smaller sintered elements. This would otherwise be technically unfeasible due to the size and power of the sintering press required.

The schematic for the prototype all-Teflon LXe TPC is shown in figure A.1. A drift region is created between a stainless steel cathode and an anode, with a shielding grid placed in between. The anode and shielding grid are both electroformed nickel meshes with 90% optical transparency. Three APDs are mounted to a stainless steel disk directly above the anode, and observe the drift region through the anode and shielding grids. A stainless steel backplane makes contact with the cathode of each APD, providing bias voltage. The cathode - grid distance is 2.54 cm, and the grid - anode distance is 0.86 cm. Resistance Temperature Detectors (RTDs) were placed above and below the electrode stack.

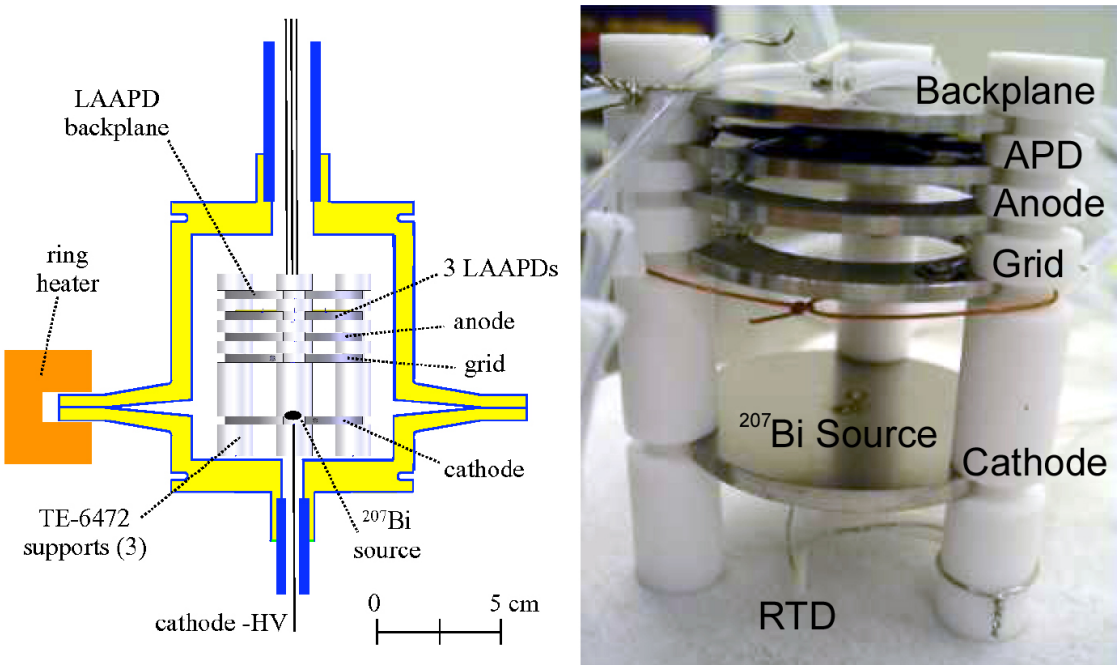

Figure A.1: Schematic of the all-Teflon LXe chamber with TPC (left). Picture of the TPC (right). Images adapted from [25].

A 1μCi ^{207}Bi source ($T_{1/2}$ = 31.6 yr) generates 570 keV and 1064 keV gammas via inverse beta decay with 97.7% and 74.5% intensity ratios. These gammas are used to measure energy resolution in the LXe. The source is a monatomic layer of ^{207}Bi electroplated onto 25 mm^2 of electroformed nickel mesh, which is spot welded to the cathode plate. The TPC is supported by three Teflon rods, and stands inside a 430 mL cylindrical Teflon chamber with 7.9 cm inner diameter and 8.8 cm inner length. Two commercially purchased tubes (2.5 cm and 1.9 cm outer diameter, with 3 mm wall thickness), made from Dyneon modified PTFE TFR-1105 by the 3M Company, are welded to sockets machined into the top and bottom of the chamber (the material of these tubes was arbitrarily chosen, with the only constraint being weldability). The top pipe serves as Xe inlet, and the bottom Xe outlet, providing a recirculation and xenon purification path. In addition, the outlet pipe serves as a conduit for the HV cathode wire, separating it from the lower voltage or grounded grid, anode, RTD, and APD wires which pass through the inlet pipe.

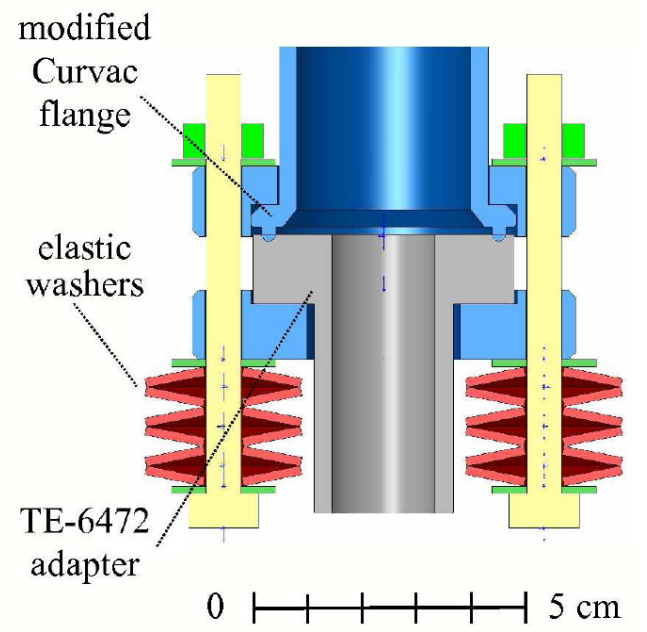

Figure A.2: Schematic of the Teflon-to-metal seal developed for use in the prototype all-Teflon LXe TPC. Image adapted from [25].

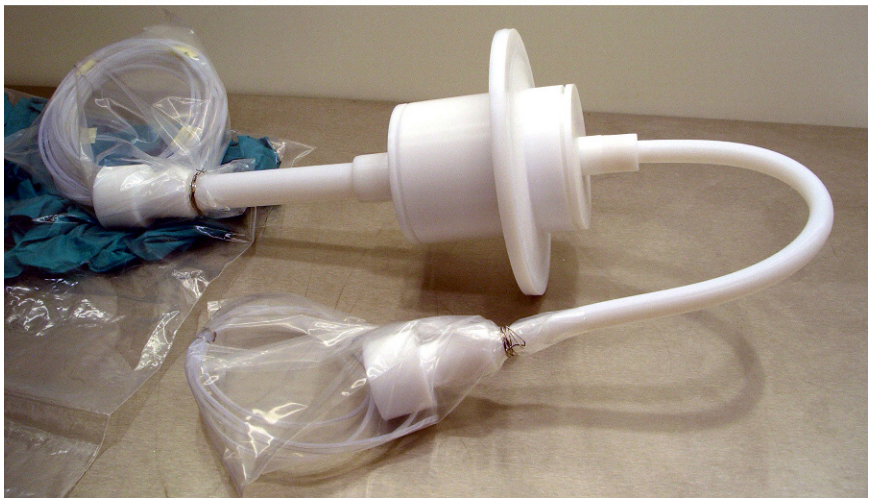

Figure A.3: The fully welded all-Teflon prototype TPC. Image adapted from [25].

Teflon adapter flanges are welded to the ends of the inlet and outlet tubes. These adapters were part of a Teflon-to-metal seal, shown schematically in figure A.2. A modified stainless steel Curvac[131] flange is pressed into the Teflon adapter flange. The sealing surface profile of the Curvac flange is a raised 1.27 mm diameter half-circle. A linear pressure of 82 kg/cm is maintained by elastic washers, which accommodate the coefficient of thermal expansion and long-term creep of Teflon. This seal was shown to work reliably through temperature cycles from 380 K to 170 K, with He leak rate $< 1{\times}10^{-4}$ cm^3 mbar s^{-1} consistent with He permeability of the teflon components.

Construction of the Teflon vessel body involved several different welds, performed in a specialized welding shop at Applied Plastic Technologies[96]. First, sintered Teflon blocks were welded together to obtain billets of sufficient size. The chamber halves were then machined from these billets. Flared ends accommodated the thermal distortions experienced during the weld, and moved the very hot weld region away from the sensitive TPC. The flared ends were mated, and a nickel plated copper ring heater was used to weld the TPC within the chamber. Ar gas was run through the chamber during the welding procedure in order to keep the temperature of the TPC from rising above 150 °C. The completed Teflon prototype TPC is shown in figure A.3.

A 90% reduction in the quantum efficiency of the APDs at 175 nm was observed after welding the TPC in the LXe vessel. In addition, the APD leakage currents increased to 1000× their original value immediately after the weld, and dropped to 30× their original value in the subsequent 2.5 months. It is suspected that outgassing of corrosive fluorides during the welding process[132] was responsible for damaging the APDs, though direct evidence of such fluorides was not obtained. A method of mitigating this damage was developed, and is shown schematically in figure A.4. An Ar purge path is created, placing the APDs upstream of the weld region. A high impedance path separates the APDs and weld region, reducing the possibility that corrosive fumes from the weld diffuse into the main chamber volume. This method proved successful in preventing any detectable damage to the APDs, though a LXe TPC was not produced utilizing this technique.

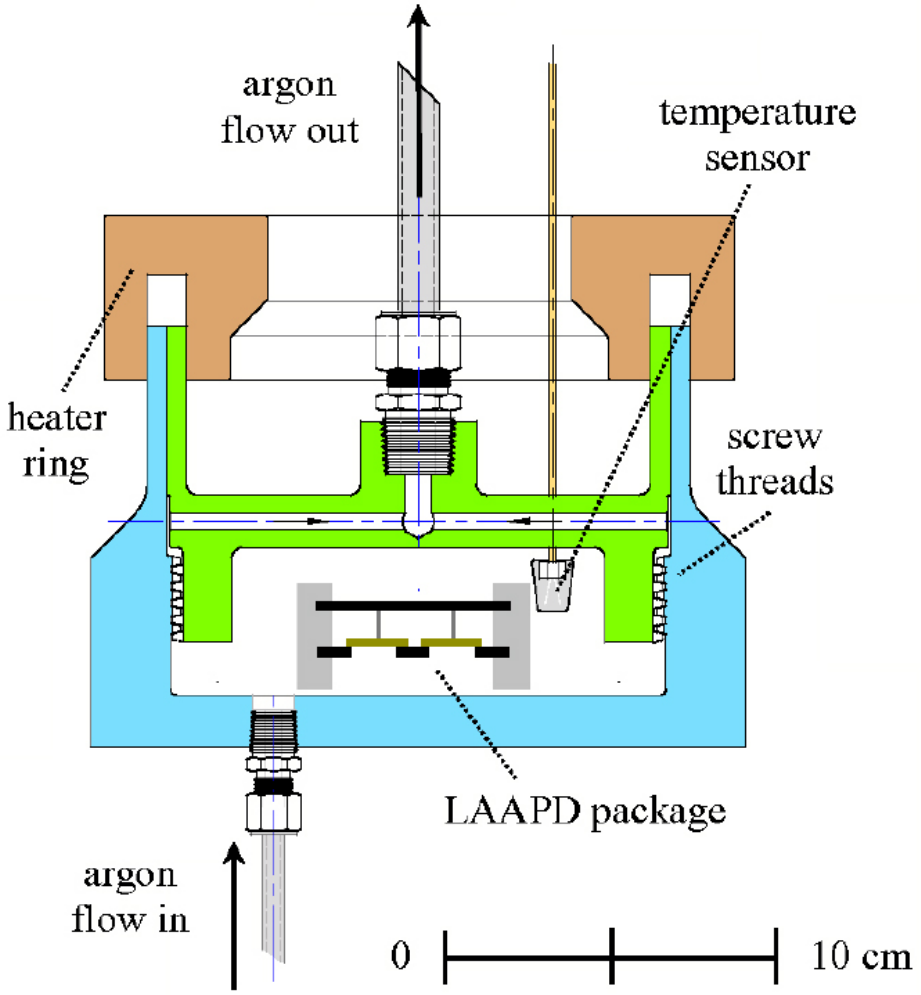

Figure A.4: Schematic of a Teflon test chamber designed to protect sensitive APDs from weld fumes via an Ar purge. Image adapted from [25].

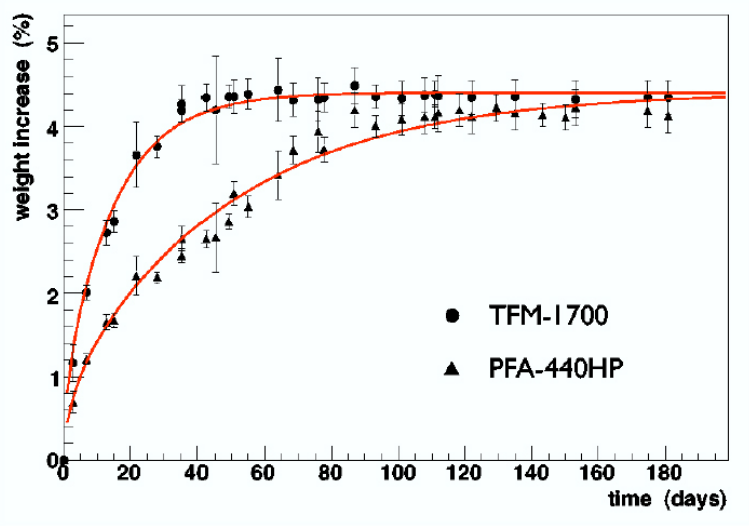

Figure A.5: The permeation of HFE into submerged samples of TFM-1700 and PFA-440HP. The data is fit assuming diffusion into an infinite, parallel plate slab (see text).

A final consideration in designing an all-Teflon TPC for EXO-200 is permeation of HFE through the Teflon walls. Two possible impacts of HFE permeation were investigated. The first was the introduction of electronegative impurities into the LXe. The second was mechanical degradation of the Teflon. The investigations took place prior the selection of DuPont TE-6472 as the prototype Teflon TPC material. Thus data on two other fluoropolymers (DuPont PFA-440HP and 3M modified PTFE TFM-1700) are presented. The permeation properties of TFM-1700 and TE-6472 are expected to be similar, since both are modified PTFEs.

Dog-bone shaped samples, 1.6 mm thick, 38 mm long, and 15 mm wide were submerged in HFE at room temperature. Their weight was recorded as a function of time, and is shown in figure A.5. The fractional weight gain vs time $\lambda(t)$ is fit assuming diffusion into an infinite, parallel plate slab:

$$\lambda(t) = S\left[1 - \frac{4}{\pi^2}\sum_{n=1}^{\infty}\frac{1-(-1)^n}{n^2}e^{-(\frac{n\pi}{L}^2)Dt}\right] \tag{A.1}$$

where S is solubility, L the thickness of the sample, and D the coefficient of diffusion.

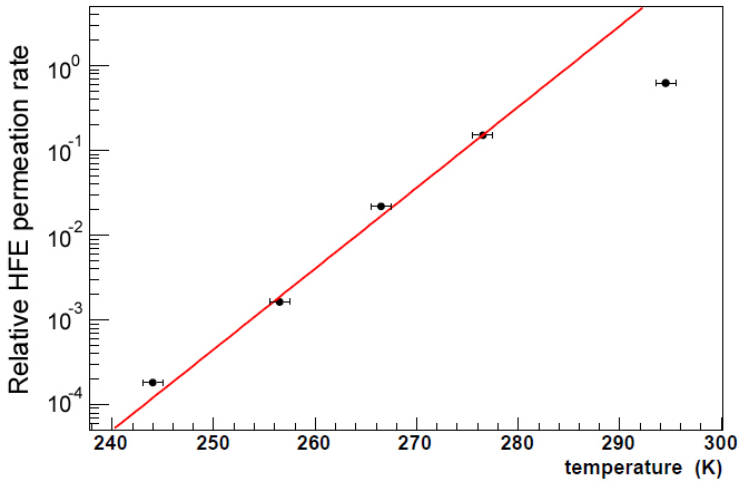

Figure A.6: Variation with temperature of the emission of HFE from a fully saturated TE-6472 sample into Xe gas. The slope of the fit is -10.5.

The fit yields S = (4.4±0.2)% and D = (1.9±0.7)×10^{-9} cm^2 s^{-1} for TFM-1700, and S = (4.4±0.5)% and D = (5.9±2.1)×10^{-10} cm^2 s^{-1} for PFA-440HP. Shorter term tests were performed on TE-6472, and indicated a ∼10% lower value of D when compared to TFM-1700.

A verification test was performed by exposing one side of a thin PFE-440HP membrane to HFE at room temperature, and the other side to vacuum. The fractional HFE content of the vacuum was measured using a residual gas analyzer (RGA). D = 3×10^{-10} cm^2 s^{-1} was obtained for PFA in this measurement, within a factor of 2 of the central value obtained by measurement of the dog-bones.

A final test was performed by inserting a sample of TE-6472 Teflon fully saturated with HFE into a Xe cell. The cell was held at various temperatures as gaseous Xe was circulated through it, and the HFE content of the Xe was sampled using an RGA in order to measure D. Figure A.6 shows the results of this experiment. The temperature dependence of HFE permeation was found to vary as $10^{-\Delta T/10.5}$ within the temperature range 245 K - 280 K. Below 245 K the HFE content of the Xe was immeasurable. Extrapolation to LXe temperatures indicates that HFE permeation through TE-6472 would be insignificant if an all-Teflon vessel were used in EXO-200.

A.2 Energy Resolution in an All-Teflon LXe Ionization Chamber

Despite the reduction in APD quantum efficiency, the prototype TPC was operated and LXe resolution due to ionization alone was measured. The APDs were sensitive enough to use as an event trigger and as a means of measuring the vertical location of the event via scintillation - ionization timing.

The LXe prototype vessel described in the previous section is connected to a Xe gas handling system. A vessel is suspended in a cryogenic dewar, equipped with a LN_2 heat exchanger. Prior to liquefaction, the xenon gas handling system and Teflon vessel were baked under vacuum at 380 K for several days. The cryostat was purged with Ar during this time to remove all air contained within the walls of the Teflon vessel. The Ar is then replaced with HFE, and the cryostat is cooled to 170 K. Commercial Xe is passed through an Oxysorb[133] purifying cartridge 8 times in order to remove O_2 and H_2O prior to data taking.

The data shown here was taken at 168 K, and 160 kPa. The ionization signal was detected by an Amptek A250 preamplifier, shaped with a Canberra model 2020 spectroscopy amplifier. A National Instruments transient digitizer recorded the signal to a control PC. The signals were fit to the following 5-parameter Gaussian distribution

$$A\sigma\left[erf\left(\frac{t_0}{\sqrt{2}\sigma}\right)-erf\left(\frac{-t+t_0}{\sqrt{2}\sigma}\right)\right]e^{\frac{-t+t_0}{\tau}}+B \tag{A.2}$$

where A is the amplitude, t_0 the drift time ($t=0$ is defined as the time of the APD signal), σ the integrator time constant, τ the differentiator time constant, and B a vertical offset. The electronic noise of data acquisition system was measured to be 597 electrons by injecting a known charge into the pre-amplifier input.

Only events interacting very near the cathode were selected, resulting in a relatively pure sample of internal conversion electron events and minimizing the effects of any inhomogeneity in drift field and purity. An ionization spectrum obtained at a drift field of 1.5 kV/cm is shown in figure A.7. The fit shown on the 570 keV peak is a Gaussian plus straight line. Noise-subtracted energy resolution is then calculated,

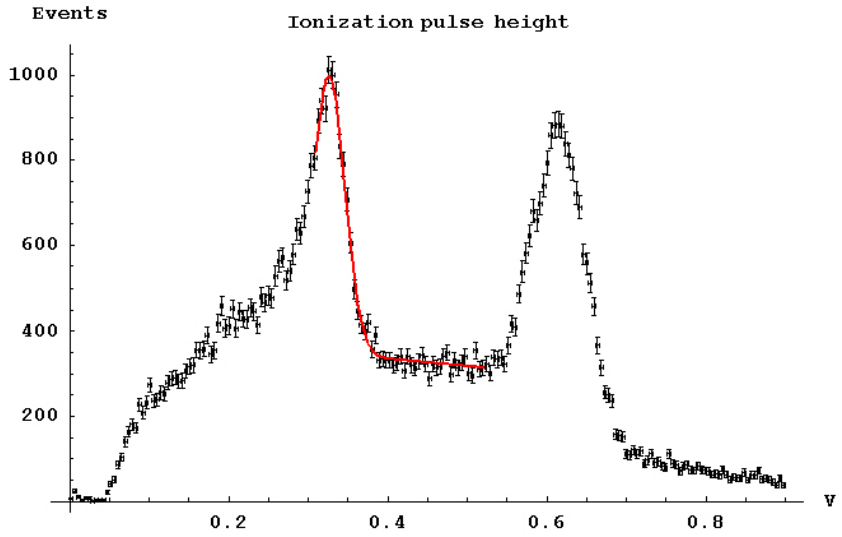

Figure A.7: The ionization spectrum measured at a drift field of 1.5 keV/cm. The 570 keV peak is fit to Gaussian plus straight line.

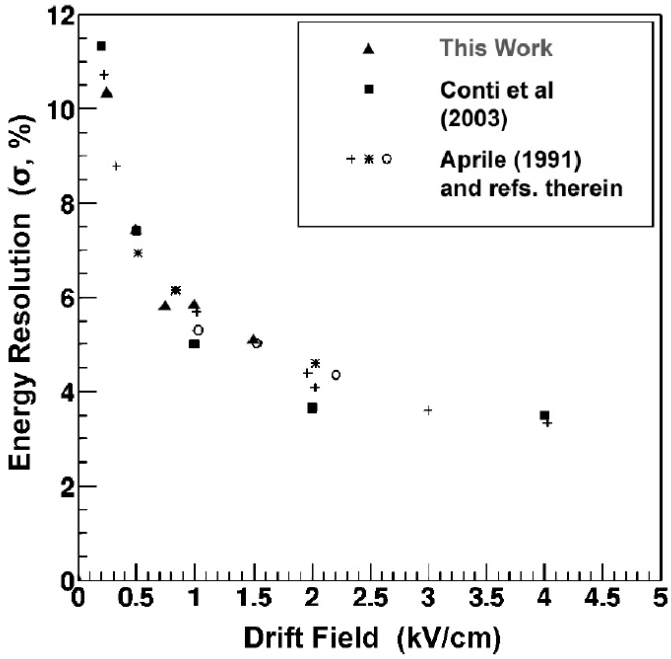

Figure A.8: LXe resolution from ionization alone obtained in an all-Teflon TPC. The results are compared to results obtained earlier by the EXO collaboration and other experiments.

and is shown for multiple field strengths in figure A.8. The ionization energy resolution obtained in the all-Teflon prototype TPC is in good quantitative agreement with the results obtained earlier by the EXO collaboration (see figure 2.3) and by others using conventional metal TPCs.

Bibliography

[1] Particle Data Group, C. Amsler *et al.*, Phys. Lett. B **667**, 526 (2003).

[2] H. Klapdor-Kleingrothaus *et al.*, Mod. Phys. Lett. A **21**, 1547 (2006).

[3] C. E. Aalseth *et al.*, Mod. Phys. Lett. A **17**, 1475 (2002).

[4] F. Boehm and V. P., *Physics of Massive Neutrinos*, 2 ed. (Cambridge University Press, 1992).

[5] F. Simkovic *et al.*, Phys. Rev. C **79**, 055501 (2009).

[6] J. Menendez *et al.*, arXiv:0801.3760v1 (2008).

[7] W. C. Haxton and G. J. Stephenson Jr., Progr. Part. Nucl. Phys. **12**, 409 (1984).

[8] E. Caurier, F. Nowacki, and A. Poves, Phys. Rev. Lett. **77**, 1954 (1996).

[9] J. Engel, P. Vogel, and M. Zirnbauer, Phys. Rev. C **37**, 731 (1988).

[10] K.-K. H. Staudt A., Muto K., Europhys. Lett. **3137**, 31 (1990).

[11] S. J. Toivanen J., Phys. Rev. Lett. **75**, 410 (1995).

[12] G. Pantis, F. Simkovic, J. Vergados, and A. Faessler, Phys. Rev. C **53**, 695 (1996).

[13] J. R. de Laeter, Pure Appl. Chem. **75**, 683 (2003).

[14] T. Takahashi, Phys. Rev. A **12**, 1771 (1975).

[15] T. Doke *et al.*, Jpn. J. Appl. Phys **41**, 1538 (2002).

[16] M. Eisenbud and T. F. Gesell, *Environmental Radioactivity from Natural, Industrial and Military Sources, 4th Edition* (Academic Press, 1997).

[17] S. Cebrian *et al.*, Astroparticle Physics **33**, 316 (2010).

[18] A. C. Hollis Hallet, *Argon, Helium and the Rare Gases I* (Interscience Publishers (New York/London), 1961).

[19] E. Aprile *et al.*, Phys. Rev. Lett. **97**, 081302 (2006).

[20] EXO Collaboration, E. Conti *et al.*, Phys. Rev. B **68** (2003).

[21] NIST ESTAR: http://physics.nist.gov/PhysRefData/Star/Text/ESTAR.html ,XCOM: http://www.nist.gov/physlab/data/xcom/index.cfm.

[22] M. Moszynski *et al.*, Nucl. Inst. Meth. A **485**, 504 (2001).

[23] C. Silva *et al.*, arXiv:0910.1058v1 (2009).

[24] Jetseal, http://www.jetseal.com/umegaseal.php.

[25] F. LePort *et al.*, Nucl. Inst. and Meth. A **578**, 409 (2007).

[26] Super-Kamiokande Collaboration, Y. Ashie *et al.*, Phys. Rev. Lett. **93**, 101801 (2004).

[27] SNO Collaboration, S. N. Ahmed *et al.*, Phys. Rev. Lett. **92**, 181301 (2004).

[28] K. Eguchi *et al.*, Phys. Rev. Lett. **90**, 021802 (2003).

[29] E. Majorana, Nuovo Cimento **14**, 171 (1937).

[30] W. Furry, Phys. Rev. **56**, 1184 (1939).

[31] R. Bernabei *et al.*, Phys. Lett. B **546**, 23 (2002).

[32] H. Klapdor-Kleingrothaus *et al.*, Eur. Phys. J. A **12** (2001).

[33] NEMO-3, R. Arnold *et al.*, Phys. Rev. Lett **95** (2005).

[34] NEMO-2, R. Arnold *et al.*, Nucl. Phys. A **658**, 299 (1999).

[35] F. Danevich *et al.*, Phys. Rev. C **68** (2003).

[36] CUORE, C. Arnaboldi *et al.*, Phys. Rev. C **80** (2008).

[37] R. N. Mohapatra, Phys. Rev. D **34**, 3457 (1986).

[38] H. V. Klapdor-Kleingrothaus and U. Sarkar, Phys. Lett. B **554**, 45 (2003).

[39] D. Soa *et al.*, Journal of Experimental and Theoretical Phys. **108**, 757 (2009).

[40] Z. Maki, M. Nakagawa, and S. Sakata, Prog. Theor. Phys. **28**, 870 (1962).

[41] M. Colaboration, Presented at the XXIV International Conference on Neutrino Physics and Astrophysics, June 2010.

[42] C. Kraus *et al.*, Nucl. Phys. A **721** (2003).

[43] V. M. Lobashev, Yadernaya Fizika **63**, 1 (2000).

[44] A. Osipowicz *et al.*, hep-ex/0109033 (2001).

[45] V. Barger, D. Marfatia, and A. Tregre, Phys. Lett. B **595**, 55 (2004).

[46] U. Seljak, A. Slosar, and P. McDonald, astro-ph/0604335 (2006).

[47] A. Goobar *et al.*, J. Cosmol. Astropart. Phys. **6**, 19 (2006).

[48] H. Klapdor-Kleingrothaus *et al.*, Mod. Phys. Lett. A **16**, 2409 (2001).

[49] H. Klapdor-Kleingrothaus *et al.*, Phys. Lett. B **586**, 198 (2004).

[50] L. W. Alvarez, Lawerence Radiation Laboratory Physics Notes , 672 (1968).

[51] CUORE, C. Arnaboldi *et al.*, Phys. Rev. Lett **95** (2005).

[52] E. Aprile *et al.*, Phys. Rev. B **76**, 014115 (2007).

[53] M. Redshaw *et al.*, Phys. Rev. Lett. **98** (2007).

[54] Y. Suzuki *et al.*, *The International Workshop on Technique and Application of Xenon Detectors* (World Scientific, 2002).

[55] A. Baldini *et al.*, IEEE Trans. Dielec. Elect. Insul. **13**, 547 (2006).

[56] E. Aprile, Nucl. Inst. Meth. A **307**, 119 (1991).

[57] E. Aprile, Nucl. Inst. Meth. A **302**, 177 (1990).

[58] L. S. Miller, S. Howe, and W. E. Spear, Phys. Rev. **166**, 871 (1967).

[59] O. Hilt and W. F. Schmidt, J. Phys.: Condens Matter **6**, L735 (1994).

[60] T. Doke, Port. Phys. **12** (1981).

[61] G. Bakale, J. Phys. Chem **80**, 2556 (1976).

[62] D. W. Swan, Proc. Phys. Soc **82**, 74 (1963).

[63] G. Bressi *et al.*, Nucl. Inst. and Meth. A **400**, 254 (2000).

[64] G. Bressi *et al.*, Nucl. Inst. and Meth. A **461**, 378 (2001).

[65] J. Jortner, L. Meyer, S. Rice, and E. Wilson, J. Chem. Phys. **42**, 4250 (1965).

[66] A. Hitachi *et al.*, Phys. Rev. B **27**, 5279 (1983).

[67] S. Kubota *et al.*, J. Physics **11**, 2645 (1978).

[68] L. Onsager, Phys. Rev. **54**, 554 (1938).

[69] A. Mozumder, Chem. Phys. Lett. **12**, 359 (1995).

[70] A. Hitachi, T. Doke, and A. Mozumder, Phys. Rev. B **46**, 11463 (1992).

[71] U. Fano, Phys. Rev. Lett. **72**, 26 (1947).

[72] T. Doke *et al.*, Nucl. Instr. Meth. **134**, 353 (1976).

[73] W. Shockley, Czech. J. Phys. **B11**, 81 (1961).

[74] G. D. Alkhazov *et al.*, Nucl. Inst. Meth. **48**, 1 (1967).

[75] 3M, http://products3.3m.com.

[76] E. I. Esch *et al.*, Nucl. Inst. and Meth. A **538**, 516 (2005).

[77] W. N. Hess *et al.*, Phys. Rev. **116**, 445 (1959).

[78] EXO Collaboration, D. Leonard *et al.*, Nucl. Instr. Meth. A **591**, 490 (2008).

[79] MIT Nuclear Reactor Laboratory,
http://web.mit.edu/nrl/www/research/neutron_activation.htm.

[80] Whatman part #: 1442-090,
http://www.whatman.com/QuantitativeFilterPapersAshlessGrades.aspx.

[81] Application Software Group, CERN,
http://wwwasd.web.cern.ch/wwwasd/geant/.

[82] FLUKA,
http://www.fluka.org/fluka.php.

[83] O. Bunemann, T. Cranshaw, and J. Harvey, Can. J. Res. A **27** (1949).

[84] Vaga Industries - Precision Thin Metal Parts through Photo Chemical Machining, http://www.vaga.com/.

[85] E. Jordan Brookes Co.,
http://www.ejbmetals.com/pdf/datasheets-metal_strip/Ca510.pdf.

[86] E. D. Earle and E. Bonvin, SNO-STR-92-061 (1992).

[87] Technic Inc product # 240552S, special order to 16g/gal,
http://www.technic.com/.

[88] API product # SD630-70-75-500,
http://www.advancedphotonix.com/ap_/pdfs/SD630-70-75-500.pdf.

[89] Hamamatsu - Solid State Devision,
http://sales.hamamatsu.com/index.php?id=13166473.

[90] Radiation Monitoring Devices Inc - Silicon Avalanche Photodiodes,
http://www.rmdinc.com/products/p006.html.

[91] R. Neilson *et al.*, Nucl. Inst. and Meth. A **608**, 68 (2009).

[92] Norsk Hydro ASA part #: 77225151, http://hydro.com/en/.

[93] EMCO High Voltage Corp, http://www.emcohighvoltage.com/regulated.html.

[94] Vacuum Process Engineering Inc, http://www.vpei.com/.

[95] Cerac Inc part #s: M-2010 (MgF_2), N-2023 (Ni), G-1065 (Au),
http://www.cerac.com/.

[96] Applied Plastic Technologies, http://www.ptfeparts.com/.

[97] E.I. du Pont de Nemours and Co., http://www.dupont.com/.

[98] C. Silva *et al.*, Nucl. Inst. Meth. A **580**, 322 (2007).

[99] Pasternack Enterprises part # RG217, http://www.pasternack.com/.

[100] Glassman part #: ER75N04-CT11, http://www.glassmanhv.com,.

[101] Ansoft, http://www.ansoft.com/products/em/maxwell/.

[102] E.I. du Pont de Nemours and Co. Part #s 1108 (resistor paste) and 6160 (conductor paste),
http://www.dupont.com/.

[103] Swiss Jewel Company, http://www.swissjewel.com/.

[104] Piconics, http://www.piconics.com/.

[105] Holders Technology part # MC18-25-00CEM,
http://www.holderstechnology.com/catalog/product.cfm?product=66.

[106] Nippon Steel Chemical Co, http://www.nscc.co.jp/english/.

[107] Dupont part # FR0110,
http://www2.dupont.com/Pyralux/en_US/assets/downloads/
pdf/FRcoverlay_H-73234.pdf.

[108] Flexible Circuit Technologies, http://www.flexiblecircuit.com/.

[109] Aurubis, http://www.aurubis.com/en/home/.

[110] Deutsches Elektronen-Synchrotron, http://www.desy.de/.

[111] Walter Valenite, http://www.walter-tools.com/us.

[112] Applied Fusion Inc, http://www.appliedfusioninc.com/.

[113] MWS Wire Industries part # MWS-650 annealed, http://www.mwswire.com/.

[114] Emhart Teknologies, http://www.emhart.com/products/helicoil.asp.

[115] McMaster-Carr, part # 93516A720,
http://www.mcmaster.com/#93516a720/=7qhkh2.

[116] Lamineries Matthey SA, http://www.matthey.ch.

[117] Master Bond, part # EP29LPSP,
http://www.masterbond.com/tds/ep29lpsp.html.

[118] Sheldahl, part # 146477, http://www.sheldahl.com/.

[119] McMaster-Carr, part #s 93516A752 and 93490A035,
http://www.mcmaster.com/.

[120] Metallica, http://www.metallica.ch/opus/.

[121] McMaster-Carr, part # 8955K42,
http://www.mcmaster.com/#tubing/=7qguul.

[122] Omega Engineering, part # TT-T-30-SL, www.omega.com/.

[123] Simolex Rubber Corporation, Compound #: SIM4768Pt, http://www.simolex.com/.

[124] SDMS, http://www.sdms.fr/.

[125] Brooks Automation, Part #: PFC-672HC, http://www.brooks.com/.

[126] BV Thermal Systems, Part #: MC300-E1-J6-H2-C6-RV-SR, http://www.bayvoltex.com/.

[127] L. Wilhelmova *et al.*, Nucl. Inst. Meth. B **17**, 568 (1986).

[128] The Doe Run Company: http://www.doerun.com/.

[129] JL Goslar GmbH and Co.: http://www.jlgoslar.de/index_e.htm.

[130] National Instruments, http://sine.ni.com/nips/cds/view/p/lang/en/nid/13505.

[131] Ultek Corp, Palo Alto, CA.

[132] W. C. Seidel *et al.*, Chem. Res. Toxicol **4**, 229 (1991).

[133] Spectron, http://www.spectron.de/.